Real-Time Control Framework for Active Distribution Networks Theoretical Definition and Experimental Validation

THÈSE N^{O} 7197 (2016)

PRÉSENTÉE LE 14 OCTOBRE 2016

À LA FACULTÉ DES SCIENCES ET TECHNIQUES DE L'INGÉNIEUR
LABORATOIRE DES SYSTÈMES ÉLECTRIQUES DISTRIBUÉS - CHAIRE EOS HOLDING
PROGRAMME DOCTORAL EN ENERGIE

ÉCOLE POLYTECHNIQUE FÉDÉRALE DE LAUSANNE

POUR L'OBTENTION DU GRADE DE DOCTEUR ÈS SCIENCES

PAR

Lorenzo Enrique REYES CHAMORRO

acceptée sur proposition du jury:

Dr S.-R. Cherkaoui, président du jury
Prof. M. Paolone, directeur de thèse
Prof. K. Strunz, rapporteur
Prof. L. Wehenkel, rapporteur
Prof. J.-Y. Le Boudec, rapporteur

ÉCOLE POLYTECHNIQUE
FÉDÉRALE DE LAUSANNE
Suisse
2016

Queda prohibido no sonreír a
los problemas, no luchar por
lo que quieres, abandonarlo
todo por miedo, no convertir
en realidad tus sueños.
— Pablo Neruda.

It is forbidden not to smile
at problems, not to fight for
what you want, leave everything
for fear, not to make
true your dreams.
— Pablo Neruda.

To Dayana...

Acknowledgements

I would like first to thank my supervisor Prof. Mario Paolone, who firstly gave me the opportunity to join his laboratory and secondly to join a challenging research project that I have fully enjoyed during this 3 years and a half. All we, his students, are very lucky for having him as mentor, not only for his enormous wisdom but also for his holistic view of the problems we face in our day to day activities.

Thanks also to Prof. Jean-Yves Le Boudec who has played the role of a second guide during all this process and to whom I specially thank his straight and positive critics, his permanent joy and openness. I admire his tremendous ability to mold his knowledge to new challenges. Certainly an example to follow. I would like to give special thanks to Dr. Andrey Bernstein, with whom I have done almost all this trip, and from whom I have learnt a lot about mathematical modeling and optimization.

This path would not had been possible without the initial support of Dr. Rodrigo Palma-Behnke and Dr. Guillermo Jiménez-Estévez, my former bosses and actual friends, who encouraged me take this opportunity. This is an acknowledgment from me and my family.

I cannot leave out of this page all my colleagues and friends in the DESL. I thank you all for the moments of discussion, amusement, drinks, barbecues, coffee breaks and a big etc. Yet, I have to specially thank Sylvain Robert and Sophie Flynn, always available for helping in my French and to solve whatever request of mine. To my office-mates, Nicolás, Dongshuai, Enrica and Andreas, I have gained a lot of intercultural experiences with you. Our office has been certainly rich of friendship.

To my new friends in Lausanne, those that I call my Swiss family. A toast and a *see you soon* are more than enough for thanking all the love, company and laughs that I, and my family have shared with you. You all know that even after leaving Switzerland we will always welcome you in our home.

I want to give special thanks to Dr. José Mardones and the authorities of the Institute of Electricity and Electronics of the Austral University of Chile for believing in me and making for me a place in their group. I am looking forward for joining you.

And of course, I cannot finish without expressing my greatest gratitude to my beloved wife Dayana and my son Agustín. They have been the everyday reason to continue pushing forward against every difficulty. You are the source of my strength and the light in my path. Dayana, I am infinitely thankful of all your support, understanding, encouragement and loyal partnership. I know that this has been in several moments more difficult for you than for me, and I will always thank you for that. Agustín, you came just in the middle

of the path, but bringing a whole bouquet of feelings to me and your mom, including some that we did not even know that we could feel. You have just made me better person and greater in all sense. You repeat this every day at this age, and I think it reflects perfectly what I feel towards you: I love you *to infinity and beyond*.

Lausanne, 8 September 2016 L. R.

Abstract

The great challenge of massively integrating the volatile distributed power-generation into the power system is strongly related to the evolution of their operation and control. The literature of the last decade has suggested two models for such an evolution: (i) the *supergrid* model, based on enhanced continental/intercontinental network interconnections (mainly DC) for bulk transmission, (ii) the *microgrid* mode, where small medium/low voltage networks interfacing heterogeneous resources, such as local generation, energy storage and active customers, are intelligently managed so that they are operated as independent cells capable of providing different services from each other and operate in islanded mode.

Irrespective of the model that will eventually emerge, the control of heterogeneous distributed resources represents a fundamental challenge for both supergrid and microgrid models. This requires the definition of scalable and composable control methods that guarantee the optimal and feasible operation of distribution grids in order to satisfy local objectives (e.g., distribution grid power balance), as well as the provision of ancillary services to the external bulk transmission (e.g., primary and secondary frequency supports). Several control methodologies have been proposed to achieve these goals, and the majority of them have been inspired by the classic time-layered approach traditionally adopted in power systems that are associated with different time-scales and extension of the controlling area, i.e. primary, secondary and tertiary controls, ranging from sub-seconds to hours, respectively. In the context of microgrids, these three levels of control can be associated with a decision process that can be centralized (i.e., a dedicated central controller decides on the operation of the system resources) and/or decentralized (each element decides based on its own rules). In the current literature, the former is used for long-term, whereas the latter for short-term decisions. In particular, primary controls are typically deployed through fully decentralized schemes mainly relying on the use of droop control.

With this in mind, in this thesis we propose, and experimentally validate, a novel control framework called COMMELEC – *A Composable Framework for Real-Time Control of Active Distribution Networks, Using Explicit Power Set-Points.* It controls a power grid in real-time based on a multi-agent structure, using a simple and low-bandwidth communication protocol. Such a framework enables a controller to easily steer an entire network as an equivalent energy resource, thus making an entire system able to provide grid support by exploiting the flexibility of its components in real-time.

Acknowledgements

The main features of the framework are (i) that it is able to indirectly control the reserve of the storage systems, thus maximizing the autonomy of the islanding operation, (ii) that it keeps the system in feasible operation conditions and better explores, compared to traditional techniques, the various degrees of freedom that characterize the system, and (iii) that it maintains the system power-equilibrium without using the frequency as a global variable, even being able to do so in inertia-less systems.
Our framework has been extensively validated, first by simulations but, more importantly, in a real-scale microgrid laboratory specially designed and setup for this goal. This is the first real-scale experiment that proves the applicability of a droop-less explicit power-flow control mechanism in microgrids.

Key words: Real-time control, explicit distributed optimization, decentralized control, congestions management, power sharing, renewable energy, active distribution networks, microgrids, distributed energy resources, energy storage systems, demand response, multi-agent system, scalability, composability, isolated microgrid, grid-connected microgrid, microgrid operation mode transitions, voltage and power control.

Résumé

Le grand défi d'intégrer massivement la génération distribuée volatile dans les systèmes électriques de puissance est strictement lié à l'évolution des principes d'opération et contrôle. La littérature des dernières décennies a suggéré deux modèles pour une telle évolution : (i) le modèle super-réseau, basé sur le renforcement des interconnections continentales / intercontinentales (principalement en DC) pour le réseau de transport ; ou (ii) le modèle micro-réseau, où petits réseaux de basse et moyenne tension, qui interfacent des ressources hétérogènes telles que la production d'électricité locale, le stockage d'énergie et les consommateurs actifs, sont intelligemment gérés pour opérer comme des cellules indépendantes capables de fournir des services entre eux et d'opérer en îlot.

Quel que soit l'approche qui sera éventuellement adoptée, le contrôle de ressources hétérogènes distribuées représente un défi fondamental pour les deux modèles. Cela requiert la définition de méthodes de contrôle extensibles et composables qui puissent garantir l'opération optimale et faisable des réseaux de distribution, de manière à satisfaire des objectifs locaux (ex. équilibrage de puissance) ainsi que l'approvisionnement des services auxiliaires au réseau de transport (ex. contrôle primaire et secondaire de fréquence).

Plusieurs méthodes de contrôle ont été proposées pour atteindre ces buts et la majorité a été inspirée par l'approche "time-layered" classique qui est traditionnellement adoptée dans les réseaux électriques, c.à.d. le contrôle primaire, secondaire et tertiaire. Ces contrôles sont associés à diverses échelles de temps et à la taille de la zone contrôlée. Dans le contexte des micro-réseaux, ces trois niveaux peuvent être associés à une décision qui peut être centralisée (i.e. un contrôleur central dédié prend les décisions d'opération des ressources du système) et/ou décentralisée (i.e. chaque élément prend ses décisions sur la base de ses propres règles). Dans la littérature actuelle, la première approche est utilisée pour le long terme, tandis que la deuxième est utilisée pour les décisions à court terme. En particulier, le contrôle primaire est typiquement déployé à travers un régime complètement décentralisé, principalement en s'appuyant sur le "droop control".

Suite à ce qui précède, le but de cette thèse est de proposer et valider expérimentalement une méthode de contrôle original, appelé COMMELEC – *A Composable Framework for Real-Time Control of Active Distribution Networks, Using Explicit Power Set-Points.* Cette méthode vise à contrôler un réseau de puissance en temps réel sur la base d'une structure multi-agent, utilisant un protocole de communication simple et avec un débit de données limité. Un cadre comme celui-ci permet de diriger facilement un réseau entier comme une ressource équivalente unique en lui permettant de soutenir le réseau principal

à travers l'exploitation de la flexibilité de ses composants en temps réel.
Les principales fonctionnalités de la méthode sont : (i) contrôler indirectement la réserve des systèmes de stockage et, par conséquent, de maximiser l'autonomie de l'opération en îlot, (ii) garder le système sous des conditions de fonctionnement faisables en exploitant ses degrés de liberté d'une meilleure manière et (iii) garder le bilan de puissance du système sans utiliser la fréquence comme une variable globale, ce qui lui permet de piloter des systèmes sans inertie.
La méthode a été largement validé, d'abord par des simulations et plus important encore, dans un setup micro-réseau à l'échelle réelle. Cette installation est la première infrastructure expérimentale qui prouve l'application d'un mécanisme de contrôle des flux de puissance explicits sans "droop control".

Mots clefs : Côntrole en temps réel, optimisation distribuée explicite, côntrole decentralisé, gestion des congestion des lignes, répartition de puissance, energie renouvelable, réseaux de distribution actifs, micro-réseaux, ressources energetiques distribuées, systèmes de stockage d'energie, côntrole de la demande, système multi agent, scabilité, composabilité, micro-réseau îloté, micro-réseau connecté au réseau, transitions de modes de fontionnement des micro-réseaux, côntrole de tension et puissance.

Abstract

La possibilità di aumentare la connessione di generazione distribuita nelle reti elettriche attuali e future è strettamente legata all'evoluzione delle metodologie di controllo di tali reti. La letteratura dell'ultimo decennio ha proposto due macro-approcci: (i) la cosiddetta supergrid, basata sul potenziamento del sistema elettrico di trasmissione a livello continentale/intercontinentale (principalmente in corrente continua); o (ii) l'approccio microgrid in cui reti di piccola estensione (normalmente a bassa e media tensione) che includono generazione, accumulo e consumo locale, sono opportunamente gestite in modo da operare come entità indipendenti capaci di fornire servizi di supporto alla rete esterna o, nel caso, di funzionare in isola.

Indipendentemente dall'approccio/modello che verrà adottato per definire l'architettura delle reti elettriche future, il controllo delle risorse distribuite rappresenta un aspetto di fondamentale importanza sia per le supergrid sia per le microgrid. In entrambi i contesti, è necessario definire delle strategie di controllo scalabili e componibili con due scopi fondamentali: garantire il funzionamento ottimo delle reti di distribuzione (e.g., controllo locale di tensione e gestione delle congestioni) e fornire servizi ancillari alla rete di trasmissione (e.g., supporto alla regolazione di frequenza primaria e secondaria). A tale riguardo, diverse metodologie di controllo sono state proposte per rispondere alle problematiche precedentemente menzionate. La maggior parte di esse sono ispirate alla classica struttura gerarchica adottata nella regolazione reti elettriche di trasmissione che include il controllo primario, secondario e terziario. I tre livelli sono generalmente associati a diverse scale temporali (da frazioni di secondo fino ad ore) e coinvolgono aree di interesse di diversa estensione.

Nel contesto delle microgrid, questi tre livelli di controllo possono essere inglobati in un unico processo decisionale che può essere centralizzato (un controllore centrale che decide per il funzionamento delle diverse risorse) e/o decentralizzato (ogni elemento decide sulla base di informazioni locali). Nella letteratura recente il primo processo viene solitamente associato a decisioni a lungo termine, il secondo, invece, per controlli con un orizzonte temporale molto più breve. In particolare, il controllo primario è generalmente effettuato in modo decentralizzato, basandosi principalmente sulla regolazione statica (statismo). Detto ciò, l'obiettivo principale di questa tesi è di proporre e validare sperimentalmente una nuova strategia di controllo denominata COMMELEC — *Composable Framework for Real-Time Control of Active Distribution Networks, Using Explicit Power Set-Points.* Tale strategia permette di controllare la rete elettrica in tempo reale ed è basata su una

struttura multi-agente. Essa si basa su un protocollo di comunicazione estremamente semplice. Tale strategia permette di aggregare le risorse di un'intera rete come una risorsa equivalente, rendendo il sistema capace di fornire supporto alla rete principale tramite la quantificazione delle flessibilità dei propri elementi.
Le principali caratteristiche della strategia proposta sono le seguenti: (i) è in grado di controllare indirettamente la riserva dei sistemi di accumulo energetico, massimizzando così l'autonomia del funzionamento in isola, (ii) mantiene la rete locale entro i limiti corretti di funzionamento, analizzando, allo stesso tempo, i gradi di libertà che caratterizzano il sistema, e (iii) mantiene l'equilibrio di potenza del sistema senza utilizzare la frequenza come variabile di controllo globale rendendo quindi possibile il controllo anche di sistemi privi di inerzia. La strategia è stata validata, in primo luogo, tramite simulazioni e, in seguito, in una microgrid sperimentale in scala reale appositamente progettata e messa a punto per tale obiettivo. Di fatto, nella tesi viene proposto il primo esempio noto, validato sperimentalmente in scala reale, che dimostri l'applicabilità di un meccanismo di controllo di microgrid non basato sul tradizionale controllo con statismo.

Parole chiave: controllo in tempo reale, ottimizzazione distribuita, controllo decentralizzato, gestione delle congestioni, ripartizione della potenza, fonti rinnovabili, reti di distribuzione attive, microgrid, risorse energetiche distribuite, sistemi di accumulo, gestione della domanda, sistema multi-agente, scalabilità, componibilità, microgrid in isola, microgrid connesse , transizioni modalità di funzionamento microgrid, controllo di tensione, controllo di potenza.

Zusammenfassung

Die Hauptherausforderung dabei, Erzeugung aus verteilten volatilen Energiequellen im grossen Massstab ins Stromversorgungssystem einzubinden, bildet der Entwicklungsbedarf im Bereich der Netzleittechnik. Im Laufe des vergangenen Jahrzehnts haben sich in der Fachliteratur zwei grundlegende verschiedene Lösungsansätze herausgebildet. (i) Der Supergrid-Ansatz setzt auf die Verstärkung des Verbundnetzes. Dies soll durch den Ausbau der Übertragungsleitungen innerhalb wie auch zwischen den Kontinenten erreicht werden (hauptsächlich durch Hochspannungsgleichstromübertragung). (ii) Der Microgrid-Ansatz setzt auf intelligente Bewirtschaftung von Verteilnetzen. Die Verbindung verschiedenartiger Ressourcen wie verteilter Erzeuger, Energiespeicher und flexibler Konsumenten soll es ermöglichen, dass die Netze sich gegenseitig Dienstleistungen erbringen oder als Inseln betrieben werden können.

Unabhängig davon, welcher Ansatz schlussendlich zur Umsetzung gelangt, stellt in jedem Fall die Regelung eines Sammelsuriums verschiedenartiger Ressourcen eine bedeutende Herausforderung dar. Daher besteht ein Bedarf nach skalierbaren, modularen Regelungsverfahren, die einen optimalen Betrieb der Verteilnetze ermöglichen. Dabei müssen Nebenbedingungen, wie die Sicherheit des Netzbetriebs, lokale Vorgaben (z.B. das Leistungsgleichgewicht), sowie die Erbringung von Systemdienstleigungen (z.B. primäre und sekundäre Frequenzstabilisierung), berücksichtigt werden.

Um diesen Anforderungen gerecht zu werden, sind verschiedene Lösungen vorgeschlagen worden. Eine Mehrzahl davon basiert auf dem klassischen hierarchischen Ansatz mit Primär-, Sekundär- und Tertiärregelung, der üblicherweise in Übertragungsnetzen angewandt wird. Die Regelungsstufen unterscheiden sich dabei sowohl in der Ausdehnung der Regelungszohne wie auch im Zeithorizont, der von Sekundenbruchteilen bis zu Stunden reicht. In einem Microgrid können diese drei Regelungsstufen entweder zentral oder dezentral implementiert werden. In ersterem Fall steuert ein einziger Regler sämtliche Ressourcen im System, in letzterem Fall entscheidet jede Ressource selbstständig nach ihren eigenen Vorgaben. In der gegenwärtigen Literatur wird der erstgenannte Ansatz für die langfristige Planung und der letztgenannte für kurzfristige Entscheidungen verwendet. Insbesondere Primärregelung wird typischerweise verteilt implementiert, zum Beispiel durch Droop Control.

In dieser Arbeit wird ein neuartiges Regelungsverfahren, genannt COMMELEC — *A Composable Framework for Real-Time Control of Active Distribution Networks, Using Explicit Power Set-Points*, vorgestellt und experimentell validiert. Dieses ist darauf ausgerichtet,

ein Stromnetz in Echtzeit zu regeln, und basiert auf einem Multiagentensystem, das sich eines simplen Kommunikationsprotokolls mit geringer Bandbreite bedient. Insbesondere kann ein Netz als Ganzes für die Netzstützung verwendet werden, indem man sich die Flexibilität seiner Bestandteile in Echtzeit zunutze macht.
Das Framework zeichnet sich durch folgende Besonderheiten aus (i) Die Reserven von Speichersystemen können implizit dafür genutzt werden, im Inselbetrieb ein Maximum an Eigenständigkeit sicherzustellen. (ii) Die Sicherheit des Netzbetriebs wird gewährleistet, wobei gleichzeitig die Freiheitsgrade des Systems besser genutzt werden. (iii) Das Leistungsgleichgewicht wird aufrechterhalten, ohne dass dafür die Frequenz als Indikator für das Ungleichgewicht berücksichtigt werden müsste. Daher lässt sich dieses Konzept auch auf Systeme ohne rotierende Massen anwenden.
Das Konzept ist einer umfassenden Validierung unterzogen worden, zum einen in Simulationen, zum anderen in einem Microgrid Labor, das eigens für diesen Zweck konzipiert und gebaut worden ist. Dies ist das erste Experiment, das die Einsetzbarkeit eines Verfahrens, welches die Leistungsflüsse statt implizit durch Droop Control explizit regelt, in einem Microgid realen Massstabes nachweist.

Schlagwörter / Schlüsselwörter: Echtzeitregelung, verteilte Optimierung, verteilte Regelung, Engpassmanagement, Leistungsumverteilung, erneuerbare Energie, aktive Verteilnetze, Microgrids, verteilte Energieressourcen, Energiespeichersysteme, Lastverschiebung, Mehragentensystem, Skalierbarkeit, Modularität, Inselnetz, Netzgekoppeltes Microgrid, Betriebsmoduswechsel in einem Microgrid, Spannungs- und Leistungsregelung.

Contents

List of Figures

List of Tables

1 Introduction

1.1 Motivation

Modern and future electrical infrastructures have to satisfy two main conflicting requirements: (i) provide reliable and secure supply to an increasing number of customers, and (ii) take into account the rational use of energy and the protection of the environment. This second requirement drives major changes in power systems, where the most evident result is an almost quadratic increase of the connection of renewable energy sources [1]. It is generally admitted that these sources need to be massive and distributed, in order to provide a significant part of the consumed electrical energy (e.g. [2]). However, the increased penetration of distributed renewable-energy resources in electrical medium and low-voltage networks is such that, in several countries, operational constraints have already been attained. Additionally, power network operators are facing a rapid and sustained reduction in the inertia of the system. This calls for a radical re-engineering of the entire electrical infrastructure. Indeed, inertia has been the key element for power system performance as it enables for smooth frequency control. Therefore, various efforts for replicating this behavior with power electronic converters have been made, for instance, by emulating inertia or applying droop control. However, these approaches are not scalable and suffer from stability issues when several power converters interact at the same time.

As it is known, the main controls of an interconnected power system are essentially concerned with

(i) maintaining the power balance, and

(ii) maintaining the voltage levels close to the rated values.

Both are performed at various time scales and geographical extensions. These two basic controls are the building blocks used by other more sophisticated regulators responsible for hierarchically superior actions (e.g., angular and voltage stability assessment, congestions

in main transmission corridors, etc.). As it is well known, the control of (i) is based on the link between the power imbalance and the network frequency (that constitutes the control variable), and it is usually deployed in three main time-frame controls that belong to primary, secondary and tertiary frequency controls. There are essentially two main drawbacks to this control philosophy: First, there is a monotonous increasing dependency between the primary/secondary frequency-control reserves and the errors associated with the forecasts of increasing renewable production (especially when distributed in small dispersed units). Second, the definition of the primary/secondary frequency-control reserves are centralized; hence, distributed control mechanisms, to be deployed in distribution networks with active resources, cannot be easily implemented. These mechanisms will require an increasing reserve scheduling, in order to keep acceptable margins and to maintain the grid vulnerability at acceptable levels (e.g. [3]). An example of such a principle is described in [4].

As for (ii), which requires maintaining the voltage deviations within predetermined limits (e.g., [5]), it is implemented at various levels and/or subsystems and with different strategies that mainly control reactive-power injections. Network voltages fluctuate, however, as a function of various quantities such as the local and overall network load, generation schedule, power system topology changes and contingencies. The typical approach for voltage-control divides (still into primary, secondary and tertiary) the control actions as a function of their dynamics and their area of influence. The major advantage of such an approach is that it enables a decoupling of the controllers as a function of their area of influence. However, it is not easily down-scalable to distribution networks because, similarly to the frequency control, it was conceived for interconnected power systems, where the control resources are limited in number, large in size, and centrally controlled.

In general, if we base the expression of the equilibrium of the grid purely in terms of power injections, there would always be the need to assess adequate reserves in order to guarantee the power balance (both active and reactive) of the system. In agreement with this approach, the European Network Transmission Systems Operator (ENTSO-E) attempts to extend the network codes to distribution networks. These codes set up a common framework for network connection agreements, between network operators and demand/producers owners [5]. This specific network code requires the distribution networks to provide the same frequency/voltage support provided by other centralized resources (i.e., power plants) that are directly connected to transmission networks. Such an approach, however, has many drawbacks in systems characterized by dominant non-dispatchable stochastic renewable energy resources where, to balance the power, the non-desirable use of traditional power plants (usually gas-fired power plants e.g. [6] or, when available, hydro power plants) is necessary.

1.2 Document Outline

This thesis is organized as follows.

In **Chapter 2**, we present a comprehensive survey of the literature on Microgrids Control. The survey includes conventional and industrialized approaches along with more elaborated techniques recently proposed by the scientific community. The various control strategies are first clustered according to their control time-frame and extension of the controlled area and, secondly, to the nature of the interaction among resources, i.e. fully centralized and decentralized or distributed approaches.

We devote **Chapter 3** to the formal presentation of a novel real-time control framework called COMMELEC, *A Composable Framework for Real-Time Control of Active Distribution Networks, Using Explicit Power Set-points*. Our framework is designed to be robust, scalable and able to exploit the flexibility of each energy resource in the grid, and account for their willingness and uncertainty at deploying a given set-point. The framework is presented for the specific case of microgrids. Therefore, we discuss its use for a microgrid in grid-connected mode, a microgrid in islanded mode, and how to handle the transitions between both modes. We emphasize the theoretical description and propose methods for coping with the real-time need of such a control strategy.

In **Chapter 4**, we present examples of and give ideas about the general procedure for designing COMMELEC resource agents for the typical devices connected to microgrids. Depending on their nature and/or internal characteristics, these resources have various degrees of controllability, from *fully controllable* resources (e.g., batteries) to *non-controllable* resources (e.g., uncontrollable loads). We show in this chapter that the controllability of the resource has a considerable effect on the design of the corresponding resource agent.

In **Chapter 5**, we evaluate the performance of the COMMELEC control framework. This assessment is done by using a suitably developed simulation environment. We consider a case study that makes reference to the low-voltage microgrid benchmark defined by the CIGRÉ Task Force C6.04.02. The microgrid is connected to a generic medium-voltage feeder that contains the minimum number of elements that enable us to show the applicability and potentials of the proposed control framework. In this system, we test the base features of the framework together with the performance at steering the islanding maneuver.

In **Chapter 6**, we present the design of the experimental facility that has been conceived for testing and validating the COMMELEC control framework. In a first part, special focus is put into the description of the technical specifications of the various physical devices and in the characteristics of the experimental setup. Secondly, the description of the experiments for the implementation of the framework along with their results are discussed. Emphasis is given to the computational burden needed in all the steps of the

process. In particular, results of the operation of the microgrid in grid-connected mode are shown together with a time-latency assessment.

Finally in **Chapter 7**, we conclude the thesis with a summary of the main findings.

1.3 Contributions

Our main contributions in this thesis are listed below.

(i) A simple and generic control framework, that uses *explicit power set-points*, for the real-time control of active distribution networks is proposed. Contrarily to conventional control techniques, the proposed framework makes use of a multi-agent system, where agents communicate in a semi-centralized and distributed way. The framework is built so that any combination of implemented power flows will never cause the violation of voltage or current bounds.

(ii) A flexible simulation environment where different real-time control techniques can be tested.

(iii) We discuss the modeling of typical resources connected to active distribution networks.

(iv) By using (iii), we propose the design of several resource agents that are able to work under the rules of the proposed framework.

(v) As the design of resource agents has a significant impact on the overall behavior of the grid when controlled with the proposed framework, we give recommendations on good design practices.

(vi) In order to challenge the capabilities of the proposed real-time control framework, we designed and set up a full real-scale microgrid laboratory. The microgrid is equipped with several resources, in particual, with different storage technologies.

(vii) We carried out an experimental validation of the proposed framework: it considers the overall behavior of the microgrid and the time-delays involved in the different processes.

2 State of the Art in Microgrids Control

Chapter Highlights:

We present a comprehensive survey of the literature on Microgrids Control. The survey includes conventional and industrialized approaches along with more elaborated techniques recently proposed by the scientific community.
The various control strategies are first clustered according to their control time-frame and extension of the controlled area and, secondly, to the nature of the interaction among resources, i.e. fully centralized and decentralized or distributed approaches.

The structure of this Chapter is the following. First, we give an overview of the basic power systems control needs and energy management strategies, which are generally divided by time frames and extension of the controlled area. In that sense, we synthetically recap the traditional way bulk power systems tackle these control tasks. We then present a survey of the existing literature on how these control functions have been adapted to microgrids by the existing literature.

Next, we present a literature survey by clustering the microgrids control strategies in two main groups: *fully centralized* and *distributed and decentralized* approaches. We discuss how they are related to the time-framed controls previously introduced.

2.1 Basic Functions of Power Systems Control

2.1.1 Traditional Power Systems

In interconnected bulk power systems, four main functions for keeping the system equilibrium are generally used. They are divided by time frames and extension of the controlled area: *primary*, *secondary*, *tertiary* control and *generation dispatch* [7]. The division among them is essentially related with the need of coordination of the various controllers and operators along the power system [8] (see Figure 2.1).

Primary Control

At the bottom of the hierarchy, the primary control is typically performed in a decentralized way. It is exclusively executed at the device level (generation units) using local measurements that reflect the system power imbalance (for frequency control) or the local reactive power need (for voltage control). This control acts with a response in the intra-second to seconds scale.

Secondary Control

Takes place at a subsystem[1] level and has a response in the seconds to minutes scale. It uses shared information among devices within the subsystem in order to keep the node voltages within bounds, and to reduce the permanent frequency deviation produced by the action of the primary control, given the unawareness for a device of the action of the others.

[1] A subsystem is here intended as representative of a region of a given power system within which a control objective needs to be achieved (for instance, secondary voltage control).

Tertiary Control

It is used when secondary control was not able to remove the permanent deviation due to the activation of operational constraints. It runs in the scale of some minutes to one hour and it uses detailed information of all controllable devices.

Generation Dispatch

It is at the top of the hierarchy and takes place at a larger time-scale. This process decides on the long-term operation of power systems and is the main tool used (for instance) in energy markets equilibrium. Dispatch methods have substantially evolved in the recent decades leading to unbundling power systems and liberalization of the associated energy markets. The typical time-horizon of this function is 24 hours (or more).

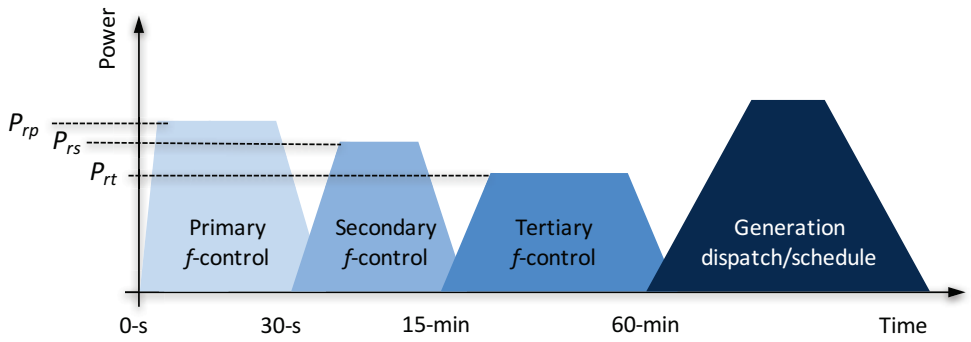

Figure 2.1 – Traditional power system control functions. P_{rp} is the primary frequency control reserve, P_{rs} is the secondary frequency control reserve and P_{rt} is the tertiary frequency control reserve. In general $P_{rp} \geq P_{rs} \geq P_{rt}$. A similar diagram can be considered for reactive power.

2.1.2 Microgrids Adaptation

In the context of microgrids, the basic control functions used in bulk power systems are typically adapted. In particular, the adaption is usually different depending upon the microgrid operation mode: grid-tie mode and islanded mode.

Thanks to the fact that all controllable devices can be found geographically close to each other and are limited in number, these control levels can be combined and hence reduce their total number with a consequent simplification of the control architecture. For example, it is a common practice to find management strategies that solve together both secondary and tertiary controls [9].

Primary Control

The primary control[2] has special characteristics with respect to conventional bulk power systems. It is first responsible of immediately responding to power imbalances, but also of reacting to untimely transitions such as the unexpected islanding or the re-synchronization maneuvers that can heavily perturb the system operation [10]. The task of the primary control becomes more difficult in microgrids due to the lack of inertia and the volatile nature of the distributed generators [11]. In particular, microgrids are typically characterized by having all (or almost all) the resources interfaced with power electronics converters [12]. Additionally, resources have similar power ratings [13] (i.e. there is absence of a *main* generator, typically used as slack).

Voltage-source inverters (VSIs) are typically used in microgrids since they do not need an external reference to stay synchronized and can provide services like ride-through capability and power quality enhancement [14, 15]. VSIs controllers are composed by two stages, an inverter output controller and a power sharing controller [16].

In grid-connected mode, as devices are connected to a stiffer power grid, only the inverter output control is needed, where every converter follows a power reference, and the main grid operates as slack [17]. Alternatively, current-source inverters (CSI) can be synchronized using a phase-lock-loop-based synchronization method [18].

When operating in islanded mode, the standalone power balance has to be strictly respected. As in microgrids resources have similar power ratings, there is the need to share the power imbalances among them. To cope with the power sharing problem, in microgrids it is a common practice to mimic the behavior of conventional power systems with multiple generation by using droop controllers that link active and reactive power with frequency and voltage magnitude respectively [19], and to introduce output impedance control loops [20]. The basic idea of the droop control loop is to use proportional controllers to relate active power P with frequency f and reactive power Q with the local measured voltage magnitude V.

$$f = f^* - m_f(P - P^*), \tag{2.1}$$
$$V = V^* - m_V(Q - Q^*), \tag{2.2}$$

where P^* and Q^* are the references of these controllers, and m_f and m_V the proportional parameters also known as *droop parameters*.

As early mentioned, the primary control also needs to tackle unexpected transitions such as the unintentional islanding. The unintentional islanding is the most difficult condition that can affect microgrids. The ability to cope with such a transition is key for ensuring the microgrid resilience and dynamic performance [21]. The state-of-the-art on

[2]Sometines in literature also refer to as local control or real-time control

islanding/grid-tie mode transitions of microgrids is mainly based on the $P - f/Q - V$ droop controls and can be roughly divided into two categories. In the first category, rotating machines are present in the microgrid and hence there is an intrinsic inertia for reacting to the islanding transition. In the second category, most of the resources are interfaced through power converters and thus the inertia is negligible or nonexistent.

The first category is well-spread in industry by acting over the governor of diesel, steam or gas turbine based synchronous machines to modify their speed and, hence, the grid frequency. In this category the most used strategy is the Load Drop Anticipator (LDA). This method acts on a pre-selected slack unit for anticipating the maximum frequency variation that might take place after the islanding. For this purpose, the method needs to know the value of the inertia of the machine beforehand.

In the second category, enhanced droop control strategies are proposed. They usually rely on a well-sized storage system to cope with the worst possible disturbances in an islanding transition. In [22], the use of different VSI-CSI configurations is discussed. It is shown that a VSI-control strategy can be used for limiting the current output of the resource during the islanding transition so that the microgrid can succesfully transit to the islanded mode. Load shedding is not discussed. In [23], a transition scheduler is proposed where, in case of islanding, all non-critical loads are shed and PV units can be curtailed. The method shows very good results in its dynamic performance for the case under study. Unfortunately, the proposed strategy is customized for the specific case study and cannot be directly extended to any generic microgrid.

Secondary Control

As in traditional power systems, the secondary control in microgrids aims at minimizing the frequency and subsystem voltage deviations with respect to their rated values. In the case of microgrids, this is done in general by centrally modifying the droop parameters (m_f, m_V, f^* and V^* of Equations (2.1) and (2.2)), according to the state of the grid and to the pre-defined operational bounds of the controllable distributed resources.

In this level, the *programmed islanding* and the *re-synchronization* procedure take place. They focus on controlling the aggregated power flow at the connection node between the microgrid and the main grid, also called point-of-common-coupling PCC[3]. The intentional islanding aims at smoothly bringing the power flow at the PCC to zero, so that the impact on the microgrid due to the disconnection from the main grid is minimum. In general, this goal is achieved by modifying the droop characteristics of the microgrid devices as a function of the measured power flow at the PCC. Therefore, this approach needs to share a minimum amount of information among devices. Another solution, without affecting

[3]Although the original definition of the PCC comes from the idea of having and ideal (impedance-less) connection between power converters.

original droop parameters is presented in [24], where a virtual grid concept is introduced composed by a generator and a storage system that replace the role of the grid.

For the re-synchronization procedure, there are two categories. The first, and the more extensively used in literature, relies on the existence of one active device at the PCC that can control the voltage mangnitude and phase, while keeping the power balance in the microgrid. In [25], a synchronization technique that temporarily disables droop is used. A so-called *connection agent* is presented in [18], which makes use of a VSI at the PCC with minimum storage. Reference [26] shows a smooth synchronization method that uses a modified $P - V/Q - f$ droop control on a unique device *close* to the PCC.

The second category, also called *active synchronization*, looks for distributing the control among the energy resources, for steering the entire grid to meet the synchronization criteria. As an example, in [27] the active computation of droop parameters for achieving the synchronization is shown by using a central controller that has access to the PCC measurements and sends frequency and voltage offsets to the distributed resources. In [28], a strategy that also accounts for unbalance and harmonic distortion in the control variables and in the synchronization criteria is presented.

Meanwhile, reference [29] argues the need of active synchronization and shows how simple switched capacitors together with a synchro-check are enough for meeting a smooth transition.

Tertiary Control and Long-Term Energy Balance

The traditional tertiary control in power systems does not play an important role in microgrids. Instead, the tertiary control in microgrids is strictly linked to the long-term objectives of the system, and it is typically referred to as microgrid energy management system (EMS). Its main objective is to plan the lowest-cost operation of the microgrid, or in case of islanded operation guarantee the long-term availability of supply, while accounting for the uncertainty of the distributed resources (e.g. renewables).

In that sense, the scientific community has focused its efforts on a centralized approach. Two categories can be found on it: the fully centralized EMS and the distributed EMS.

In a fully centralized EMS, as in [30], [31] and [32], a central controller gets data from all resources (knowing in advance their particular nature), and performs forecasts, state-of-charge computation, unit-commitment and dispatch in order to minimize the use of fuel-based units, maximize the generation from renewables and keep the energy balance in the microgrid.

Distributed EMS are commonly accomplished by assigning particular tasks at different levels of the system, such as, at the distribution network operation (DNO), at the

microgrid central controller (MGCC) and at the local controllers (LC) [33].

A disadvantage of these approaches is that they are custom for each microgrid, and are not straightforwardly scalable.

2.2 Distributed and Decentralized Approaches in Microgrids Control and Dispatch

Distributed and decentralized approaches are typically used as equivalent terms. However, they are slightly different in the following way. In the decentralized approach, the local controllers (LC) are only linked with each other through the physical grid, and their decision process is made only based on local measurements. In the distributed approach, the LCs use local measurements and share information among them or with a central controller (CC). The main idea is that the overall problem is partitioned into several small problems that are solved locally by the LCs. A CC *may* be present in order to orchestrate the distributed decisions.

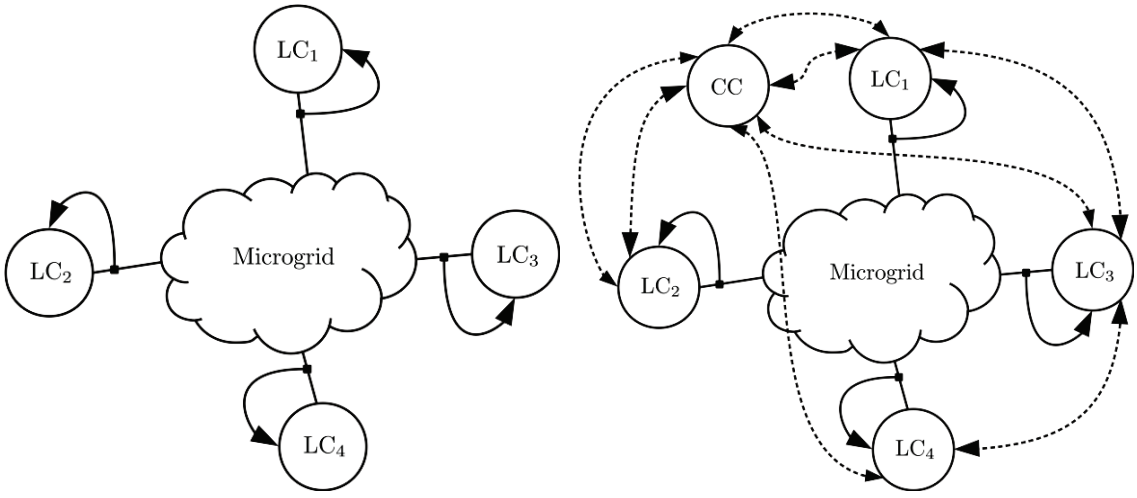

(a) Decentralized approach. (b) Distributed approach.

Figure 2.2 – Schematic representation of decentralized and distributed control approaches.

Decentralized approaches are normally found at the primary control level. In this category, the droop-based methods are well spread in real implemented microgrids, and are part of the primary source of research in the academic literature. However, the basic droop control method has several disadvantages, among which the main are [34, 16, 35, 36, 37]:

- Lack of general knowledge of the state of the energy storage devices, that can lead to non-secure and sub-optimal decisions.

- Poor performance in networks characterized by a low X/R ratio[4].
- Instability issues when choosing small droop parameters, that are desirable for keeping the deviations small.
- Disregard of the uncertain resources dynamics, that can lead to limit violations and instability.
- Poor power sharing among power converters due to output impedance uncertainties that are result of their internal control law.
- Inability to impose a fixed system frequency independent of system loading conditions.

In the following we present how the literature has proposed to tackle these issues.

2.2.1 Conventional Droop-based Methods

As presented in Section 2.1.2, the conventional droop strategy relates the active power with frequency and the reactive power with voltage magnitude, which is a good assumption in high-voltage grids. However, at lower voltage levels, the X/R ratio decreases. Indeed, in low-voltage it is typically much smaller than 1, namely, lines are characterized by being essentially resistive.

In practical implementations, this issue is usually solved by the use of an inductance or a transformer at the point of connection between the inverter and the microgrid (see Figure 2.3), that also plays the role of filter [38]. This element will increase the equivalent X/R ratio and the controlled power flow is the one at the power electronics output, enabling the decoupling of the $P - f/Q - V$ controls.

In general however, the active and reactive power are both related with voltage and frequency deviations [20, 39], due to the impedance between the converter output and the grid.

A first approximation of a solution is presented in [40], where a *rotational transformation matrix* is introduced, that accounts for the full link between control and controlled variables. The control law is kept almost the same

$$f = f^* - m_f(P' - P^*), \tag{2.3}$$
$$V = V^* - m_V(Q' - Q^*), \tag{2.4}$$

[4] X and R here indicate real and imaginary parts of the lines longitudinal impedances.

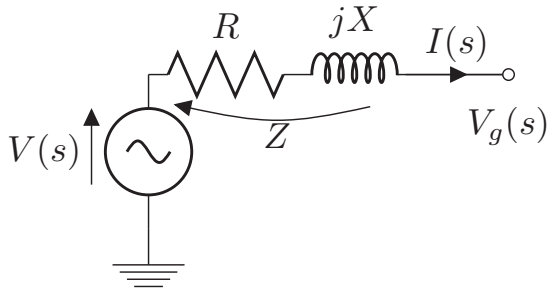

Figure 2.3 – Converter output impedance equivalent diagram.

where P' and Q' are computed as

$$\begin{bmatrix} P' \\ Q' \end{bmatrix} = \begin{bmatrix} X/Z & -R/Z \\ R/Z & X/Z \end{bmatrix} \begin{bmatrix} P \\ Q \end{bmatrix}, \tag{2.5}$$

being P' and Q' the so-called *modified* active and reactive powers, while X, R and Z are the inductance, resistance and overall impedance viewed from the converter side as shown in Figure 2.3. In Figure 2.4 (adopted from [40]), a graphical representation of this transformation is schematically shown.

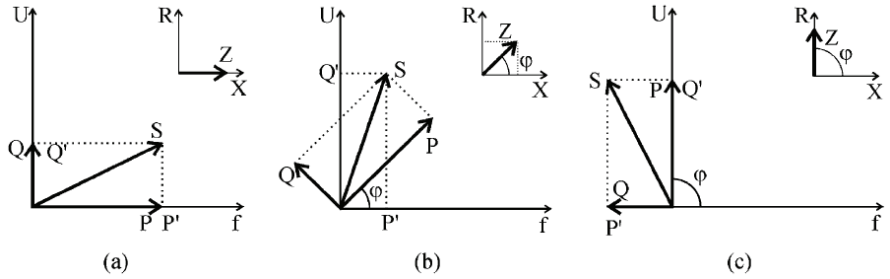

Figure 2.4 – Phasor representation of the effect of coupled droop control laws. (a) $R/X = 0$, (b) $R/X = 1$, (c) $R/X = \infty$.

Additionally, as the equivalent impedance seen by converter will not only be affected by passive elements (filters, lines), but also by the internal control laws of the converter, a further improvement is to add an outer impedance loop [41, 42]. This approach is also know as *virtual impedance* control. The virtual impedance loop modifies the voltage reference of the internal control loop, to follow a given desired behavior [43, 44] (see Figure 2.5), represented in the Laplace domain with the following equation.

$$V_{ref}(s) = V(s) - Z_v(s)I(s), \tag{2.6}$$

where V is the voltage given by the droop control, Z_v the virtual impedance, I the output current and V_{ref} the modified reference voltage.

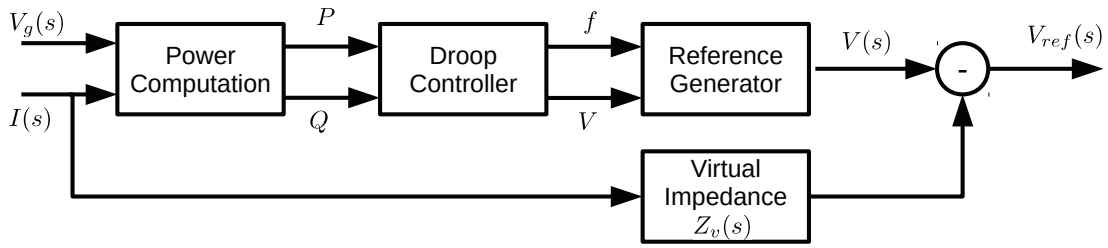

Figure 2.5 – Output impedance control loop. V_g is the measured grid voltage.

Usually, the virtual impedance Z_v is chosen such that the total equivalent output impedance is mainly dominated by this control loop [14]. In the opposite case of the basic formulation, this implementation leads to the possibility of designing $P-V/Q-f$ droop controllers for purely resistive impedance [45, 46]. This may be useful in the general case, since this virtual impedance has no power losses [47].

2.2.2 Advanced Droop-based Methods

In order to cope with the instability issues and the lack of knowledge of the behavior of the uncertainty and the state of the storage devices, improved droop-based methods have been proposed in literature.

As for stability, a modified droop strategy is proposed in [48], for resistive output impedance, that can in general be written in the PD controller form

$$f = f^* - m_f(P' - P^*) - \hat{m}_f \frac{dP'}{dt}, \tag{2.7}$$

$$V = V^* - m_V(Q' - Q^*) - \hat{m}_V \frac{dQ'}{dt}, \tag{2.8}$$

with $\hat{m}_f$ and $\hat{m}_V$ are the gains for the derivative term. This formulation leads to a PI controller in the power angle ($2\pi f = \omega = d\delta/dt$). A slight improvement is presented in [49], where $\hat{m}_f$ and $\hat{m}_V$ are adaptive transient gains that are computed on-the-fly by using pole placement techniques given the updated measurements. A supplementary droop control loop in $P-f/Q-V$ droop scheme, that only affects the non-DC component of the measured power, is proposed in [50]. It shows satisfactory power sharing and stability behavior, but depends on a non-trivial computation of the different droop control gains.

When the controlled resources are storage systems, the power flexibility that they can offer to the microgrid changes as a function of their state-of-charge (SoC). This information is typically neglected by the distributed droop control. Indeed, the classical recommendation for the computation of the droop parameters in its basic form is:

$$m_f = \frac{\Delta f_{max}}{\Delta P_{max}}, \quad m_V = \frac{\Delta V_{max}}{\Delta Q_{max}}, \tag{2.9}$$

where Δf_{max} and ΔV_{max} are the maximum expected variations of frequency and voltage respectively, while $\Delta_{max}P$ and $\Delta_{max}Q$ are the maximum possible operational ranges of the controlled resources, which also represent their flexibility. In storage systems, as being characterized by having bi-directional power flow, a common practice is to set these values to twice the maximum power $m = 2P_{max}$, $n = 2Q_{max}$. However, the active power flexibility is dynamic and it is strongly dependent on the storage SoC. Indeed, when reaching the energy storage bounds (fully-charge or depletion) the flexibility is strictly limited to half of the power, and therefore the droop parameters have to be saturated. For instance, if the storage is fully charged (SoC= 1), the available flexibility lies in the range $[0, P_{max}]$ and the droop parameter is saturated so that the active power is *zero* for a positive frequency deviation ($f > f^*$).

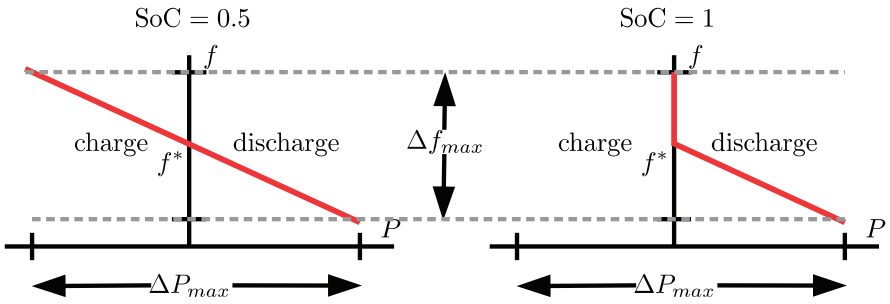

Figure 2.6 – Saturation of droop parameters given by the reduced flexibility of a storage resource. For this example, as it is commonly used, the reference power was selected as $P^* = 0$.

To avoid saturation and allow a smooth computation of the droop parameters, SoC-based droop strategies have been proposed in literature [51, 52]. With these, the droop parameters for storage converters can be computed locally and continuously.

Decentralized approaches, have been also adopted in secondary control. As an example in [53] a PSO-fuzzy controller is proposed in order to compute adaptive gains of the droop controller.

2.2.3 Droop-Free Methods

One last category of decentralized techniques searches to solve the control problem without the use of droop-based strategies. In this category, decentralized multi-agent-systems (MAS) are mainly found, where agents communicate with each other (without the use of a central controller), and take decisions on its own. The decisions are not based on voltage or frequency deviations, but on power and voltage set-points computed as a function of the state of the other agents.

In [54] and [55], a decentralized robust control strategy is proposed that is formulated as

a servomechanism problem [56][5]. It needs a initial analysis of the microgrid flexibility to define the control parameters. Thus, it is not scalable.

A wireless-based multi-agent coordination method is proposed in [57], and a self-organizing architecture method in [58]. Both of them compute the control mechanism by using concensus theory.

In [59] the coordination mechanism is formulated as a social welfare maximization problem, that includes a special agent (not central) corresponding to the network operator. This method is framed in the secondary control level.

Two distributed and partially centralized voltage control strategies are proposed in [60]. They first cluster the grid into small interconnected subsystems where there is one energy storage system, which is then responsible for solving an optimization problem that reduces the voltage deviations in its neighboring nodes.

In [61], a distributed primary voltage and frequency control is presented and a method that depends on the communication network topology is proposed in [62]. In both cases, agents that are closely connected will receive continuous updates of the neighbors nodal power flows, in order to compute their own. These two last methods are specifically focused on keeping the system state in safe conditions, but they are not able to take advantage of the entire flexibility of the various resources steering them to their particular desired operational state. This task is forwarded to a general secondary control strategy.

2.3 Fully Centralized Approaches for Microgrids Control and Dispatch

The literature on fully centralized microgrids control in the presence of stochastic generation tackles the problem by using two main approaches. The fully centralized approach is characterized by strictly depending on a CC, that is in charge of solving the overall problem. It gets all the needed information from the LCs and sends operational set-points for them to implement. The LC only has the task of adopting the requested set-point. For this reason, fully centralized approaches normally work in the minutes time-range, and is typically used for planning stages (see Figure 2.7, partially adapted from [31]).

We present two separated categories, although some of the strategies here discussed use both approaches.

[5]The goal of a servomechanism problem is to find a decentralized controller so that certain outputs of the system asymptotically track given reference inputs independent of any external disturbances which may affect the system, and independent of any variations in the plant parameters and gains of the system.

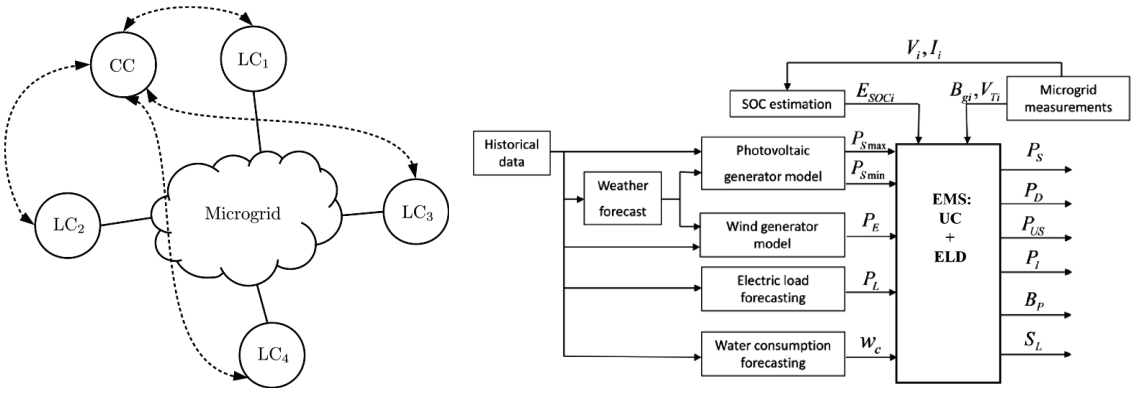

(a) Fully centralized approach. (b) Typical decision process of a fully centralized approach

Figure 2.7 – Schematic representation fully centralized control approaches.

2.3.1 Optimal Control/Dispatch based Methods

The first type of approaches relies on the possibility of quantifying and using the statistical distributions of both the stochastic generation and the loads in a central controller/dispatcher. In general, the controller/dispatcher is responsible for the solution of an optimal dispatch problem constrained by the grid operation limits.

For example, an intra-day two-stages scheduler is proposed in [63], that accounts for the resources uncertainties and the presence of on-load-tap-changer (OLTC) transformer. The paper shows a method for simplifying the mixed-integer-linear-program (MILP) into a iterative procedure using voltage and current sensitivity coefficients.

In [64], a scheduling of microgrid resources is proposed; it accounts for the stochasticity of the renewable generation (wind) and specific loads (plug-in vehicles) by means of a brute-force scenario-generation and reduction based on a-priori known statistical distributions of these stochastic variables. In [65], it is proposed to solve the microgrid dispatch problem together with its optimal configuration assessment, by representing the stochasticity of renewable resources/loads via a forecasting tool based on the support vector regression technique. The authors of [66] propose a power scheduler aimed at minimizing the microgrid net cost, where the utility of the dispatchable loads accounts for the worst-case transaction cost inferred from the uncertainties in the renewable generation.

In [67] the stochasticity of renewable generation is faced by using a Model Predictive Control (MPC) strategy when coupling traditional space heating sources with combined heat and power units to achieve *energy replacement*. A MPC-based secondary voltage control is proposed in [68], which can robustly steer the system voltages after extreme operation conditions.

2.3.2 Centralized MAS

The other approach discussed in the literature for centralized approaches relies on multi-agent-systems (MAS). As an example, reference [69] presents and gives a comprehensive analysis of the way such systems are typically used in power systems. In this context, MAS are proposed as a step towards the distribution of control. Note that we differentiate between decentralized and centralized MAS, while the first was presented in Section 2.2, the second relies on the presence of a centralized agent that receives messages from followers, solves an overall problem and sends messages back to the followers.

Optimization goals in previously proposed methods, like in [70] and [71], consider the operational costs of the system without accounting for the operational constraints such as voltage magnitudes or line congestions. More precisely, the MAS approach presented in [71] relies on the availability of droop control that is suitably adjusted by MAS negotiations. However, this method neither expresses the specific state of the resources nor considers the grid state to ensure an appropriate grid Quality-of-Supply (QoS) and a feasible operation of the grid.

The authors of [72] present a centralized control scheme that uses MAS for generation scheduling and demand-side management for secondary frequency regulation, in order to optimize the operational cost of a microgrid in both grid-connected and islanded modes. However, the method proposed there does not account for the operational constraints associated with the grid and, also, does not take into account the sub-second time constraints associated with the short-term volatility of stochastic resources. Therefore, this method does not appear to be a *real-time* control strategy.

The case of the post-fault microgrids behaviour is discussed in [73] along with the design principles of a corresponding MAS-based real-time control method. In particular, the proposed method is designed to achieve fast load-shedding strategies in order to maintain the real-time power balance of the microgrid and, as a consequence, avoid its collapse. The paper does not discuss the use of the MAS with respect to the optimal operation of the grid in normal operating conditions. Additionally, similarly to the other references, the proposed method does not express the internal state of the resources to the other agents and it is not scalable.

A virtual droop control approach is presented in [74], that looks at centrally computing droop parameters in order to optimally steer the system to safe and efficient operation regions. It relies on the knowledge of the specific details of the resources of the microgrid and does not consider line congestion management. On the contrary, a *top-dowm* unified framework for primary and secondary frequency controls and congestion managment has been recently presented in [75], it distributes an overall optimization problem into the various resources for primary control, and computes a centralized decision for secondary control. Indeed, in this approach the problem distribution is strictly dependent on

the nature of the problem itself and, therefore, changing the objective will require a re-engineering of the distribution of the control, which threatens its scalability.

2.4 Contributions of the Thesis in View of the Literature Review

The proposed approach underlined in this thesis shows several advantages with respect to literature ones.

1. First, the framework is based on a unified and abstract representation of devices and subsystems, key element for simple and straightforward design.
2. Second, the approach is composable, i.e., entire subsystems can be abstracted in the same way of a device. This characteristic makes the approach fully scalable from low-voltage microgrids to medium-voltage distribution networks.
3. Third, we target stringent real-time control. Specifically, we propose a formal approach capable to close the agent negotiation and deployment of control set-points in sub-second time-scales.
4. Fourth, we eliminate the constraint that distributed approaches cannot be adopted for primary voltage and frequency control.
5. Fifth, the control framework can be coupled with long-term energy management objectives enabling optimal decoupling of the real-time control and the dispatch problems.

3 A Composable Framework for Real-Time Control of Active Distribution Networks, Using Explicit Power Set-Points

Chapter Highlights:

We devote this chapter to the formal presentation of a novel real-time control framework called COMMELEC, *A Composable Framework for Real-Time Control of Active Distribution Networks, Using Explicit Power Set-Points*. Our framework is designed to be robust, scalable and able to exploit the flexibility of each energy resource in the grid, and account for their willingness and uncertainty at deploying a given set-point.
The framework is presented for the specific case of microgrids. Therefore, we discuss its use for a microgrid in grid-connected mode, a microgrid in islanded mode, and how to handle the transitions between both modes.
We emphasize the theoretical description and propose methods for coping with the real-time need of such a control strategy.

3.1 Situation Awareness and Working Hypothesis

The current structure of power grids is essentially composed of a number of electrical subsystems interconnected at different voltage levels. Each subsystem comprises *electrical grids* and *resources*. These latter elements could be clustered, in general, into three categories: loads, generators and storage devices.

We base our framework on the following working hypothesis: If in distribution networks it is possible to expose to a *grid controller* the state of each subsystem (resource and/or electrical grid), then, in principle, it is possible to find an admissible and stable system-equilibrium-point that exploits at maximum the grid flexibility while respecting its operational limits. We suppose that we have available a situation-awareness metering system, capable of informing at a high frame-rate and low latency about the state of the controlled grid.

Note that the state of a subsystem can rapidly vary, specially in the presence of volatile renewable generation. Hence the need for a framework that is at least as fast as the fastest power variation possible that can take place in a resource. This feature could enable the graceful operation of a *microgrid* in both islanded and grid-connected operation modes, thus enabling, for this last one, the possibility of quantifying the amount of ancillary services to the upper grid (i.e., primary and secondary frequency control support, as well as voltage compensation). Directly controlling every resource, however, is clearly too complex when resources are numerous and diverse.

We focus on distribution networks as a microgrid is, in our opinion, the smallest subsystem where such a control framework can be deployed. For this reason, in the following the definition of the framework is focused on microgrids, but as it will be discussed, it is not limited to that application.

3.2 General Definition for a Grid-tie Microgrid

The COMMELEC framework steers a set of energy resources in a power grid using explicit (P, Q) power set-points, for active and reactive power, respectively.

We define, based on a multi-agent approach, a *scalable* framework for the direct and explicit control of real-time nodal power flows with the following features:

(a) *Abstract Framework.* It applies to all electrical subsystems and specifies their capabilities, expected behavior, and a simplified view of their internal state. The existence of a common abstract framework is an essential step for scalability and composability. Such a framework was applied, for example, to the control of very large and heterogeneous communication networks [76].

(b) *Composition of Subsystems.* It is possible to aggregate a set of interconnected elements into a single entity. In this sense, a local grid with several generation sources, storage facilities and loads can be viewed by the rest of the network as a single resource.

(c) *Separation of Concerns.* Controllers that are responsible for resources are specific but their function is simple, as it is limited to (i) mapping the internal state of the resource and expressing it in the abstract framework and (ii) receiving and implementing power set-points from the agent with which they communicate. In contrast, controllers that are responsible for grids, manipulate only data expressed by means of the abstract framework and do not need to know the specific nature of the resources in their grid. In other words, controllers that need to know details of diverse systems are simple-minded, whereas controllers that need to take intelligent decisions have an abstract, simple view of the grid and of their resources.

3.2.1 Grid Agent and Resource Agents

We use software *agents*, i.e., pieces of software that are able to speak for, and control a resource or a set of electrical systems. An agent can be implemented in a stand-alone processor, as a process on a control computer, or in an embedded system. Small systems such as appliances, boilers or small photovoltaic roofs, do not necessarily need to have a specific agent. Instead, they can be controlled and represented by one single group-aggregating agent that uses a broadcast protocol such as GECN [77, 78]. An agent that controls an entire grid is called *grid agent* (GA); other agents are called, in general, *resource agents* (RAs). Agents follow the hierarchy of distribution and transmission networks.

Note that a grid agent can communicate with several resource agents, to which it will send set-points, but with only one grid agent, from which it will receive set-points.

We assume that a GA receives measurements that, from the grid under its responsibility, are used to estimate the electrical state. The measurement messages are sent periodically, with a period for instance, of $\tilde{T} = 20$[ms]. Such a time period is compatible with the data frames of modern monitoring systems equipped, for instance, with phasor measurement units (PMUs). These devices typically provide synchrophasor measurements ranging from 10 to 60 frames-per-second, as required by the IEEE Std. C37.118 [79, 80]. Examples of time latencies and accuracy of real-time state estimation processes fully based on PMU data are discussed in [81, 82, 83]. Typical time latencies of less than one hundred milliseconds can be achieved in order to determine the system state with relevant refresh rates of some tens of milliseconds.

For example, in Figure 3.1 we show a LV distribution network with a high penetration of renewable resources and the presence of storage units, in which all the aforementioned elements are presented. A bidirectional communication link is needed between agents,

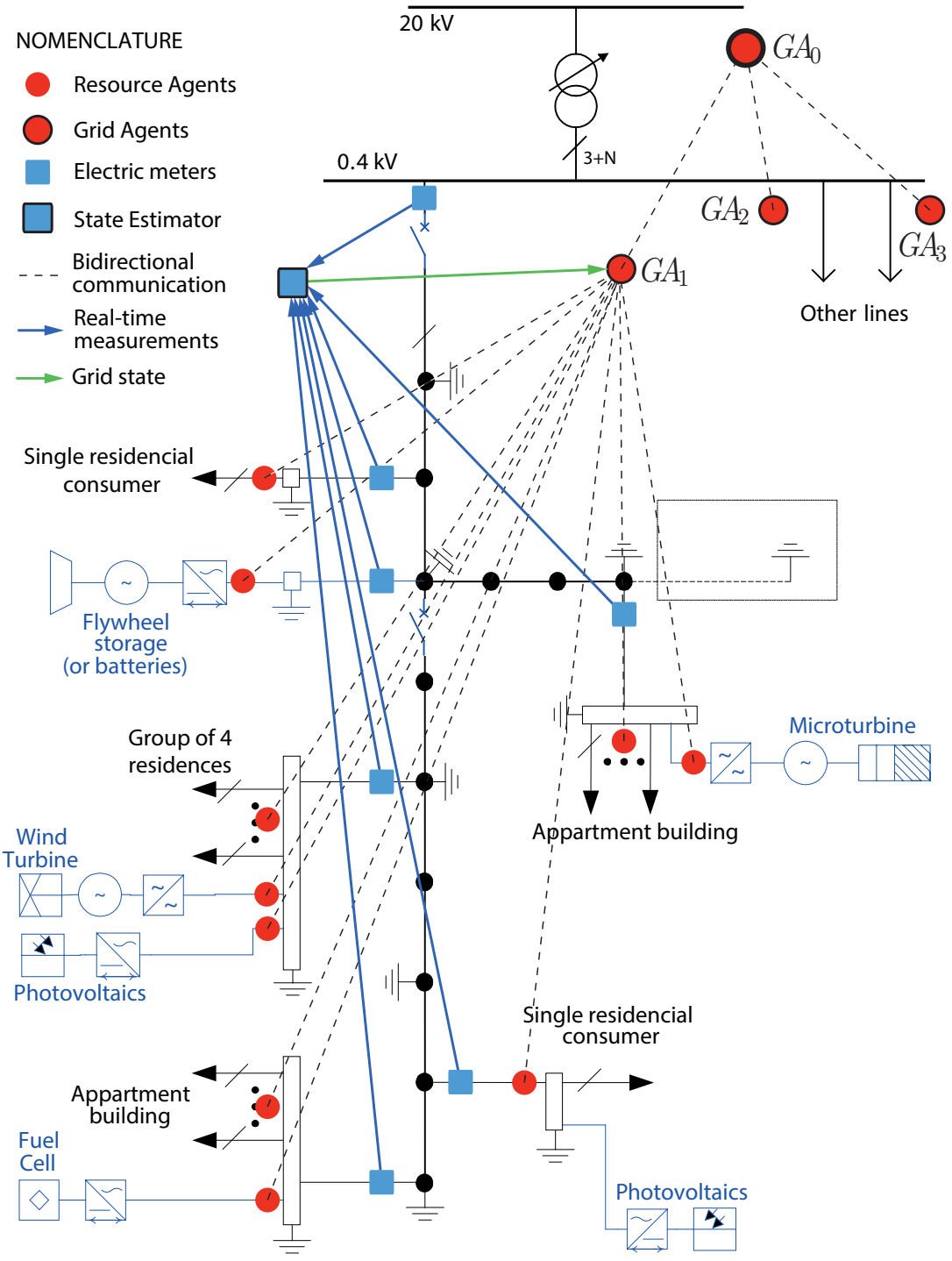

Figure 3.1 – A general view of the elements in the COMMELEC framework. The diagram is based on the CIGRÉ LV microgrid benchmark

whereas measurement units stream data to a state-estimation process that, on its part, sends an updated grid-state to the grid agent of this microgrid. Two additional grid

agents, related to two other feeders (microgrids) connected at the 0.4kV, bus are also communicating with a main grid agent at the MV grid level.

The advertisement/request protocol used by agents is as follows.

1. RAs periodically advertise an abstract view of the internal state of the resource or grid under their control, in terms of three quantities: the PQ profile $\mathcal{A}$, the belief function $\mathcal{B}$ and the cost function $\mathcal{C}$. Details on the definition of each element are presented in Section 4.11.4.
2. A GA has knowledge of the state of its electrical grid and uses the information received from RAs, together with the requested set-points from an upper GA, in order to compute the requested power set-points (Section 3.4.4) that are then sent to the RAs.
3. Upon receiving the requested set-points RAs set, if possible, their operation according to the requested set-points and respond with a new advertisement that also serves as a confirmation that the set-points were set.

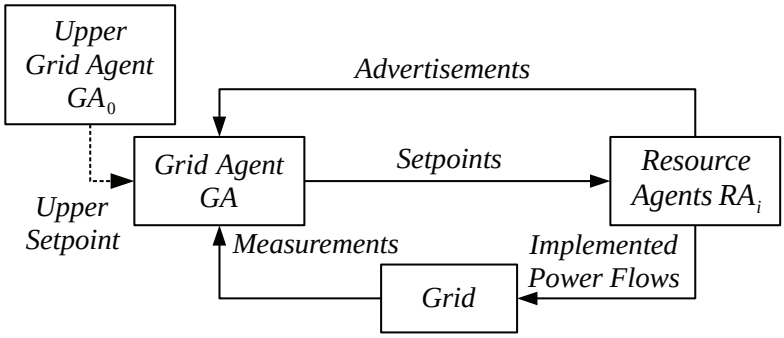

Figure 3.2 – Decision process performed by the GA

The process presented in Figure 3.2 is repeated periodically every T time units, where T is a value short enough to cope with the fastest volatility of distributed resources and large enough to be compatible with the need to estimate the electrical state of the grid.

3.2.2 On the Hierarchy and Synchronism of Agents

Observe from Figure 3.1 that the hierarchy of agents follows a tree structure, where we can find *leaders* and *followers*. Leaders send set-points to followers and followers send their advertisements to leaders: this setup is repeated at any level of hierarchy. Note that this architecture enables the scalability of the framework, as every leader and any follower behaves in the very same way.

In the particular case presented in Figure 3.1 and summarized in Figure 3.3, every resource

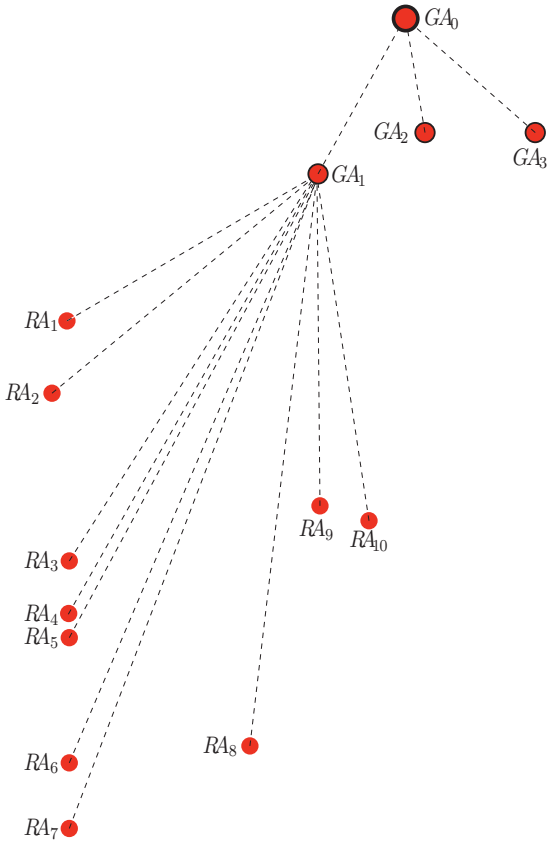

Figure 3.3 – Agents hierarchy taken from Figure 3.1

agent RA_i is a follower of GA_1. GA_2 and GA_3 are at the same hierarchy level as GA_1 and all three are followers of GA_0. In general, resource agents are always followers, whereas grid agents can take both roles. Note that for simplification the followers of GA_2 and GA_3 are omitted.

The framework was conceived to minimize the level of synchronism among agents. Indeed, according to the voltage level of electrical grids, we consider that the hierarchy of the agents follows the hierarchy of power grids. In this respect, it is expected that at higher hierarchy level we find resources with higher inertia, and therefore, decisions can take longer.

In general, a follower computes an advertisement just after receiving a set-point, whereas a leader will compute new set-points only after receiving all followers' advertisements. This is shown schematically in Figure 3.4. Observe that, in the case of GA_1, both computations take place but they are performed asynchronously, even when they depend on each other. We present in Section 3.2.4 how to handle the dependency among the processes in an asynchronous way.

The description of the content of both advertisements and request messages is given in

the following sections.

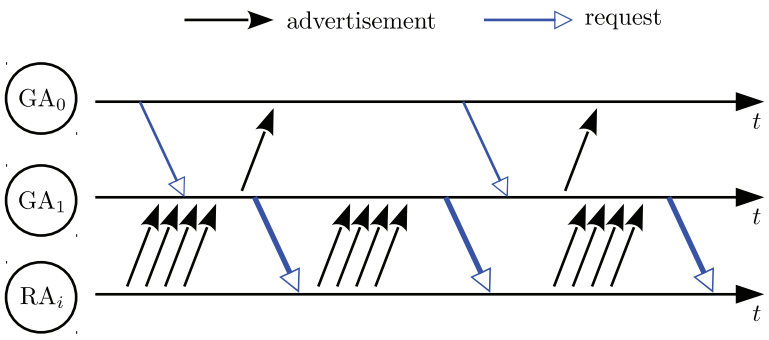

Figure 3.4 – Agents time synchronism diagram

3.2.3 Advertisement Messages

Any agent, regardless of its nature and internal details, periodically sends an abstract message $(\mathcal{A}, \mathcal{B}, \mathcal{C})$ to its leader. The information contained in this advertisement represents all the necessary elements to safely steer a grid in real-time.

First, we introduce some nomenclature and conventions,

- P and Q values, for active and reactive power, respectively, are treated as injections/absorptions to/from a node;
- negative power (active or reactive) means consumption, positive power means production;
- index i is used for resource agents. i can go up to an arbitrary $n > 0$ that represents the number of resource agents.

In the following, we describe each element of the advertisements.

PQ Profile $\mathcal{A}$

An agent advertises a region in the (P, Q) plane that the subsystem under its control can deploy. More precisely, $\mathcal{A} \in \mathbb{R}^2$ is the set of (P, Q) values that this subsystem can safely implement for a predefined time-window. This set can be, for instance, associated with the well-known PQ capability-curve diagram of a synchronous machine. The difference would be that this set, in general, constantly changes according to the state of the resource. In Figure 3.5, we show an example of a generic PQ profile.

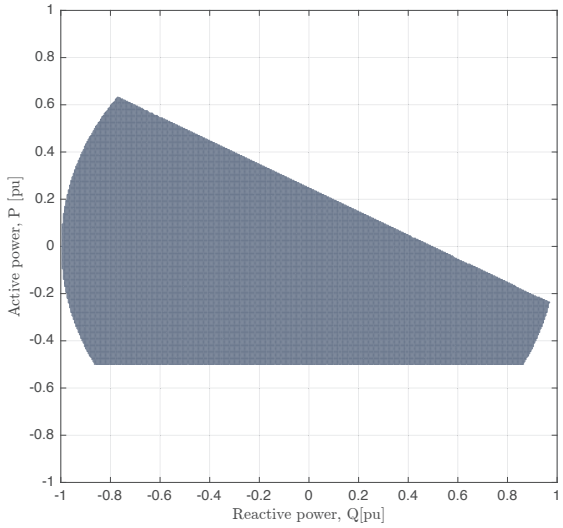

Figure 3.5 – Illustration of a generic PQ profile $\mathcal{A}$

Belief Function $\mathcal{B}$

An agent also advertises the *set-valued* function $\mathcal{B} : \mathcal{A} \to \mathbb{R}^2$. This function returns the set of all possible power flows that this resource might implement for a given set-point. Formally, we call $\mathcal{B}$ the belief function of an agent that receives a request to implement a set-point (P, Q); then the implemented power flow (P', Q'), which this subsystem does implement, lies in the set $\mathcal{B}(P, Q)$ with overwhelming probability.

$\mathcal{B}$ accounts for the uncertainty. For instance, in Figure 3.6 different cases are presented. $\mathcal{B}(P_1, Q_1)$ could represent an oscillating behavior around the requested set-point (P_1, Q_1), $\mathcal{B}(P_2, Q_2) = \{(P_2, Q_2)\}$ is, for example, the case of a highly controllable device, such as a battery or generator. Whereas $\mathcal{B}(P_3, Q_3)$ represents a generic deviation from the requested set-point, which results always in an implemented set-point inside $\mathcal{A}$. Larger sets can be found, for instance, in devices where there is no information available; then, any power implementation could occur from one time-step to another. In practice, it is desirable to have small belief-sets, hence it is highly recommended the use of forecasting tools to reduce the uncertainty.

It is important to underline the difference between $\mathcal{A}$ and $\mathcal{B}$: the former indicates the deployable set-points that this resource *can* implement, whereas the latter indicates all the possible operating conditions that *might* result from applying a requested set-point due to the stochasticity or the nature of the process controlled by the resource agent.

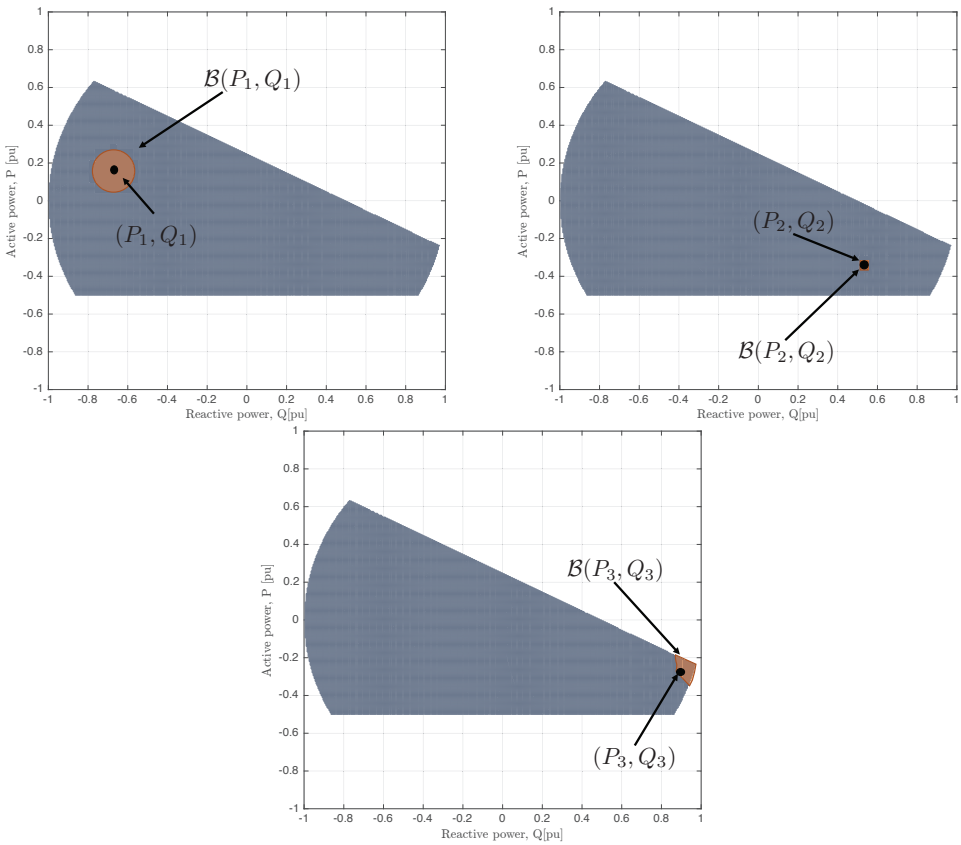

Figure 3.6 – Illustration of a generic belief function $\mathcal{B}$ for different set-points, defined in the domain $\mathcal{A}$ of Figure 3.5. The requested set-point is represented with the black dot while the belief-set is in orange.

Virtual Cost $\mathcal{C}$

In addition, the agent also advertises $\mathcal{C} : \mathcal{A} \to \mathbb{R}$. The virtual cost is interpreted as its own cost of implementing a requested power set-point. Note that, this virtual cost does not make reference to a real electricity cost. On the contrary, its role is to quantify the propensity of this resource to deploy (P, Q) set-points within particular zones of the PQ profile. For instance, if a storage system is close to being fully charged, its agent advertises a low cost for producing power and high cost for consuming power, thus signaling to the grid agent that the storage system would prefer to be discharged.

As a simple example, Figure 3.7 shows the cost function $\mathcal{C}(P, Q) = P^2 + Q^2$ defined for the domain of $\mathcal{A}$.

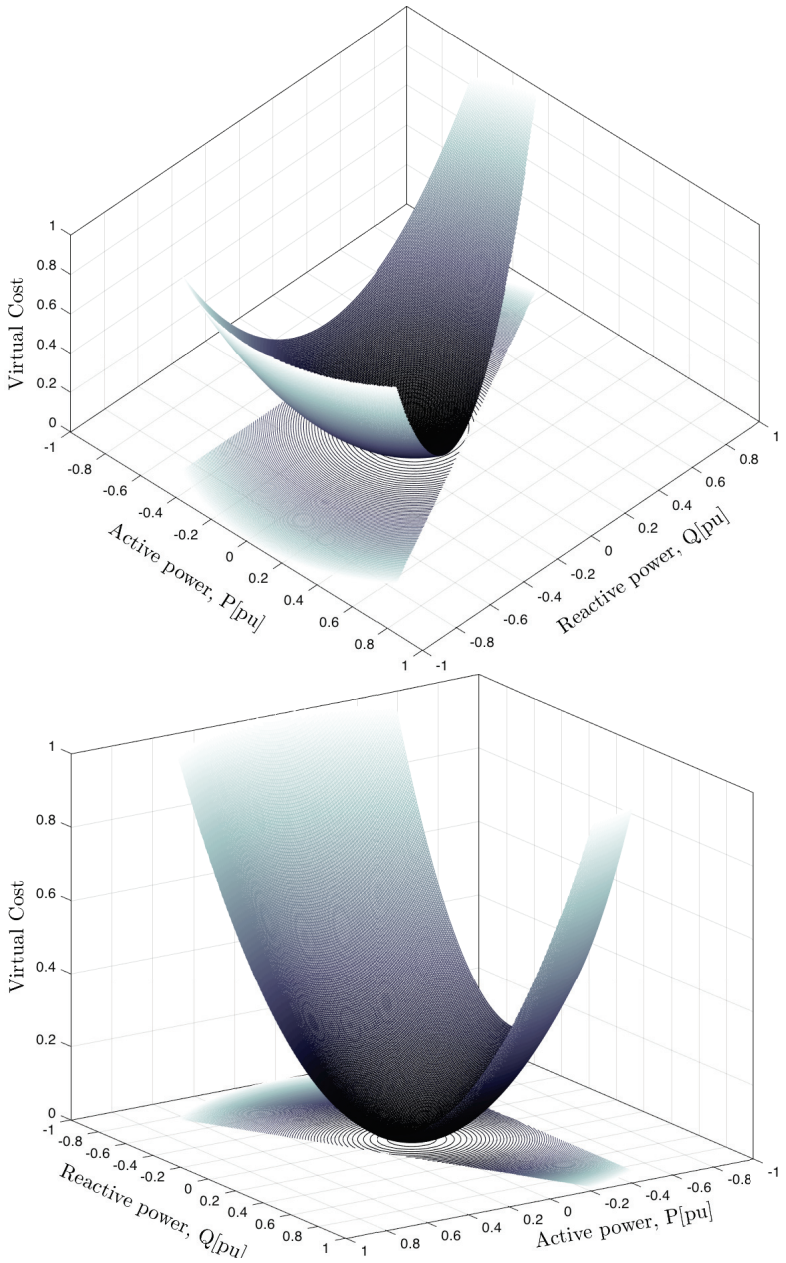

Figure 3.7 – Example of a generic virtual cost $\mathcal{C}$, defined in the domain $\mathcal{A}$ of Figure 3.5.

Valid Approximations of PQ Profiles and Belief Functions

As our goal is to develop a *real-time* control system, we use simplifications. A simplification is valid only if it maintains the grid in a feasible electrical state. In this sense, any simplification must satisfy the following property:

Definition 3.2.1 (Validity Property for PQ profiles and Belief Functions)**.** $(\mathcal{A}, \mathcal{B})$ *is a valid pair of PQ profile and belief function for a given resource if, whenever it receives a target set-point* $(P, Q) \in \mathcal{A}$*, its actual implemented power flow lies in the set* $\mathcal{B}(P, Q)$*.*

Consequently, a grid agent can simplify its computation by using approximations of the advertised PQ profiles and belief functions, instead of those are were received, as long as the approximation satisfies the validity property. In particular, if we replace an original PQ profile by an approximating *subset* and a belief function by an approximating *superset*, then the approximation is valid.

3.2.4 Request Set-Points: Grid Agent Decision Process

In this section, we describe in detail the decision process performed by the Grid Agent (GA) as illustrated in Figure 3.2. Consider that GA is responsible for a grid-tie microgrid in which there are n resources, and that it receives periodical requests from GA_0 that is responsible for controlling a MV grid. Next, we indistinctly call the point of connection between the microgrid and the MV grid the LV-MV bus or the PCC (point-of-common-coupling).

At every computation step, the GA has received the *advertisement messages* from all RAs, the target set-point (P_0, Q_0) from GA_0 and an estimation of the electrical state of the grid. The goal of the GA is then to *steer*, using frequent updates, the electrical state of its grid by explicitly setting the power set-points so that (i) the virtual costs of the followers are minimized, (ii) the set-point (P_0, Q_0) is satisfied as much as possible and that (iii) the grid is in a *feasible state of operation*, as defined next.

Feasible State of Operation

The *electrical state* of a power grid is given by the set $\{\delta_k, V_k\}$ representing the voltage angles and magnitudes at different buses k, respectively. We assume that the GA has the means to estimate the electrical state of its grid with a sufficient refresh rate that is compatible with the frequency of power set-points updates.

We say that an electrical state is *feasible* if it satisfies static conditions on voltage and currents, of the form

$$V_k \in [V_k^{nom} - \beta_k, V_k^{nom} + \beta_k], \quad I_\ell \leq I_\ell^{\max} \tag{3.1}$$

where V_k^{nom} is the nominal voltage value of V_k (which depends on the voltage rating of the GA grid), I_ℓ is the current magnitude at a line[1] $\ell = (k, k')$, and β_k and $I_\ell^{\max}$ are given threshold variables.

Note that, for the sake of clarity, the concept of *feasible electrical state* defined by (3.1) has been intentionally simplified to include only these steady-state feasibility conditions. This

[1] If the current getting into line (k, k') is different from the one getting into line (k', k), I_ℓ is the maximum among them.

concept can be further extended to take into account other conditions that formalize the *dynamic stability* of a grid, such as voltage and angular stability. In this respect, recent literature has discussed the stability aspects of microgrids in the case of constant-power flows actuated by modern power electronics (e.g., [84] and [85]). Although this aspect goes beyond the scope of this work, it is worth remarking that for this specific case, as the GA is assumed to know the state of the grid, it also knows the admittance matrix of the system [82]. As a consequence, it can formally compute the frequency-domain input impedances in the correspondence of each node where the resources are connected. Therefore, the GA can potentially use this information to augment the computation of the feasible electrical state of the grid, hence include further stability requirements.

We are interested in radial distribution networks, in which it is known that the load-flow problem has a unique solution if voltage magnitudes are close to nominal values [86, 87]. We consider a grid operating in this regime. In particular, we assume that the voltage magnitude bounds β_k are small enough to guarantee the uniqueness of a solution to the load-flow and that it contains a margin compatible with the accuracy of state estimation. This implies that the electrical state of the grid and the power flow at the LV-MV bus are uniquely determined by the power flows $(P_1, Q_1, ..., P_n, Q_n)$ and the voltage (δ_0, V_0) at the slack bus that for this case is assumed given for slack bus convention.

Admissible Target Set-Points

We control the power set-points at all resources, which therefore enable us to control the electrical state of the grid. However, the actual power set-points implemented by this resources can differ from targets, and this is captured by the belief functions. This suggests the following definition.

Definition 3.2.2 (Admissible Target Set-Points)**.** *We say that a collection of target set-points $(P_1, Q_1, ..., P_n, Q_n)$ is admissible if, for any actual implementation, $(P', Q') \in \mathcal{B}(P, Q)$, the resulting electrical state is feasible. We denote the admissible set by $\mathcal{U}$.*

Formulation of the Grid Agent Objective Function

The purpose of GA is to compute the collection $u = (P_1, Q_1, ..., P_n, Q_n)$ of target set-points that are admissible following Definition 3.2.2. In order to do so, the received virtual costs are aggregated by means of the weighted total cost

$$C(u) \triangleq \sum_{i=1}^{n} w_i \mathcal{C}_i(P_i, Q_i), \tag{3.2}$$

where $\mathcal{C}_i(P_i, Q_i)$ is the virtual cost function of follower i, and the weights $\{w_i\}$ express the preference of GA of one follower over another.

The computation of the weights is not discussed here. We simply mention that, in general, this computation will depend on the overall goal of a particular grid. For instance, if a grid is willing to provide services to the grid, the weights will be computed such that the resources will participate according to their flexibility. In what follows, we assume that the weights are pre-computed based on the prior knowledge aboutthe followers and that they are fixed during the system operation.

Furthermore, we add a penalty term that represents the constraints on the power at the LV-MV bus. For example, here we use the quadratic function

$$J_0((P_0,Q_0),(P_0(u),Q_0(u))) = J_0(u_0,X_0(u)) = w_0((P_0-P_0(u))^2+(Q_0-Q_0(u))^2), \quad (3.3)$$

for $w_0 > 0$, where $u_0 = (P_0, Q_0)$ is the request sent by GA_0 and $X_0(u) = (P_0(u), Q_0(u))$ is the resulting power flow through the bus when the collection of power flows at the resource buses is given by u.

Finally, a penalty term $J(u)$ is added to capture the distance of the electrical state to the boundary of the feasible state region. Following the discussion of Section 3.2.4, here we propose an example of a function defined in terms of both threshold variables β_k and $I_\ell^{\max}$. $\beta_k = \beta$ is considered constant (e.g., 10% of the nominal voltage), whereas $I_\ell^{\max}$ might change dynamically and depends on the physical characteristics of the line conductor. With all, J is defined by

$$\begin{aligned} J(u) &\triangleq \sum_k \frac{(V_k(u)-V_k^{nom})^2}{\beta^2-(V_k(u)-V_k^{nom})^2} + \sum_\ell \frac{I_\ell(u)^2}{(I_\ell^{max})^2 - I_\ell(u)^2} \\ &\quad \text{if } \{V_k(u), I_\ell(u)\} \text{ satisfy (3.1)} \\ &= \infty \text{ otherwise.} \end{aligned} \quad (3.4)$$

In the above $V_k(u)$, $I_\ell(u)$ are the voltage and current magnitudes that result from the load-flow solution when the collection of power flows is given by u.

Ideally, GA would like to find a collection of target set-points u that (i) is admissible (as per Definition 3.2.2) and (ii) minimizes

$$F(u) = C(u) + J_0(u) + J(u) \quad (3.5)$$

over all admissible u.

Solution of the Grid Agent Objective Function

Knowing that Equation (3.5) is not easy to solve, and in order to comply with the timing needs of a real-time control scheme, we propose to steer the power injections in the direction of the optimum of Equation (3.5), using a *gradient descent approximation*. More precisely, the decision process at the grid agent computes

$$u = \mathcal{P}_{\mathcal{U}}[\hat{x} - \alpha \nabla F(\hat{x})], \tag{3.6}$$

where $\mathcal{P}_{\mathcal{U}}$ is the Euclidean projection onto the admissible set $\mathcal{U}$, $\hat{x}$ is the estimated power set-point, (obtained from the state estimation process), and α is the gradient step-size parameter.

Again, we do not discuss here the optimal value of α, but just mention that it could be computed in order to prevent the subsequent computation of u from oscillating around the optimal trajectory or diverging from it, but ensuring that the convergence is fast enough.

Note that the algorithm defined in Equation (3.6) requires two major computations:

(i) that of the gradient of the objective function, and

(i) the projection to $\mathcal{U}$.

Gradient of the Objective Function

By using the definition of J in Equation (3.4), it can be easily verified that

$$\nabla J(x) = \sum_k \frac{2\beta^2(V_k(x) - V^{nom})}{(\beta^2 - (V_k(x) - V^{nom})^2)^2} \nabla V_k(x) + \sum_\ell \frac{2(I_\ell^{max})^2((I_\ell^{max})^2 - I_\ell(u)^2)}{\left((I_\ell^{max})^2 - I_\ell(u)^2\right)^2} \nabla I_\ell(x). \tag{3.7}$$

This requires the knowledge of $V_k(x)$ and $I_\ell(x)$ and, in particular, its dependence on the power flow $x = (P_1', Q_1', ..., P_n', Q_n')$. The precise dependence is complicated, as it follows from the solution of the power flow equations. We use, instead, a *linear approximation* of this dependence. In particular, given the current state $\hat{V} = \{\hat{V}_k\}$ and $\hat{I} = \{\hat{I}_\ell\}$ (obtained from the state estimation procedure), we let

$$\widetilde{V}(x) = \hat{V} + K_V(x - \hat{x}), \text{ and } \widetilde{I}(x) = \hat{I} + K_I(x - \hat{x}), \tag{3.8}$$

where K_V and K_I are the voltage and current *sensitivity coefficients* computed using methods as in [88, 89]. This simplification is safe as we use small steps to update the

power set-points. By using this approximation, we have that

$$\nabla \widetilde{V}_k(x) = (K_V)_k \text{ and } \nabla \widetilde{I}_\ell(x) = (K_I)_\ell. \tag{3.9}$$

Moreover, as the gradient $\nabla J(x)$ is computed at $x = \hat{x}$, we have that

$$\widetilde{V}(x) = \hat{V} \text{ and } \widetilde{I}(x) = \hat{I}. \tag{3.10}$$

Therefore, Equation (3.7) and the approximated values above provide us with an approximation of the gradient of the objective function.

A similar approach is taken in order to compute the gradient of $J_0(u_0, X_0(x))$, where $X_0(x) = (P_0(x), Q_0(x))$: the exact dependence of $X_0(x)$ is replaced by an approximated linear one, and the corresponding gradient is computed.

It is important to note that at distribution level, the common assumption that the voltage at the LV-MV bus is fixed (infinite bus) is no longer true. Hence, we assume that the GA knows the equivalent Thevenin impedance between this bus and the ideal slack bus of the overall system. This impedance can be computed using methodologies such as [90, 91, 92].

Finally, the gradient of the cost function $C(x)$ is computed either by using the analytic form of the cost function advertised to GA, or by numerical approximation.

Projection onto the Admissible Set

We next give explicit expressions for the admissible set used in the grid agent. We denote with $\bar{\mathcal{A}}$ the *joint* PQ profile, i.e. set of all collections of set-points that are in the advertised PQ profiles, i.e.

$$\bar{\mathcal{A}} \triangleq \Pi_{i=1}^{n} \mathcal{A}_i. \tag{3.11}$$

Similarly, we denote with $\bar{\mathcal{B}}$ the *joint* belief function, by

$$\bar{\mathcal{B}}(u) \triangleq \Pi_{i=1}^{n} \mathcal{B}_i(P_i, Q_i). \tag{3.12}$$

Note that $\bar{\mathcal{A}}$ represents the *domain of definition* of $\bar{\mathcal{B}}$.

Hence, the admissible set can be written as

$$\mathcal{U} = \left\{ u \in \bar{\mathcal{A}} : \forall x \in \bar{\mathcal{B}}(u), J(x) < \infty \right\}, \tag{3.13}$$

where again $x = (P_1', Q_1', ..., P_n', Q_n')$ is any *actual* implementation of the power flows. Observe that the feasibility condition of Equation (3.1) is equivalent to $J(x) < \infty$ (see Equation (3.4)).

We next relax the exact computation of the projection to the set of admissible target set-points $\mathcal{U}$, which is required in the solution of Equation (3.6). Note that belief functions are used to ensure a feasible operation of the grid, hence we need to guarantee that the relaxation maintains the feasibility property.

First, consider the subproblem of testing whether a given control $u \in \mathcal{U}$. We refer to this process as the *admissibility test*. As follows from Equation (3.13), in order to carry out this test, we should solve

$$\max_{x \in \tilde{\mathcal{B}}(u)} J(x) \tag{3.14}$$

and verify whether the result is finite.

The above optimization is hard in general, as it should test all the combinations of power set-points and their corresponding beliefs that in principle could be non-convex. Instead, we propose to relax it as follows. First, observe that using Definition 3.2.1, we can replace the exact belief functions with *supersets*. We thus assume that the grid agent has access to functions $\tilde{\mathcal{B}}_i(P_i, Q_i)$ with the following two properties:

(i) $\mathcal{B}_i(P_i, Q_i) \subseteq \tilde{\mathcal{B}}_i(P_i, Q_i)$, and

(ii) $\tilde{\mathcal{B}}_i(P_i, Q_i)$ is a *rectangle* in $\mathbb{R}^2$.

We note that the rectangular *super beliefs* can be either sent directly by the follower agents, or computed by the grid agent from the advertised exact beliefs.

One possible solution for performing the projection into the admissible set $\mathcal{U}$ is shown in Algorithm 1, and the admissibility test can be performed as presented in Algorithm 2.

We also use the following property. It was shown in [87] that, whenever the shunt elements of the lines are neglected, the solution is *monotonic* in radial distribution networks. Specifically, every voltage magnitude can either increase or decrease monotonically as a function of a single power-injection (while the other injections are kept fixed). Similarly, the extreme values of the current magnitudes are obtained at the extreme values of a power injection.

For the case of medium-voltage lines in which shunt capacitances cannot be neglected (specially in the case of coaxial cables), we can numerically verify that this condition holds in general. For example, taking the most difficult case of a capacitive constant power factor load, we show in Figure 3.8 that monotonicity holds in practice, and that the non-monotonicity behavior appears either in the non-admissible operation zone of the line, or for very long lines (not expected at distribution level). This property enables a considerable reduction of the computational complexity, when running the admissibility

Algorithm 1 Projection onto $\mathcal{U}$

Input: Control $u = (u_j)$ to be projected.
Parameters: Search step Δu, number of search directions n.
Initialization: The min-max violation $\Delta_{\min\max} = C > 0$.
While: $\Delta_{\min\max} > 0$

1. Generate n test point $\{x_m, m = 1, ..., n\}$ uniformly spread on a sphere with radius Δu around u, so that $\|x_m - u\| = \Delta u$.
2. **For** $m = 1, ..., n$**:**
   (a) Project x_m to $\mathcal{A}$ (using, e.g., the alternating projections method [93]):
   $$x_m := \mathcal{P}_{\mathcal{A}}\{x_m\}.$$
   (b) Use Algorithm 2 to test admissibility of x_m, save the output to $\Delta_{m,\max}$.
3. Compute the direction of the minimum violation:
   $$m^* \in \underset{m=1,...,n}{\operatorname{argmin}} \Delta_{m,\max},$$
   and the corresponding violation:
   $$\Delta_{\min\max} = \min_{m=1,...,n} \Delta_{m,\max}.$$
4. Update $u := x_{m^*}$.

Output: The projected control u.

Algorithm 2 Admissibility Test

Input: Control $u = (u_j)$ to be tested.
Parameters: Belief functions of the resources, given in terms of $\mathcal{B}_j(u_j)$ – finite sets of representative "worst-case" set-points that u can give rise to (e.g., vertices of a rectangle).
Do: Obtain worst-case set-points of a resource j by using the belief function,
$$B_j = \mathcal{B}_j(u_j),$$
and test all possible combinations of the set-points in B_j. That is, for each $x_j \in B_j$, compute $d(x, \mathcal{Y})$, where $d(y, \mathcal{Y})$ is a certain "distance" of x from the set $\mathcal{Y} \triangleq \{x : J(x) < \infty\}$. This distance can be computed using the definition of J.
Output: Maximum violation $\Delta_{\max} = \max_{x:\, x_j \in B_j} d(x, \mathcal{Y})$.

test. We emphasize, however, that in the general framework, the monotonicity is not a necessary condition, as long as the admissibility can be verified efficiently.

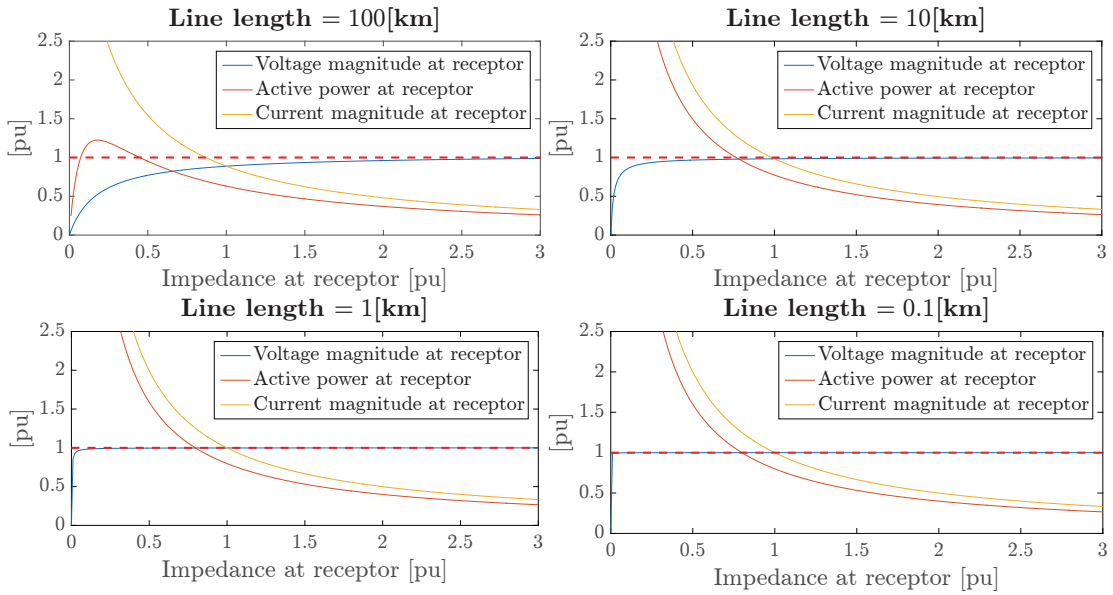

Figure 3.8 – Monotonicity analysis for a 20[kV], 5[MVA] power cable at distribution level. $r = 0.0095[\frac{m\Omega}{m}]$, $l = 0.309[\frac{\mu H}{m}]$, $g = 0.285[\frac{nS}{m}]$, $c = 0.302[\frac{nF}{m}]$. Load has a capacitive power factor of 0.8.

By using the definition of $J(u)$ in Equation (3.4), it follows that only a small finite number of simple computations is required in order to perform the admissibility test of a control u. In particular, for each *vertex* v of $\tilde{\mathcal{B}}(u)$, we should test whether (i) there exists a solution to the load-flow equations, and whether (ii) $J(x) < \infty$.

Given this simplified admissibility test, we can devise an efficient method for projection to $\mathcal{U}$. As the projection is needed only in a local vicinity of the current set-point $\hat{x}$, it can be efficiently computed by doing a search of the closest point in $\mathcal{U}$, and using a relatively small number of the (simplified) admissibility tests.

3.3 Adaption to Islanded Microgrids

We have presented in Section 3.2 the method for steering a microgrid connected to an upper level grid, relying on the assumption that this grid will act as slack. However, when a microgrid is working in islanded mode, the flexibility for reacting to a power change in the grid is only given by local resources.

We assume that one of the resources of the microgrid is able to work in voltage-control mode, and that its agent constantly sends the aforementioned information to the GA.

With this, we show that few modifications are to be done to the framework.

3.3.1 Impact on the GA Objective Function

We repeat here that the three purposes of the GA are to minimize the cost functions of the RAs, to keep the system in safe electrical state and to try to comply with the received request, remain unchanged. Yet, the slack resource in this case has a dynamic flexibility that can be represented in terms of its advertisement. Let us designate, without loss of generality, this agent as RA_0. It is worth observing that, as defined by the proposed control framework, this agent sends the advertisement $(\mathcal{A}_0, \mathcal{B}_0, \mathcal{C}_0)$ to the GA; however, instead of implementing set-points, as it works in the voltage control mode, it satisfies any instantaneous (P, Q) request within its capability limits.

In this sense, no request is implemented in the slack resource, but the GA tries to satisfy as much as possible the operation preference of RA_0. Therefore, we use the advertised cost of the slack agent $\mathcal{C}_0$ as a cost for power at the slack bus, namely

$$J_0(u_0, X_0(u)) = w_0 \mathcal{C}_0(P_0, Q_0), \tag{3.15}$$

where w_0 is the weight assigned to the cost of RA_0.

3.3.2 Impact on the Admissible Set

For the islanded mode, a set-point is considered admissible if, apart from resulting in a feasible electrical state, it also results in a feasible power flow for the slack resource. This is,

$$\mathcal{U} = \left\{ u \in \bar{\mathcal{A}} : \forall x \in \bar{\mathcal{B}}(u), J(x) < \infty, X_0(x) \in \mathcal{A}_0 \right\}, \tag{3.16}$$

where x is the actually implemented overall power set-point, $J(x)$ is the grid operation cost, $X_0(x)$ is slack power flow when x is the power set-point, and $\mathcal{A}_0$ is the slack resource PQ profile.

With these two modifications, we ensure that the GA is able to exploit the flexibility of the microgrid under its control, whereas the operational limits of the slack resource are always respected. Note that the autonomous operation of the microgrid strongly depends on the flexibility, of the slack resource, to react to uncertain power variations. Imagine, for the sake of simplicity, that the microgrid is equipped with two similar storage systems. By default one of them is chosen to be the slack. Assume that, after some time of operation, the slack storage is close to reach its capacity limits, considerably reducing its flexibility and the second one stays in normal conditions. In such an scenario, it would be desirable that the second storage become slack. We discuss in Section 3.5.4 a method for real-time selection of the slack resource.

Observe that, in the COMMELEC framework, the system frequency is not needed as a variable of interest for controlling the microgrid, because there is no control action performed by using this magnitude. Therefore, during an islanded operation, it can be kept constant at the grid rated value (e.g., 50[Hz]). This can be physically actuated by an astatic controller in RA_0. Further use of the frequency signal can be used for improving the system behavior, but it is not discussed here.

3.4 Composability and Aggregation

A key aspect of the framework is *composability*: resources and subsystems can be aggregated and viewed by others as a single entity that exhibits the same properties of a single element (i.e., PQ profile, belief function, and virtual cost). This is essential for the application of the framework to systems of any size and complexity. In particular, our goal is to propose a *computationally efficient* method that ensures *feasibility of the electrical state* of the entire system, specifically, of all layers.

Consider again, without loss of generality, the setup of Figure 3.1. Recall that we use the index 0 for referring to the LV-MV bus.

3.4.1 Aggregated PQ Profile $A\mathcal{A}$

First, we write the load-flow constraints more explicitly, in terms of the power injections in the grid and the powers at the slack bus:

$$P_0 = \sum_{i=1}^{n} P_i - L_P(\{P_i, Q_i\}), \quad Q_0 = \sum_{i=1}^{n} Q_i - L_Q(\{P_i, Q_i\}), \tag{3.17}$$

where $L_P(\{P_i, Q_i\}) \geq 0$ and $L_Q(\{P_i, Q_i\})$ is the active and reactive total power "losses". Alternatively, Equation (3.17) can be written as

$$X_0(u) = \sum_i u_i - L(u), \quad L(u) \triangleq (L_P(\{P_i, Q_i\}), L_Q(\{P_i, Q_i\})), \tag{3.18}$$

and the exact aggregated PQ profile reads

$$A\mathcal{A} = \bigcup_{u \in \mathcal{U}} \left\{ u_0 = \sum_{i=1}^{n} u_i - L(u) \right\}. \tag{3.19}$$

where $u_i \in \mathcal{A}_i$.

To make the computation simple and compatible with our real-time application, we choose to aggregate the PQ profile by ignoring the losses in the load-flow problem. Specifically,

we assume that the LV-MV power flow takes the form of

$$u_0 = \sum_{i=1}^{n} u_i, \tag{3.20}$$

Hence, the aggregated PQ profile is given by

$$A\mathcal{A} = \sum_{i=1}^{n} \mathcal{A}_i, \tag{3.21}$$

where the summation is the Minkowski set summation. We note that the Minkowski summation can be computed efficiently when the sets $\mathcal{A}_i$ are approximated by convex polygons.

3.4.2 Aggregated Belief Function $A\mathcal{B}$

The main challenge in defining the aggregated belief function is to define a set that (i) is large enough to cover the uncertainty in the operation of GA in between two set-points request, and (ii) is small enough to provide as accurate view of uncertainty as possible to the upper GA.

We want to expose the uncertainty of the LV-MV power flow that is caused by request u_0. However, we assume that the aggregated belief function does not depend on the request u_0, and we identify the corresponding constant function with the uncertainty set. This assumption is reasonable whenever the upper GA works at a much slower pace. Therefore, the computation of the aggregated belief function will depend solely on the last set of set-points, namely u, by solving the following four optimal power flow problems (OPFs):

$$\begin{aligned} &\max / \min P_0 && \max / \min Q_0 \\ &\text{s.t.} \begin{cases} x \in \mathcal{B}(u), \\ (P_0, Q_0) = X_0(x), \end{cases} && \text{s.t.} \begin{cases} x \in \mathcal{B}(u), \\ (P_0, Q_0) = X_0(x). \end{cases} \end{aligned} \tag{3.22}$$

This will yield a *rectangular* belief function that represents a superset of the true aggregated belief. Let us define

$$A\mathcal{B} = R(u) = [\underline{P}, \overline{P}] \times [\underline{Q}, \overline{Q}], \tag{3.23}$$

where $\underline{P}, \overline{P}, \underline{Q}, \overline{Q}$ are the solutions of Equations (3.22).

In order to cope with our real-time application, we propose to avoid solving these exact OPFs; instead we use Equations (3.17) and *bounds on the losses*. As a preliminary step,

these bounds are estimated *offline*:

$$\begin{aligned} \overline{L}_P &= \max L_P(\{P_i, Q_i\}), \quad \underline{L}_P = \min L_P(\{P_i, Q_i\}), \\ \overline{L}_Q &= \max L_Q(\{P_i, Q_i\}), \quad \underline{L}_Q = \min L_Q(\{P_i, Q_i\}), \end{aligned} \tag{3.24}$$

where the optimization is done over all possible set-points.

3.4.3 Aggregated Cost Function $A\mathcal{C}$

As mentioned in 3.2.4, to compute the aggregated virtual cost function at a given requested set-point $u_0 = (P_0, Q_0)$, the internal GA applies its gradient descent algorithm in Equation (3.6) in order to obtain a collection of power set-points u for its set of followers, and it returns the corresponding value of the objective function in Equation (3.5). In principle, as with $A\mathcal{B}$, we should compute $A\mathcal{C}(u_0)$, which could be obtained by evaluating the objective function

$$F(u_0) = C(u_0) + J_0(u_0) + J(u_0), \tag{3.25}$$

in a sparse partition of $u_0 \in A\mathcal{A}$, and performing a suitable interpolation method.

Instead, under the assumption of slow change of the request u_0 and due to frequent set-point updates, we propose to advertise a *linear approximation* of the cost function in the form

$$A\mathcal{C}(u_0) = \lambda P_0 + \mu Q_0, \tag{3.26}$$

where

$$\lambda \triangleq \partial F/\partial P_0, \quad \mu \triangleq \partial F/\partial Q_0 \tag{3.27}$$

are the partial derivatives of the objective function computed at the current set-point u.

Note that u depends on P_0 and Q_0 through Equation (3.6). As this dependence involves projection, we propose assuming that the projection is not active, namely

$$\begin{aligned} u &= \hat{x} - \alpha \nabla F(\hat{x}) \\ &= \hat{x} - \alpha \left(\sum_i w_i \nabla C_i(\hat{x}) + \nabla J(\hat{x}) + \nabla J_0(\hat{x}, P_0, Q_0) \right). \end{aligned} \tag{3.28}$$

3.4.4 Using the Composability in the GA Decision Process

The aggregation method naturally accounts for an asynchronous message exchange, and it is inherently robust to communication delays. Indeed, if the GA sends at a given

time-step an advertisement containing $A\mathcal{B}$, it can perform the set-points computation of Equation (3.6) considering that the admissible set $\mathcal{U}$ is

$$\mathcal{U} = \left\{ u \in \bar{\mathcal{A}} : \forall x \in \bar{\mathcal{B}}(u), J(x) < \infty, X_0 \in A\mathcal{B} \right\}, \tag{3.29}$$

until the reception of a new request. In words, the GA will use, in the set-points computation, the last computed advertisement as a *promise* of what the uncertainty of LV-MV power flow will be. In this sense, several set-point computations could be performed with the same $A\mathcal{B}$ that would be updated only after receiving a new request or, for instance, whenever the set $\mathcal{U}$ is empty as it is not possible to satisfy the constraint $\forall x \in \mathcal{B}(u), X_0(x) \in A\mathcal{B}$.

In fact, this could also happen upon receiving a new set of advertisements, as using $R(u)$ from Equation (3.22) can be a too restricted set, in view of the admissibility set $\mathcal{U}$ defined in Equation (3.29). To overcome this problem, we propose to inflate the belief set as follows. Consider a ball $B(u, \rho)$ of set-points with radius ρ centered on u. Sample K set-points $u^{(k)} \in B(u, \rho)$, $k = 1, ..., K$, so that $u^{(k')} = u_j$ for some k'. Then advertise

$$A\mathcal{B} = \text{rect} \left[\bigcup_{k=1}^{K} R\left(u^{(k)}\right) \right], \tag{3.30}$$

where rect $(\cdot)$ is the "rectangular hull", i.e., the corresponding bounding box approximation. Clearly, this set contains the uncertainty caused by the currently implemented set-point u, as well as that of implementing other set-points that are at the distance at most ρ from u. Recall that, by using the property of Definition (3.2.1), this superset ensures that the computed set-points will be admissible.

3.5 Islanding Maneuver

In this section, we propose a procedure to cope with an unintentional islanding using the available information defined by the COMMELEC framework. We define the method as follows.

(a) At all times, in particular before the islanding event occurs, the GA maintains two lists:

- A rating list $\mathcal{I}$, of all the RAs controlled by the same GA in view of their ability to be a slack resource. This rating is computed based on the power availability and on the state-of-energy (SoE) of each resource. The SoE quantifies the amount of energy that can be withdrawn from a potential slack regardless of the PQ profile for a given time-window.
- A list of all the resources $\mathcal{S}$ (i.e., generators and loads) that have to be shed if the current best candidate slack resource (the first in the previous rating) is

selected. This list can be computed from the uncertainty of the resources and from a predefined order of shedding priority. We assume the latter is given.

(b) Islanding conditions are continuously monitored via an available real-time state estimation process. When these conditions are detected, the GA sheds all resources in the shedding list and chooses an initial slack based on the current rating.

(c) The grid operation continues during the remainder of the islanding maneuver under the control of the GA, as explained in Section 3.3. During this operation, two events can occur:

- The rating of the resources has changed, so that a new resource is at the top of the ranking.
- It is not possible to operate the grid with the current slack (without rating change). In this case, a further load shedding is performed.

Definition 3.5.1. *A microgrid is islanding-capable when there exists at least one resource that is able to absorb the power imbalance with a guaranteed quality-of-supply, for any actual implementation that is compatible with the advertised belief functions.*

By using the proposed procedure, a microgrid is always islanding-capable minimizing the amount of resources disconnections.

We consider that the steps to perform an islanding maneuver are

1. **Detection of islanding conditions.** Several methods could be used. We assume to have one device that signals the islanding conditions in less than 20[ms]. This is possible to perform in real-time, in principle, due to the availability of a system observability infrastructure (see Section 3.1).
2. **Adaptive slack selection.** The advertisement messages from the RAs are used to choose the "best" possible slack in real-time in an adaptive way.
3. **Quality-of-Supply and Optimality.** Right after the islanding, the GA will steer the electrical state as explained in Section 3.3. In particular, the quality-of-supply in the network is optimized.

Next, we explain the way to perform the second and third step in the COMMELEC framework.

3.5.1 Criteria for Ranking the Slack Candidates

In this section, we show how the information exchanged between the agents in the COMMELEC framework can be used to assist in choosing the most appropriate slack

resource. We assume that the GA maintains a rating of all the resources based on (i) the state of energy (SoE) of each resource (in Wh) and (ii) the advertisements from the resource agents. In particular, a separate "task" is running in the grid agent that is responsible for preparing the list of candidate slack resources. We note that (i) should be sent by the resource agents to the GA, which can be done straightforwardly by adding a message type to the COMMELEC framework.

Also, observe that the knowledge of (i) only, is not enough to choose the best appropriate slack. Consider, for example, the case when the grid is *consuming* 10[kW] and there are two possible slack resources, a battery with SoE=30[kWh] and a supercapacitor with SoE= 2[kWh]. Without knowing the real-time constraints of these two resources, the natural choice according to the SoE would be the battery. However, if we know (from the advertised PQ profile) that the battery can supply only 5[kW] and that the supercapacitor can supply 60[kW], we will choose the supercapacitor as the default slack resource (with the possibility to switch later to the battery).

Below we propose a concrete way for preparing this rating. For each candidate slack resource i, and any element (either vector or set) $\mathcal{E}$, we let $\mathcal{E}_{-i}$ denote the same element *without* considering the resource i. In particular,

$$\mathcal{A}_{-i} = \mathcal{A}_1 \times ... \times \mathcal{A}_{i-1} \times \mathcal{A}_{i+1} ... \times \mathcal{A}_n \tag{3.31}$$

denotes the overall PQ profile, omitting $\mathcal{A}_i$, and the same for $\mathcal{B}_{-i}$, u_{-i}, and x_{-i}.

When considering resource i as a slack, we let $Y(x_{-i}|i)$ denote the corresponding electrical state of the grid. Specifically, it is the load-flow solution when i is the slack and the power set-point for other resources is x_{-i}. Similarly, $X_i(x_{-i})$ is the resulting power at the slack bus. We denote the set of feasible states when i is the slack by $\mathcal{F}_i$.

We next define the following metrics that are used to rate the candidates for being a slack resource.

Controllability of the Resource

We would like to choose resources with no (or little) uncertainty in the implementation of the requested set-point. Hence, ideally, we would like to choose a resource with a "perfect" belief function, namely $\mathcal{B}_i(P,Q) = \{(P,Q)\}$. Then, the first metric $\rho_C(i)$ measures the distance between the perfect belief $\{P,Q\}$ and the advertised one. Formally, we set

$$\rho_C(i) \triangleq \max_{(P,Q)\in\mathcal{A}_i} \max_{(P',Q')\in\mathcal{B}_i(P,Q)} \frac{d((P,Q),(P',Q'))}{\sqrt{P^2+Q^2}}, \tag{3.32}$$

where, $d((P,Q),(P',Q'))$ is the distance imposed by the Euclidean norm. It can be seen that ρ_C is the maximal set-to-set (Hausdorff) distance between the singleton $\{P,Q\}$ and

$\mathcal{B}_i(P,Q)$ over all possible $(P,Q) \in \mathcal{A}_i$, measured in percentage relative to the requested set-point (P,Q). We note that this normalization is essential in order to compare the controllability of resources with different power ratings.

Available Power-Range

The following metrics measure the ability of resource i to absorb the imbalance in the grid created by the current (measured) set-point $\hat{x}_{-i}$, taking into account the uncertainties as represented by the advertised belief functions. In particular, let

$$A\mathcal{B}_i(u_{-i}) \triangleq \{(P_i,Q_i) = X_i(x_{-i}) : x_{-i} \in \mathcal{B}_{-i}(u_{-i})\} \tag{3.33}$$

denote the set of all possible power set-points that could take place at the connection point of resource i, given the uncertainty of all other resources defined by $\mathcal{B}_{-i}(u_{-i})$ or, in other words, the *aggregated* belief set for the slack power, computed at a given set-point u_{-i}.

We define the metric $\rho_{P,1}(i)$ to measure the safety margins of resource i as follows:

$$\rho_{P,1} \triangleq \min_{(P_i,Q_i)\in A\mathcal{B}_i(\hat{x}_{-i})} d\left((P_i,Q_i),\mathcal{A}_i^c\right). \tag{3.34}$$

Here, $\mathcal{A}_i^c$ is the complement of $\mathcal{A}_i$ relative to $\mathbb{R}^2$, and $d(x,S)$ denotes the Euclidean distance of x from the set S. Observe that, on the one hand, a positive $\rho_{P,1}$ means that the current set-point is "safe" in the sense that for any actual implementation, the resulting slack power is feasible. On the other hand, we define $\rho_{P,2}$ as the amount of maximum violation of resource i:

$$\rho_{P,2} \triangleq \max_{(P_i,Q_i)\in A\mathcal{B}_i(\hat{x}_{-i})} d\left((P_i,Q_i),\mathcal{A}_i\right). \tag{3.35}$$

Note that $\rho_{P,2}$ is positive when the current set-point results in a non-feasible actual implementation.

Feasibility of the Electrical State

We next define metrics that measure the ability of resource i to provide a feasible electrical state when it is the slack, taking into account the uncertainties represented by the advertised belief functions. Similarly to $A\mathcal{B}_i$, we let

$$\mathcal{Y}_i(u_{-i}) \triangleq \{y = Y(x_{-i}|i) : x_{-i} \in \mathcal{B}_{-i}(u_{-i})\} \tag{3.36}$$

denote the set of all possible electrical states that could result from the uncertainty of all resources but i when i is the slack. We then compute the following two distances:

$$\rho_{Y,1} = \min_{y \in \mathcal{Y}_i(\hat{x}_{-i})} d\left(y, \mathcal{F}_i^c\right), \quad \rho_{Y,2} = \max_{y \in \mathcal{Y}_i(\hat{x}_{-i})} d\left(y, \mathcal{F}_i\right), \tag{3.37}$$

with a similar interpretation to that of $\rho_{P,1}$ and $\rho_{P,2}$.

Admissibility of Set-Points

We consider the set $\mathcal{U}_i$ of *admissible* set-points when resource i is the slack, that is the collection of target set-points for all resources but the slack, $u_{-i} \in \mathcal{A}_{-i}$, so that (i) the resulting electrical state is feasible, and (ii) the resulting power at the slack bus fits the PQ profile $\mathcal{A}_i$ of the slack, for any actual implementation that is compatible with the belief functions. Formally, $\mathcal{U}_i$ can be written as

$$\mathcal{U}_i = \left\{u_{-i} \in \mathcal{A}_{-i} : \mathcal{Y}_i(u_{-i}) \subseteq \mathcal{F}_i,\ A\mathcal{B}_i(u_{-i}) \subseteq \mathcal{A}_i\right\}. \tag{3.38}$$

Observe that when $\mathcal{U}_i = \emptyset$, it is not possible to operate the grid with the current slack unless a shedding strategy is applied. We thus define a binary metric

$$\rho_U(i) \triangleq \mathbb{I}\left\{\mathcal{U}_i = \emptyset\right\}, \tag{3.39}$$

where $\mathbb{I}\left\{\cdot\right\}$ is the indicator function. We note that the exact computation of this metric is not feasible in the real-time framework as $\mathcal{U}_i$ is not given explicitly as in Equation (3.13) or Equation (3.16). However, a sufficient condition for $\mathcal{U}_i \neq \emptyset$ is that the GA is able to *project* the current set-point to $\mathcal{U}_i$. In the following, we thus identify the condition $\mathcal{U}_i \neq \emptyset$ with the ability to project to $\mathcal{U}_i$.

State of Energy (SoE)

Observe that the interpretation of the SoE depends on whether the grid produces or consumes power. Specifically, given the current set-point, let $(\hat{P}_i, \hat{Q}_i)$ denote the active and reactive power flows at the slack bus, assuming that the grid is islanded and i is set to be the slack. We consider a *directional* metric, defined by

$$\rho_E(i) = \begin{cases} (1 - \mathrm{SoE}_i) E_{\mathrm{rated},i}, & \text{if } \hat{P}_i < 0, \\ \mathrm{SoE}_i E_{\mathrm{rated},i}, & \text{otherwise,} \end{cases} \tag{3.40}$$

where SoE_i is the state of energy of the resource i (in *per unit* of the rated power of a given resource), and $E_{\mathrm{rated},i}$ is its rated energy capacity. We note that this metric cannot directly be computed from the information advertised in the original COMMELEC framework, but it can readily be obtained by a simple addition to the advertisement

messages.

Using $\rho_E(i)$, we also estimate the "survival time" of a slack resource as follows:

$$\rho_T(i) = \rho_E(i)/\hat{S}_i, \tag{3.41}$$

where $\tilde{S}_i = \sqrt{\hat{P}_i^2 + \hat{Q}_i^2}$ denotes the corresponding apparent power.

Rating Computation

First, the GA filters out the non-controllable resources and the resources that have too short a survival time, by considering only the set

$$\mathcal{I} = \{i : \rho_C(i) \leq \epsilon, \rho_T(i) \geq \delta\}, \tag{3.42}$$

for some $\epsilon \geq 0$ and $\delta > 0$. The value of ϵ represents the maximum allowed deviation of the actually implemented set-point from the requested one (in percentage from the requested one). The value of δ is chosen large enough so that the slack can absorb the imbalance during several COMMELEC cycles. Then, we sort *lexicographically* the resources according to

- ρ_U, so that resources with $\rho_U(i) = 0$ (i.e., having non-empty set of admissible set-points) are on top;
- $\rho_{P,2}$ in ascending order, so that resources with the least violation of power feasibility are on top;
- $\rho_{Y,2}$ in ascending order, so that resources with the least violation of state feasibility are on top;
- $\rho_{P,1}$ in descending order, so that resources with the maximum power-availability are on top;
- $\rho_{Y,1}$ in descending order, so that resources with the maximum state-feasibility margins are on top;
- ρ_E in descending order, so that the resources with the highest SoE are on top.

To decide if two resources i, j have the *same* metric ρ, we use an *approximate* equality test, namely $|\rho(i) - \rho(j)| \leq \alpha$ for some small $\alpha \geq 0$. Let $\mathcal{I}(1)$ denote the *best-rated* resource.

3.5.2 Counteraction in the Case of Non-admissibility: Shedding List

Note that, in the case of an unintended islanding, the power flows in the grid can dramatically change. That being said, the previous slack ranking could result in all

elements with $\rho_U(i) = 1$, in other words, no device in the microgrid (in particular $\mathcal{I}(1)$) would be able to handle this sudden change while keeping the system in a safe electrical state. Formally, the microgrid is not *islanded-capable* as per Definition (3.5.1). This conduces to the need of disconnecting elements in the grid, as regularly done in power networks. Yet, by using the available information given by the COMMELEC framework, the GA could take wiser decisions and also rank the elements to disconnect. We call this ranking the *Shedding list* $\mathcal{S}$.

First, we assume that the GA has access to a *priority-ordered list* of devices to shed, which is the usual information available for a central operator to perform load/generation shedding schemes. For example, hospitals or security facilities will be at the end of this list. Note that this list could also use information advertised in the COMMELEC framework, such as the controllability of the resource (given by metric $\rho_C(i)$) and/or other.

We define now the shedding list $\mathcal{S}$, which is the result of checking the admissibility of the best slack candidate *in case the islanding takes place*. Formally, in the simulated scenario when the islanding takes place with $\mathcal{I}(1)$ as slack and if shedding is necessary, i.e., if $\rho_U(\mathcal{I}(1)) = 1$, we follow the next procedure:

(a) The first element of the priority-ordered list is added to $\mathcal{S}$.

(b) We recompute $\rho_U(\mathcal{I}(1))$, i.e., the set-point-admissibility metric of the selected slack $\mathcal{I}(1)$, with this new state of the shedding list.

(c) If $\rho_U(\mathcal{I}(1)) = 0$, we stop, otherwise we add to $\mathcal{S}$ the next element of the priority-ordered list and go back to the previous step.

This is repeated until $\rho_U(\mathcal{I}(1)) = 0$ or the priority-ordered list is exhausted. Note that until this point, no actions have been performed, but we are only preparing the GA to know how to react in case of an islanding maneuver. We next explain how to proceed in such an scenario.

Observe that, even when this procedure is conceived for the case of the islanding maneuver, during regular islanded operation the GA can end up in a situation where $\mathcal{U}$ is empty. In such a case, we can use the same procedure.

3.5.3 Islanding Maneuver

When the unintentional islanding occurs, there is a need to immediately react to the islanding condition by steering the power set-points to an admissible area. Hence, we propose a simple and time-efficient scheme rather than an optimal one.

Recall that, as the first step, the islanding conditions are detected using real-time state estimation. As a result of this detection, the elements of $\mathcal{S}$ are shed and the resource $\mathcal{I}(1)$ is set to be the slack.

The same procedure can be used for an *intentional* islanding maneuver as well. However, in this latter case there is inherently more time to prepare the system to the islanded mode, therefore more elaborate algorithms can be used.

3.5.4 Dynamic Slack-Selection

Note that the procedure of Section 3.5.2 is not only useful for the islanding maneuver, but it could also be helpful on the islanded operation.

Indeed, if we assume that the GA has the ability of computing the aforementioned metrics during the islanded operation, we could make use of the counteraction of Section 3.5.2 continuously. The main difference in this case, is that in islanded mode this is not anymore a simulation, but a real condition, i.e., $\mathcal{I}(1)$ is the slack and the GA steers the system as in Section 3.3. In that sense, the computation of the shedding list is done assuming that $\mathcal{U}(\mathcal{I}(1)) = \emptyset$, again, preparing the GA for that scenario.

Observe that the slack ranking can change during the islanded operation of the microgrid as, for instance, in the case discussed in Section 3.3.2. With this procedure, the change to another, more suitable, slack resource is straightforward.

3.5.5 Re-connection of Shed Resources

Once in islanded mode, some resources can remain disconnected, due to the action of the shedding list. Note that all disconnected resources are contained in $\mathcal{S}$. In this case, we assume that elements that are at the beginning of the list have more priority (as they were the last to be added). Then, we propose to re-connect the elements one-by-one with the following procedure:

(a) As with the construction of $\mathcal{S}$, we simulate the case when $\mathcal{S}(1)$ is connected and check that $\rho_U(\mathcal{I}(1))$. That is to say, the uncertainty of the new resource can be handled by the slack and it results in a feasible electrical state.

(b) If $\rho_U(\mathcal{I}(1)) = 1$ we return to the previous step, otherwise we continue.

(c) The element is requested to be connected to the grid and is removed from $\mathcal{S}$.

(d) The process is repeated from the beginning. It ends only when the list is exhausted.

3.6 Re-synchronization Process

Recall that in islanded mode, we assume that the slack resource can be connected to any node of the microgrid. Considering that we are provided with a real-time state estimation process, we assume that there is access to the voltage phasors measurements at both sides of the connection breaker between the microgrid and the upper grid.

Let us call the *sync-magnitudes* of bus k the triplet $s_k = \{V_k, \delta_k, f_k\}$. Ideally, for the re-synchronization process to succeed we would like to fulfill the condition

$$s_0 = s_0^{out}, \tag{3.43}$$

where s_0 and s_0^{out} are the measured sync-magnitudes in the connection point at the microgrid side and the upper-grid side, respectively.

As the frequency is not used as a control variable by COMMELEC (see Section 3.3) and assuming that it is a global magnitude (i.e., a single frequency characterizes the entire microgrid), we can easily control it at the slack resource. We name f the overall frequency of the microgrid. With this, we can then set the angle-reference at $\delta_i = 0$, so that the phasors measured at the external grid will be referred to the microgrid slack. This can be safely done and has a negligible effect on the resulting power flows. Frequency can be then adapted at the slack resource so that the conditions $f = f_0^{out}$ and $\delta_0 = \delta_0^{out}$ are met. For this, we propose to send $\Delta f = f - f_0$ and $\Delta\delta = \delta_i - \delta_0$ to the slack resource . Specifically, we propose the following procedure

(a) At first retrieval, set $f = \hat{f} + \Delta f$ and disregard $\Delta\delta$. This will give us an idea about how much the angle has to be corrected.

(b) From hereon, and considering that the deviation $\Delta\delta$ is similar in all buses, modify the frequency at the slack so that $f = \hat{f} + \Delta f$ and $\delta_0 = \hat{\delta_0} + \Delta\delta$.

(c) Repeat previous step until $\Delta f \leq \epsilon_f$ and $\Delta\delta \leq \epsilon_\delta$, with $\epsilon_f, \epsilon_\delta > 0$.

As the normal islanded operation keeps running, power flows will continue changing, thus affecting the voltage phasors in the microgrid, specifically the sync-magnitude s_0. This will affect both V_0 and δ_0, but not f. Therefore, we could modify the penalty function of the GA to, for example,

$$J(u)' = J(u) + \frac{(V_0(u) - V_0^{out})^2}{\beta_0^2 - (V_0(u) - V_0^{out})^2}, + \frac{(\delta_0(u) - \delta_0^{out})^2}{\gamma_0^2 - (\delta_0(u) - \delta_0^{out})^2}, \tag{3.44}$$

where β_0 and γ_0 are small enough to ensure small deviations when the re-synchronization takes place. Observe that in order to apply our method of Equation (3.7) we need the derivatives of the angle with the respect to the set-points $\partial\delta_0/\partial P_\ell$, $\partial\delta_0/\partial Q_\ell$ for all ℓ, which could also be obtained using sensitivity coefficients as in [88].

However, condition (3.43) can be too strict for the current resources flexibility, represented by the PQ profiles $\mathcal{A}_{-i}$, in the microgrid. This calls for the use of another decision variable. We choose the voltage-magnitude at the slack resource V_i, as it is the only one in the microgrid that works on voltage-mode. First, we need to verify that the slack resource can cope with the change in the power flows of the grid, given the change in s_i. This is due to the fact that some resources of the grid could change their power flow, as a function of the local voltage in their node. Assuming that this variation is accounted for in the belief function of each resource (See Section 4.6 for an example), which can be safely done as voltage is a local variable at each node, we just need to verify that

$$A\mathcal{B}_i(u_{-i}) \subseteq \mathcal{A}_i. \tag{3.45}$$

Recall that the computation of $A\mathcal{B}_i$ uses a worst-case scenario analysis for the losses. Second, we need to know what is the best V_i to meet condition (3.43). For this purpose, we consider that

(i) as $\hat{x}_{-i} \in \mathcal{B}_{-i}(u_{-i})$, a good guess for the implemented power flow is the current measurement $x_{-i}(s_i) = \hat{x}_{-i}$ and,

(ii) the selected s_i results in a feasible state, i.e. $Y(s_i|i) \in \mathcal{F}_i$.

Hence, we propose to solve the following OPF

$$\begin{aligned} &\min_{(P_i,Q_i)\in A\mathcal{B}_i(u_{-i})} C_i(X_i(s_i)) \\ &\text{s.t.} \begin{cases} s_0 = s_0^{out} \\ X_i = \sum_{k\neq i} \hat{x}_k - L(s_i, \hat{x}_{-i}) \\ Y(s_i|i) \in \mathcal{F}_i, \end{cases} \end{aligned} \tag{3.46}$$

with C_i the virtual cost function of the slack resource and $\hat{x}_{-i}$ the current power flow implementation in all resources but the slack. The solution of this problem, s_i, will be then sent to the slack resource to be implemented. Note that this procedure could be repeated in several time-steps due to the uncertainty of the resources in the microgrid.

The difficulty of the problem lies on the non-convex nature of $L(s_i, \hat{x}_{-i})$. In order to solve it efficiently, we propose to approximate it with

$$L = \frac{\partial L}{\partial V_i}\Delta V_i + \frac{\partial L}{\partial \delta_i}\Delta\delta_i. \tag{3.47}$$

As the losses are essentially affected by voltages magnitudes, the right-side element of the sum can be neglected. With this, we need to have access only to the partial derivatives $\partial V_{k\neq i}/\partial V_i$ and to the Y impedance matrix.

4 Resource-Agents Design

Chapter Highlights:

In this chapter, we present examples of and give ideas about the general procedure for designing COMMELEC resource agents for the typical devices connected to microgrids.
Depending on their nature and/or internal characteristics, these resources have various degrees of controllability, from *fully controllable* resources (e.g., batteries) to *non-controllable* resources (e.g., uncontrollable loads). We show in this chapter that the controllability of the resource has a considerable effect on the design of the corresponding resource agent.

Resource Agents (RA) are pieces of software usually deployed on a computer, a processor or a microcontroller installed in the vicinity of the resource. For instance, in a generation or storage unit, the RA can be implemented within its controller, whereas a load agent can be installed in a building computer to monitor and control its aggregated power-consumption. RAs might have a simplified or sophisticated view of the internal behavior of their resources as a function of the RA developer. The better the resource model is, the more accurate advertisement messages sent to the GA will be, and the better the overall decision will be.

As a summary, we recall that each resource agent advertises its internal state to its grid agent using the following three elements.

1. The *PQ profile* $\mathcal{A}$ is the region in the (P, Q)-plane (for active and reactive power) that the resource under the control of a resource agent can be requested to implement.
2. The *belief function* $\mathcal{B}$ returns the set of all possible (actual) power flows that this resource *might* in reality implement when instructed to implement a target set-point. It accounts for the uncertainty of the resource operation. For practical aspects, this function should smoothly vary in time, as it is the main element used for assessing the *admissibility test* (see Section 3.2.4).
3. The *virtual cost* $\mathcal{C}$ is a function, defined for every $(P, Q) \in \mathcal{A}$, which returns a number interpreted as the willingness of this resource to apply a requested power set-point (P, Q). It is virtual in the sense that it is not directly related to monetary value.

Keep in mind that these three elements (i) are the only information needed for real-time control in the COMMELEC framework and (ii) they abstract the specific internal state of the resource.

4.1 Summary of Considered Resources

This section shows a summary of all designed resources agents.

- **Generic uncontrollable resources:** loads, generators or bi-directional resources that are simply non-controllable or out of the control of the COMMELEC grid agent.
- **Loads**
  - **Space-heating loads:** a general electric-based heating system for a building whose flexibility can be exploited for providing demand-side management.
  - **Water boilers:** water-storage loads that can provide flexibility to the grid.

- **Generation units**
  - **Synchronous generators:** a traditional rotatory machine.
  - **PV plants:** a photo-voltaic plant that can follow power set-points. This case is of main importance in view of the large penetration of solar power in distribution networks.
  - **Fuel cells:** hydrogen-based generator typically used in long-term storage systems.
- **Storage systems**
  - **Batteries:** general definition of a battery-based storage system.
  - **Supercapacitors:** short-term high-power storage for reacting to fast changes in the grid.

Recall that RA messages refer to the power flows at the point of connection with the grid, thus for DC-nature resources, **power converters** are always considered as part of the resource. This is the case for the underlined resources in the previous list. As converters can be used by all kind of resources, a separate section is dedicated to their representation as a simplified transfer function and power constraints.

Observation. *In general, the internal state and operation area of DC resources are defined by a combination of characteristics of the resource itself and the DC-AC power converter. As the latter can be represented with a standardized model for any resource of this type, the definition of the advertised elements is discussed only for the DC-side. A suitable transfer function is to be used to express the overall advertisement* $(\mathcal{A}, \mathcal{B}, \mathcal{C})$*. In particular for the PQ profile* $\mathcal{A}$*, an intersection between the DC-based constraints and the power converter constraints is to be performed.*

Here we present how to implement RAs in detail, specifically, how they manage the requests and produce the advertisements.

4.2 Operation of a Resource Agent

For any resource agent in the COMMELEC framework, the sending/receiving message cycle is repeated continuously and endlessly in normal operation. In this sense, an RA computes an advertisement just after receiving a request. The whole cycle of an RA is described next (see Figure 4.1).

1. At time k, reception of a new set-point request $(P, Q)[k]$. The request is to maintain this power fixed from k to $k + 1 = k + \Delta t$. Δt is defined by the GA and it is known for the RA. Observe that $(P, Q)[k]$ has been computed with the knowledge of $(\mathcal{A}, \mathcal{B}, \mathcal{C})[k - 1]$.

2. Check the feasibility of the requested set-point, given the actual instantaneous measured/estimated state in the resource (not available to the GA), and compute the verified set-point $(\tilde{P}, \tilde{Q})[k]$. Note that for resources with high uncertainty, the implemented power could significantly differ from the requested set-point, whereas it will be exactly the same (ideally) for fully controllable resources. This uncertainty was advertised in the previous belief function. This action also serves to maintain the resource safe in case the GA requests an invalid power set-point.

3. Instruct the resource to implement the verified set-point $(\tilde{P}, \tilde{Q})[k]$.

4. Compute and send the advertisement $(\mathcal{A}, \mathcal{B}, \mathcal{C})[k+1]$ based on local measurements. This advertisement should ensure that $(P, Q)[k]$ maintains the resource safe until time-step $k+1$.

5. Wait for a new request from GA.

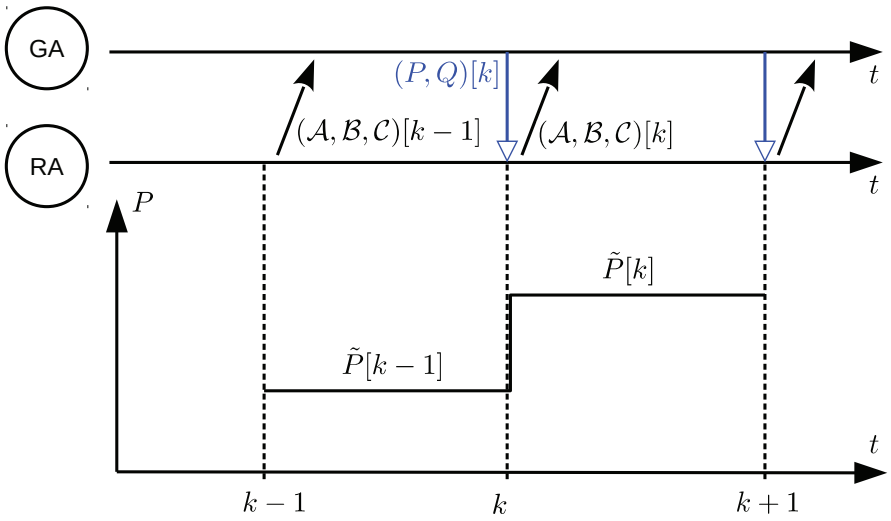

Figure 4.1 – Representation of the messages between GA and RA in time. The lower diagram shows the implementation of the requested set-point. For simplicity, only active power is shown.

We next detail the steps performed by different resource agents for implementing the requested set-points and computing the advertisement.

4.3 Uncontrollable Resources

We first present the simplest agent: the one in charge of a non-controllable resource. Without loss of generality, we focus on an uncontrollable load, but the concept can be applied also to any kind of uncontrollable resources.

Implementation of Set-Points. In this case, the agent disregards the requested set-point, as it does not have any way to set it.

PQ **Profile**. In principle, the resource has no available set-points, hence the PQ profile should be an empty set. In practice, as the virtual cost and the belief function are defined only in the domain of $\mathcal{A}$, an empty set could neglect useful information to the GA. Therefore, we define the PQ profile as a single point in the PQ-plane, allowing with this the ability to exhibit useful information even when the resource is not controllable. This singleton could be any single point, given that in practice it cannot be set. Still, as we want to express, in the belief function, the plausible set where the realization will belong, a good choice for the singleton is the actual implemented value as, in general, it will be close to the next realization

$$\mathcal{A} = \{(\hat{P}, \hat{Q})\}. \tag{4.1}$$

The best practice for such a resource would be to implement a forecasting tool that predicts its expected behavior. In this case, we recommend taking advantage of the forecasted powers P^f and Q^f to compute the PQ profile as

$$\mathcal{A} = \{(P^f, Q^f)\}. \tag{4.2}$$

Belief Function. Assuming that the only available information from the resource is the rated power S_r (there is no way to know what the consumption will be in the next time-step), the belief function should represent the entire area of operation of the load defined by S_r. Formally,

$$\mathcal{B}(P, Q) = \{(P, Q) \in \mathcal{A} : P^2 + Q^2 \leq S_r^2, P < 0\}. \tag{4.3}$$

Alternatively, by making use of a forecasting tool, the belief set could be considerably shrunk to a small set around the expected value (P^f, Q^f). If we assume separated and uncorrelated prediction methods for P and Q, we can consider $[\underline{P}, \overline{P}]$ and $[\underline{Q}, \overline{Q}]$ the active and reactive predicted power-ranges, respectively. Hence, we can simply have

$$\mathcal{B}(P, Q) = \{(P, Q) \in \mathcal{A} : P \in [\underline{P}, \overline{P}], Q \in \underline{Q}, \overline{Q}]\}. \tag{4.4}$$

Observe that the rectangular definition of the belief set comes from the uncorrelated prediction assumption. But, for example, in the case when considering the node voltage as a source of the uncertainty of the resource, both magnitudes are correlated, and the belief set will have to account for that.

Examples for PQ profiles and belief functions for both possibilities presented before are shown in Figure 4.2.

Virtual Cost. As the agent cannot control its resource, we set the advertized virtual

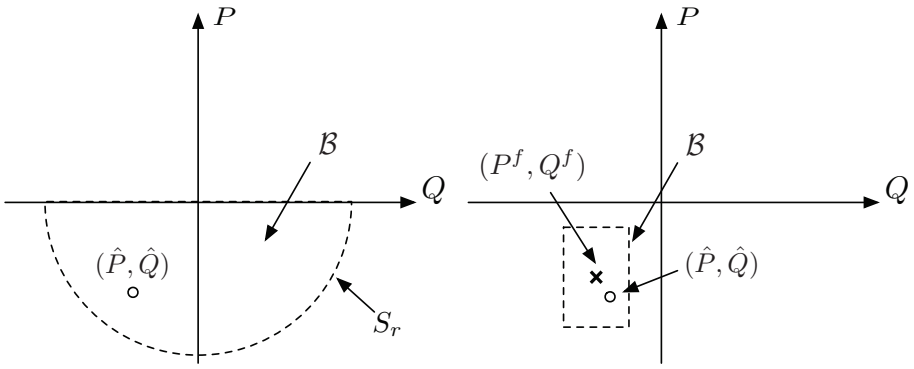

(a) Without any additional information. (b) Using a forecasting tool.

Figure 4.2 – PQ profile and belief functions for uncontrollable resources.

cost to

$$\mathcal{C}(P, Q) = 0. \tag{4.5}$$

We note that, in our implementation of the grid agent, only the *gradient of the cost* is used by the employed gradient-descent algorithm. Hence, the uncontrollable load-agents can have any *constant* cost without influencing the set-points computation procedure.

4.4 Space-Heating Load with Discrete Power Steps

In this section, we propose the design of an agent in charge of the electrical-heating system of a building, whose intrinsic flexibility consists of temperature comfort bounds $[T_{min}, T_{max}]$. We model the building with n rooms, each of them having an electrical heater with an on-off state. The model that uses discrete state-space formulation, as in [94], includes the building thermal dynamics, the influence of the external temperature and the solar irradiance. The agent can be adapted to buildings of any size and type, provided that the heating system is electric and air temperature measurements are available in each controlled volume.

Without loss of generality, we consider that the heaters are purely resistive, hence $Q = 0$. Figure 4.3 shows how the load process is conceived. The details will be explained next.

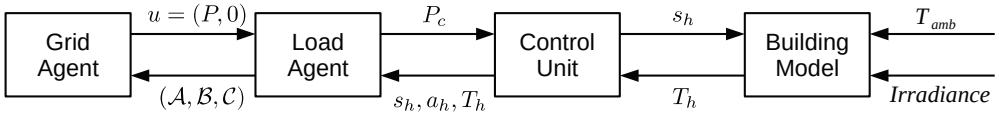

Figure 4.3 – Full process of the emulated load.

4.4.1 Heating System Control Unit

The control unit (CU) of the heating system is a piece of software that knows the state s_h (on/off), the rated power P_h, the availability a_h (i.e., if it is able to change state), and the temperature T_h of a room associated to a heater $h \in \mathcal{H}$, being $\mathcal{H}$ the set of all heaters in the building. We rely on the assumption that each room has an electrical heater, so n is also the number of heaters. It is also assumed that the CU can directly act on the switches supplying the heaters. The model of this controller is of special importance as its behavior has a direct impact on the flexibility of the resource, regardless of the agent design.

We next detail the proposed implementation of the CU and the way it accomplishes its various goals. These goals and actions are sequentially executed, as they are presented here.

Locking heaters

First, the CU will lock the heaters that have recently changed their state. This locking is needed in order to avoid continuous switching. Such a consideration is typically done in real switching devices to avoid rapid deterioration and aging. The locking period, τ_l, is set to be constant. The CU tracks the state of a heater s_h and initializes a counter $c_h = \tau_l$ when a change occurs. The counter will be reduced as the time passes. A room will be not available if $c_h > 0$.

Keep rooms temperature inside comfort bounds

If the temperature of a room is out of bounds, the CU will automatically set the state of the associated heater accordingly (OFF for $T_h > T_{max}$ and ON for $T_h < T_{min}$) and will force the heater to be *not-available*. We define

$$\mathcal{Z} = \{h \in \mathcal{H} : a_h = 1\}, \tag{4.6}$$

the set of all available heaters, whereas the *availability* is computed as

$$a_h = \begin{cases} 0 & \textbf{if } c_h > 0 \text{ or } T_h > T_{max} \text{ or } T_h < T_{min} \\ 1 & \text{otherwise.} \end{cases} \tag{4.7}$$

At this point, the state of the non-available heaters is already set

$$\forall h \notin \mathcal{Z}, \qquad s_h = \begin{cases} 1 & \textbf{if } T_h < T_{min} \\ 0 & \textbf{if } T_h > T_{max} \\ s_h & \text{otherwise.} \end{cases} \tag{4.8}$$

Handling external requests

In order to permit the heating system to follow external commands P_c, we first check how much flexibility is not usable given the heaters availability. This is direct from the definition of a_h. In this respect, the power to be consumed by the available rooms is the difference between the external set-point and the power of the non-available heaters that are forced to be switched ON, that will represent a base consumption. Mathematically,

$$P_{on} = P_c - \sum_{h \in \mathcal{X}} P_h, \tag{4.9}$$

where

$$\mathcal{X} = \{h \in \mathcal{H} : a_h = 0, s_h = 1\}. \tag{4.10}$$

Maximize power flexibility

Observe that the flexibility is lost when a heater is not available. As the comfort bounds are strict constraints, in order to maximize the aggregated flexibility, we can only rely on avoiding locking a heater, thus minimizing the heater state changes. To accomplish this, we sort the heaters in $\mathcal{Z}$ twice: first by temperature and then by state, so that in the array we find first the heater whose room temperature is the lowest among the heaters that are switched ON. An example of the sorting for a 4-rooms building is shown in Figure 4.4.

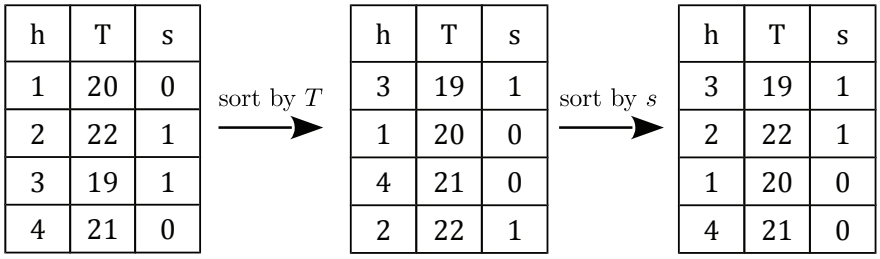

Figure 4.4 – Sorting available rooms to maximize flexibility.

Then, we iterate through the sorted set until the power of the heaters adds up P_{on}. The simplest algorithm is presented in Algorithm 3.

4.4.2 Flexible-Building Agent

First note that, due to the discrete nature of the heaters consumption and the continuous nature of the GA requests, an error ϵ between the implemented power and the external set-point can be caused. This error should be bounded (or even reduced if possible) over

Algorithm 3 Select heaters to be ON to follow external set-point

Require: P_{on}, $\mathcal{Z}$
  $\mathcal{Z}_T = sortByT(\mathcal{Z})$;
  $\mathcal{Z}_s = sortBys(\mathcal{Z}_T)$;
  for all $h \in \mathcal{Z}_s$ **do**
    if $P_{on} - P_h \geq 0$ **then**
      $P_{on} = P_{on} - P_h$;
      $s_h = 1$;
    else
      $s_h = 0$;
    end if
  end for

time.

Implementation of Set-Points First, as with any other agent, the flexible building agent will check the actual state of the device and project the request into the feasible region of operation. The projected request is $\tilde{P}$. To handle the error, and assuming for simplicity that all heaters have the same rated power P_r, at each time-step k the agent sends to the CU the command $P_c[k]$ defined as

$$P_c = \text{round}\left(\frac{\tilde{P} + \epsilon}{P_r}\right) P_r, \tag{4.11}$$

where the error is calculated as

$$\epsilon[k+1] = \epsilon[k] + k_p(\tilde{P}[k] - \hat{P}[k]), \tag{4.12}$$

the value of k_p determines the speed of convergence and $\hat{P}$ is the measured implemented power.

PQ **Profile.** The objective of the agent is to guarantee that the rooms temperatures are always within their comfort bounds. We assume therefore that we have access to the information that the CU tracks. Recall that in our convention, a load has *negative power*. With this in mind, the *PQ* profile can be computed as the interval defined by

$$\mathcal{A} = \{(P, Q) : P_{min} \leq P \leq P_{max}, Q = 0\}, \tag{4.13}$$

where, on a first side, P_{max} is the bound imposed by the heaters that are not-available and turned ON. Recall that this includes both the locked heaters and those where the room temperature is lower than the lower bound.

$$P_{max} = \sum_{\substack{h \notin \mathcal{Z} \\ s_h = 1}} P_h. \tag{4.14}$$

On its side, P_{min} is the bound imposed by the not-available heaters that turned OFF in the previous step, with a similar interpretation.

$$P_{min} = \sum_{h \in \mathcal{H}} P_h - \sum_{\substack{h \notin \mathcal{Z} \\ s_h = 0}} P_h. \tag{4.15}$$

Belief Function. In this case, the belief function uses the error ϵ to indicate the expected implemented value for a given set-point, namely

$$\mathcal{B}(P, Q) = \left(\text{round} \left(\frac{P + \epsilon}{P_r} \right) P_r, 0 \right). \tag{4.16}$$

Note that the resulting set is a single point that is a function of ϵ that, by the definition of Equation (4.12), is bounded to $|\epsilon| \leq P_r/2$.

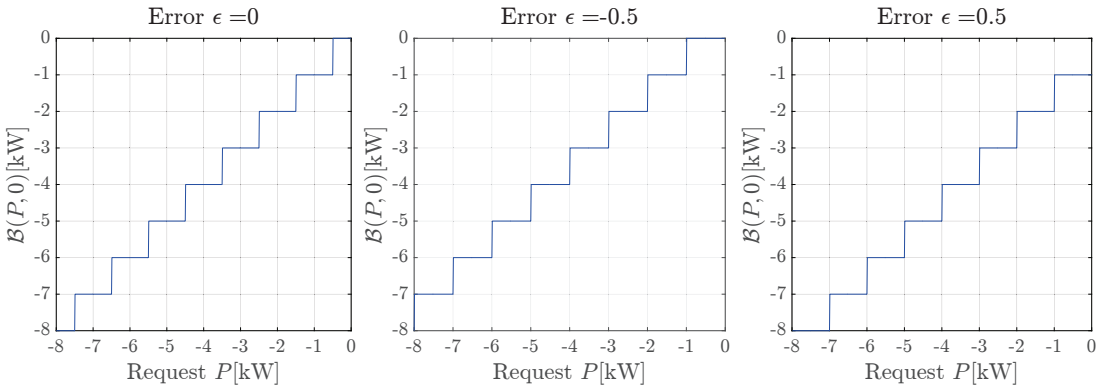

Figure 4.5 – Example of belief function for discrete load steps of 1[kW]

Virtual Cost. We try to steer the rooms to have a temperature that is as close as possible to the average temperature of the comfort interval ($\bar{T}$). Hence, the cost function is defined in general as

$$\mathcal{C}(P) = aP^2 + bP + c. \tag{4.17}$$

We want to define a cost such that it is minimum when the heaters of all the rooms temperature below $\bar{T}$ are switched ON and the rest are OFF, so that we enforce all rooms to be around $\bar{T}$. In other words, when the consumed power is

$$P^* = \sum_{\substack{h \in \mathcal{H} \\ T_h \leq \bar{T}}} P_h, \tag{4.18}$$

the cost is zero (chosen arbitrarily). For simplicity, we next fix the maximum possible

cost to 1, so that the entire definition of $\mathcal{C}$ lies in the range $[-1, 1]$. Defining

$$\overline{P} = \sum_{h \in \mathcal{H}} P_h, \tag{4.19}$$

we can add to the definition the restrictions

$$\begin{aligned} \mathcal{C}(0)|_{P^*=\overline{P}} &= 1, \\ \mathcal{C}(\overline{P})|_{P^*=0} &= 1, \end{aligned} \tag{4.20}$$

And parameters of the cost function result in

$$a = \frac{1}{\overline{P}^2}, \quad b = \frac{-2P^*}{\overline{P}^2}, \quad c = \left(\frac{P^*}{\overline{P}}\right)^2. \tag{4.21}$$

Note that, as the GA uses a gradient-descent strategy, c can be disregarded. With this, the advertised virtual cost can be written as

$$\mathcal{C}(P) = \frac{1}{\overline{P}^2}(P^2 - 2P^*P). \tag{4.22}$$

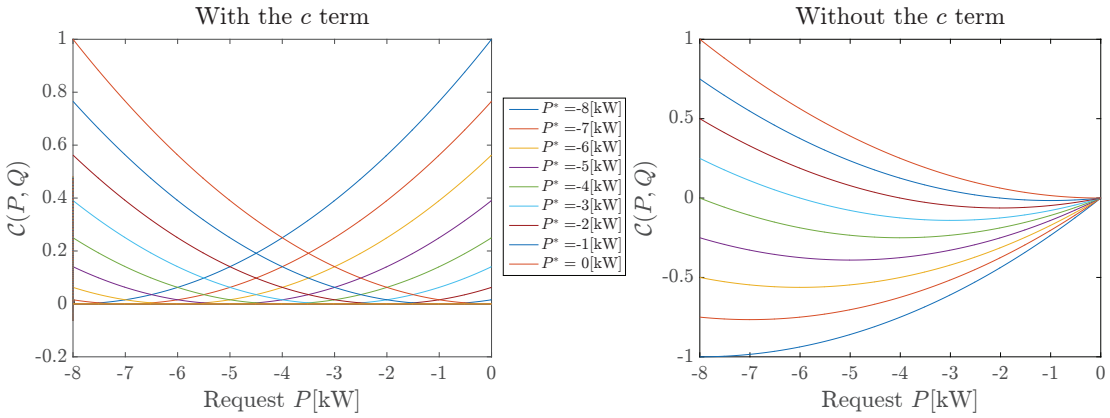

Figure 4.6 – Cost function defined by the agent, for the example of 1[kW] heaters.

4.5 Water Boilers

We consider thermal controllable loads such as *water boilers* (WB). Each controllable load is considered as a *single* boiler capable of estimating its own thermal state. Eventually, the approach could be extended to *distributed* controllable loads (e.g., [77]).

As with the discrete heating system, for this resource we consider only active power, namely $Q = 0$.

4.5.1 Water-Boiler Model

We assume that the internal controller of the WB is capable of any active power in $[P_{min}, 0]$, i.e., it is a continuous device. Next, we assume that the thermal state of the boiler is represented by the total energy stored in it at time t, given by

$$\mathcal{E}(t) = \int_{\tau=0}^{t} (P_{in}(\tau) - P_{out}(\tau))d\tau, \tag{4.23}$$

where $P_{in}(t)$ is the absolute value of the power injected into the water reservoir, and $P_{out}(t)$ is the absolute value of the power drawn from the reservoir (e.g. for heating consumption). The process $\{P_{out}(t)\}$ is the source of uncertainty in this resource, as it is affected by nature and demand patterns of the users of the boiler. The process $\{P_{in}(t)\}$, on the contrary, is controlled by the water-boiler agent (WBA).

4.5.2 Water-Boiler Agent

Implementation of Set-Points. For this implementation, we consider that we can always find a way to avoid the WB controller deciding to change the operation without being instructed to do so. In other words, we assume that a WB decision subsequent to an emergency condition (e.g., when hitting a boundary constraint) is instructed only after a COMMELEC cycle[1].

With this consideration, the WBA checks the viability of the request by computing the allowable power range and projecting request into it. The result will be then sent to the WB controller.

PQ **Profile**. The operational constraints of the WB are: its rated power, P_r, and the energy bounds given by $\mathcal{E}(t) \in [\mathcal{E}_{min}, \mathcal{E}_{max}]$.

Even though the WBA has controllability over the process $\{P_{in}\}$, the process $\{P_{out}\}$ is highly uncertain. To account for this uncertainty, we assume that the WBA has a forecasting tool to predict the load profile. Let $[\underline{P}^f_{out}(t), \overline{P}^f_{out}(t)]$ denote the confidence interval of the forecast at time t ($P_{out} > 0$). For typical sizes of water boilers (e.g., 5[kW], 5[kWh]), P_{in} will be mostly limited by the rated power and P_{out} will slightly modify the energy stored in one COMMELEC cycle (we recall here that one COMMELEC cycle is of around 100[ms]). We therefore propose, at each discrete time-step k, to compute the

[1]For this resource, this is of special concern. Allowing the internal controller to act by its own during a COMMELEC cycle can mean that in one time-step the belief set of a power set-point P is large (for instance from P to 0 if the maximum energy bound can be violated) and in the next one, after the action took place, it shrinks down to singleton ($\{0\}$ in order to avoid further violation). This would violate the principle of design of the belief function, as presented in the introduction of this chapter. Another possibility would be to define a belief function such that it changes smoothly while approaching the operational limits.

power operational limits at the next time-step as (recall that the load has negative power)

$$P_{max}[k+1] = -\max\left(0, \frac{\mathcal{E}_{min} - \mathcal{E}[k]}{\Delta t} + \overline{P}^{f}_{out}\right), \tag{4.24}$$

$$P_{min}[k+1] = -\min\left(P_r, \frac{\mathcal{E}_{max} - \mathcal{E}[k]}{\Delta t} + \underline{P}^{f}_{out}\right). \tag{4.25}$$

And, therefore, as with other resources, we define the PQ profile as

$$\mathcal{A} = \{(P,Q) : P_{min} \leq P \leq P_{max}, Q = 0\}. \tag{4.26}$$

Belief Function. As there is no uncertainty related to the process $\{P_{in}\}$, which is the one to which the GA has access, the belief function is ideal, namely $\mathcal{B}(P,Q) = \{(P,0)\}$.

Virtual Cost. We assume that the basic goal of WBA is to keep the stored energy at a certain target level $\mathcal{E}_{target}$. Therefore, the virtual cost function advertised by WBA can be defined as

$$\mathcal{C}(P,Q) = \frac{\Delta\mathcal{E}}{3\mathcal{E}_{max}}\left(\frac{sgn(\Delta\mathcal{E})(P - P^{f}_{out})^2}{P_r^2} - \frac{2(P - P^{f}_{out})}{P_r}\right), \tag{4.27}$$

with $\Delta\mathcal{E} = \mathcal{E} - \mathcal{E}_{target}$ and P^{f}_{out} the forecasted expected power drawn for the reservoir.

4.6 Synchronous Generator

Let us take for simplicity the case of cylindrical rotor machines, where the agent uses the traditional model for the generator (both equivalent circuit and relevant capability curves), as in [95], and we assume that they are interfaced to the network through an appropriate transformer or power converter. Furthermore, we assume that, in general, a small synchronous generator will not be selected as a slack resource in a microgrid with renewable penetration simply because it does not allow bi-directional power flow. In this sense, in an islanded condition, the frequency in the system can be always imposed by a converter-interfaced resource that keeps it constant. We can therefore express the behavior of this resource by simply using algebraic equations. This assumption appears reasonable in view of the typical capacity of synchronous machines connected to LV grids. Note that this simplification is done only for sake of simplicity, but not because of a limitation of the framework.

Implementation of Set-Points. When receiving a request, the SG agent (SGA) computes the current limits of the resource by using the measurement of the voltage in the connection point V. These limits correspond to the well-known capability curves of a synchronous machine defined by maximum and minimum active power P_{max} and P_{min}, maximum field-current I^{f}_{max}, maximum line current I^{l}_{max}, and stability limit. Furthermore,

the SGA commands the implementation of the projection to the capability curves.

PQ **Profile**. As the bounds of this resource are dependent on V that is in turn dependent on external variables, the prediction of the limits in the next time-step is a non-trivial task. The voltage-dependent constraints are represented by the set $\mathcal{G}(V)$. This set is not necessarily monotonic with respect to V, therefore a largest set $\mathcal{G}^l$ and smallest set $\mathcal{G}^s$ are to be computed as a function of V (see Figure 4.7 for an example). The SGA will hence advertise

$$\mathcal{A} = \{(P, Q) : (P, Q) \in \mathcal{G}^l\}. \tag{4.28}$$

The variations on V are accounted for in the belief function.

Belief Function. Due to changes in V, the boundaries of the capability curves might vary at a given time-step. Thus, some set-points, in this case those nearest to the bounds, might be shifted to $\mathcal{G}^s$. Thus, the belief function can be defined as

$$\mathcal{B}(P, Q) = \begin{cases} (P, Q), & \text{if } (P, Q) \in \mathcal{G}^s, \\ \text{line}((P, Q), \mathcal{P}_{\mathcal{G}^s}(P, Q)), & \text{if } (P, Q) \in \mathcal{G}^l \setminus \mathcal{G}^s, \end{cases} \tag{4.29}$$

where $\mathcal{P}_{\mathcal{G}^s}$ is the Euclidean projection to $\mathcal{G}^s$, and $\text{line}(a, b)$ the line between points a and b. An illustration of both PQ profile and belief is presented in Figure 4.7.

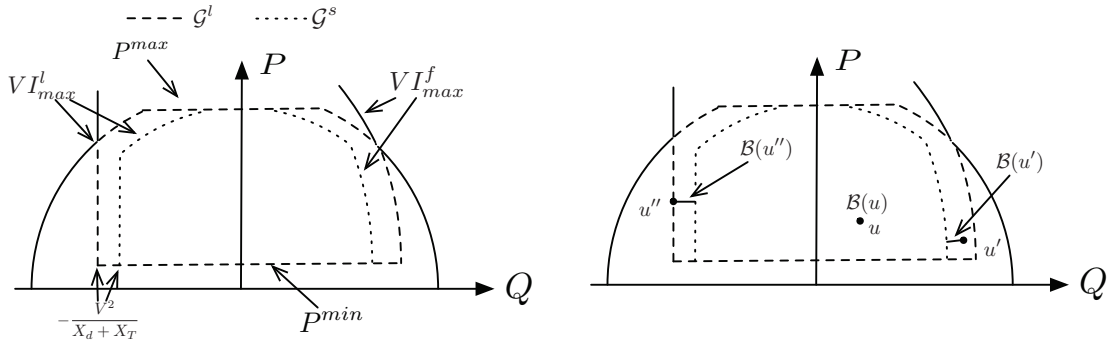

(a) PQ profile $\mathcal{A}$ (b) Belief function $\mathcal{B}$

Figure 4.7 – PQ profile and belief function (for different requests) of a cylindrical rotor synchronous machine. X_d and X_T are the direct-axis stator and transformer impedances.

Virtual Cost. To express the virtual cost, we consider that the SGA operates the resource in order to maximize its overall efficiency. As the efficiency of the turbine, given an electrical produced power $\eta(P)$, plays the most important role in the overall efficiency, we define the virtual cost as $\mathcal{C}(P, Q) = (1 - \eta)$. For an example, we present the cost

function in Figure 4.8.

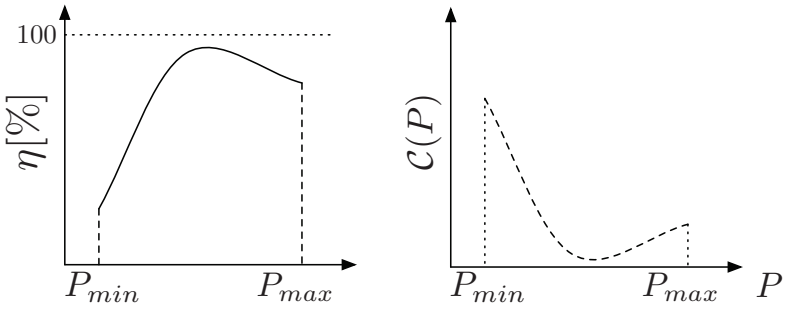

Figure 4.8 – Efficiency curve of a turbine (left) and cost function of SG agent (right).

4.7 Power Converters

The resources presented after this section are interfaced with the grid by using power converters. Here, we summarize the considerations on the modeling and their effect on the development of the agents.

First, we consider that the admissible area of operation of power converters can be modeled with three general constraints:

(i) *The PQ capability curve of a three-phase converter*, which is in general given by

$$\sqrt{P^2 + Q^2} \leq \sqrt{3}\hat{V} I_n, \tag{4.30}$$

where P and Q are the active and reactive power of the converter, I_n the nominal line current and $\hat{V}$ the actual measured voltage, both on the AC-side of the converter. As $\hat{V}$ can be externally affected, the resulting power constraint has an uncertainty (indeed, $\hat{V} = f(t)$) that could be reflected in the belief function.

Alternatively, it could be considered that a converter is simply constrained by its nominal rated power S_r in which case the capability curve will be defined by

$$P^2 + Q^2 \leq S_r. \tag{4.31}$$

(ii) *The power factor constraint*, given by

$$\left| \frac{P}{\sqrt{P^2 + Q^2}} \right| \geq \cos(\phi)_{min}, \tag{4.32}$$

where $\cos(\phi)$ stands for the power factor of the converter and ϕ the phase-shift between voltage and current phasors. This constraint is relevant, for instance, in the case of PV converters that are required to operate with such a constraint.

(iii) *Unidirectional or bidirectional converter*, depending on the nature of the resource. For instance, a grid-tie PV usually cannot absorb active power, thus $P \geq 0$. In the case of an energy storage system, we consider a unique bidirectional device for charge and discharge.

Next, we need to define the effect of the converter on the delivered power. Without loss of generality, we focus from here on DC-AC converters. In general, as the converter dynamics are much faster than the expected COMMELEC behavior (tens of kHz in contrast with tens of Hz), the specific details can be hidden with a transfer function $(P, Q) = f(p)$, with p the DC-side power.

For instance, we could assume that a constant efficiency (η) accounts for the effect on the DC power, depending on the power flow direction:

$$P = \begin{cases} \eta(p)p, & \text{if } p \geq 0, \\ \frac{p}{\eta(p)}, & \text{if } p < 0. \end{cases} \tag{4.33}$$

But in practice, this could exhibit low accuracy for small power-magnitudes, especially when they are interfaced through transformers that have non-negligible losses. Instead, another more recommendable practice would be to fit function $f(\cdot)$ using actual measurements. In Figure 4.9 we show an example of a possible curve fitting.

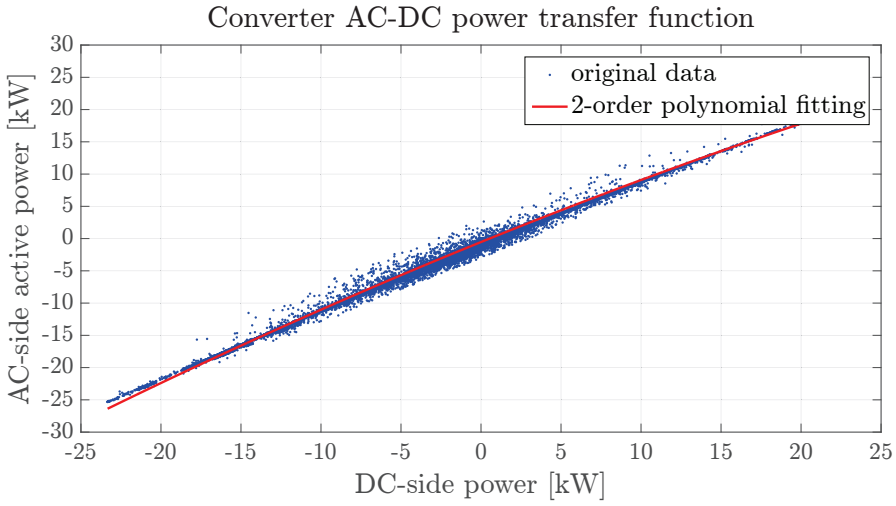

Figure 4.9 – Example of a DC-AC converter transfer function for active power.

4.8 PV Plant

In this section, we show a way to exploit the flexibility of a PV plant, where the term *flexibility* means the capacity of curtailing the generation of this resource, along with

the possibility of controlling its reactive-power injection. The former can be needed, for instance, when there is excess of energy in the grid that cannot be immediately stored, whereas the latter is for voltage regulation. We study the general case when a certain power-factor restriction is imposed, and we make use of the elements of the COMMELEC advertisements to express the irradiance uncertainty.

As for the Observation in Section 4.1, we expose the irradiance uncertainty on the DC-side, whereas the power-factor constraint on the AC-side. Note that, we use the lowercase for DC powers and the uppercase for AC ones.

Implementation of Set-Points. Using local measurements, we assume that the PV agent (PVA) can obtain the current maximum admissible power production P_{max}. For instance, we can make use of the behavior of a maximum-power-point tracking (MPPT) technique to define the maximum available power for the next 200[ms]. Then, the PVA controls its resource to set the request projected to the admissible set defined by this bound and the converter limits from Section 4.7.

PQ **Profile**. We first focus on the maximum available power defined by the uncertainty of the irradiance. For an example, we consider a setup where the temperature of the cell array and the global irradiance measurements are continuously available.

Then we use a forecasting tool to estimate the range where the global irradiance (expressed in [W/m^2]) will lie in the next time-step $P^{irr}[k+1] \in [P^{irr}_{dw}, P^{irr}_{up}]$, with k the current instant. Using this range and a suitable PV plant model, we can compute the range where p will lie $[p_{dw}, p_{up}]$, which we can then express on the AC-side as $[P_{dw}, P_{up}]$. Secondly, we apply the power converter constraints. As is typical for the grid-tie PV converters, a constraint on the reactive power production, given by a minimum power factor PF_{min} as in Equation (4.32) and a rated power S_r constraint.

$$\mathcal{A} = \{(P,Q) : 0 \leq P \leq P_{up}, \sqrt{P^2+Q^2} \leq S_r, \arctan(P/Q) \leq \arccos(\mathrm{PF}_{min})\}. \quad (4.34)$$

Belief Function. As the uncertainty is linked to the prediction interval $[P_{dw}, P_{up}]$, we can define singleton belief sets equal to the set-point for all $P \leq P_{dw}$. For those set-points lying in the prediction interval, we define a line from the set-point P to P_{dw} and consider that the reactive power could also be different as a consequence of the power factor constraint. We can write therefore the belief function as

$$\mathcal{B}(P,Q) = \begin{cases} \{(P,Q)\}, & \text{if } P \leq P_{dw}, \\ \mathrm{line}((P,Q),(P',Q)) \cup \mathrm{line}((P',Q),(P_{dw},Q')) & \text{otherwise}, \end{cases} \quad (4.35)$$

where the active power constraint P' is expressed as

$$P' = Q \tan(\arccos(\mathrm{PF}_{min})), \quad (4.36)$$

whereas the reactive-power constraint Q' is

$$Q' = sgn(Q)P_{dw}\frac{\sqrt{1-\mathrm{PF}_{min}^2}}{\mathrm{PF}_{min}}, \tag{4.37}$$

that is defined for all P'. An example of PQ profile and belief function is shown in Figure 4.10.

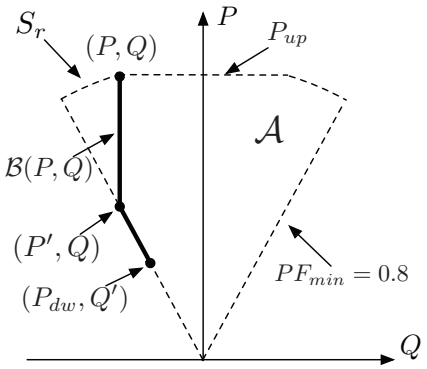

Figure 4.10 – PQ profile and belief function defined by a PV Agent. Note that the prediction interval width $P_{dw} - P_{up}$ has been intentionally exaggerated for visualization purposes.

Virtual Cost. We assume that the PVA seeks to maximize the active-power production and minimize the reactive power. This latter desire of the PVA is due to the need of reducing the losses in the PV converter, associated with the injection of reactive power. Therefore, an example of the advertised virtual cost function is given by

$$\mathcal{C}(P,Q) = -\frac{P}{S_r} + \frac{Q^2}{S_r^2}. \tag{4.38}$$

4.9 Fuel Cell

In this section, we consider the case of a proton-exchange-membrane (PEM) fuel cell that can be used to provide controllable power injection to the microgrid. In general, a fuel cell operates with fixed-input hydrogen pressure, whereas its state can be determined by the produced DC current i and the stack temperature T. To compute the three elements of the advertisement, we present first the model that the fuel cell agent uses.

4.9.1 Fuel Cell Model

The main working hypothesis for the derivation of the fuel cell model is that the time-constants that represent the changes in the stack average-temperature can be considered

large compared to the COMMELEC time-frame control action. Therefore, we can assume that the stack temperature T does not change between two consecutive control actions, hence it does not represent a state variable of the model. In this respect, the standard fuel cell model for computing the *polarization curve*, which is the direct relation between its DC current i and voltage v (temperature T is given), is:

$$v = v_0|_T - v_c(i)|_T - v_a(i)|_T - v_l(i)|_T, \tag{4.39}$$

where v_0 represents the constant open-circuit voltage of the stack, v_c the concentration losses, v_a the activation losses and v_l the ohmic losses. In general, v_0 depends on T and on the pressure of the gases. However, in systems of this size, it can be considered as a constant value, as its variations with T are negligible and the input pressures are typically controlled to be constant. On the contrary, v_c, v_a and v_l are dependent on T and i. In the literature, several options can be found for expressing these voltages [96, 97, 98]. Here, we consider for v_c an exponential behavior, and for v_a the approximation presented in [67]. In summary, the expressions are

$$v_0 = \alpha, \tag{4.40}$$
$$v_c = (\beta_1 T + \beta_2)e^{\beta_3 i}, \tag{4.41}$$
$$v_a = (\gamma_1 T + \gamma_2)\sqrt{i}, \tag{4.42}$$
$$v_l = (\delta_1 T + \delta_2)i, \tag{4.43}$$

where α directly represents the open-circuit voltage, parameters β_i the change in concentration of the reactant at high current densities, parameters γ_i the behavior of the speed of the reaction at low current as a function of the stack temperature, whereas parameters δ_i are used to represent a temperature-dependent resistance. These parameters are to be inferred from a fitting procedure that, such as maximum likelihood estimation [67], wants to maximize the probability that the model can explain a set of operation measurements.

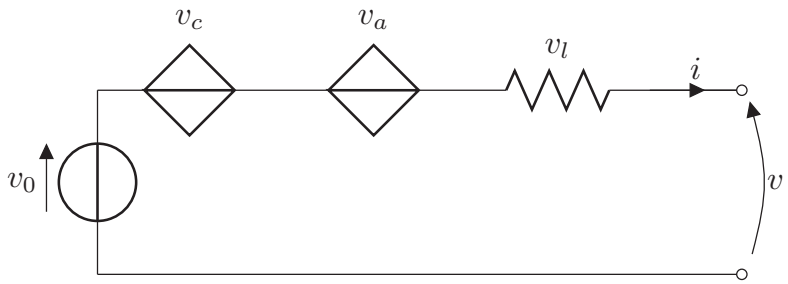

Figure 4.11 – Equivalent circuit of the fuel cell model.

Note that, when i increases, the voltage deteriorates significantly, therefore the power extraction from the stack decreases due to concentration losses. As the objective of the fuel cell is to provide power, there is no reason for operating at higher values of

currents. Therefore, this will define an operational limit that depends on the stack surface temperature T.

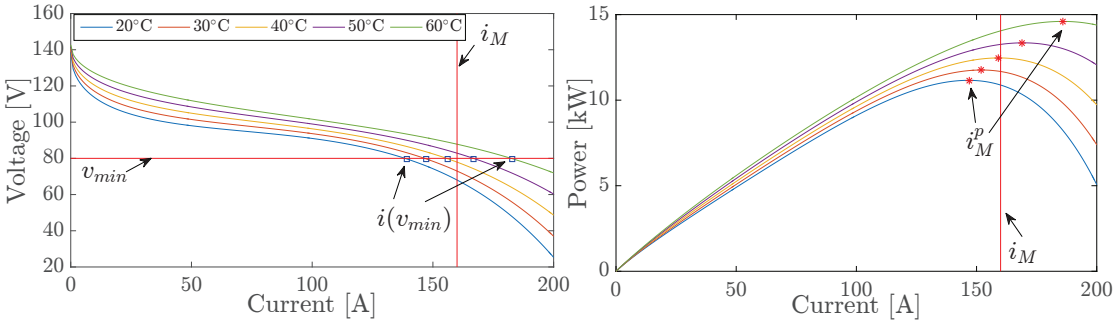

Figure 4.12 – Typical shape of polarization and power curves of a fuel cell stack, together with its the operational limits.

4.9.2 Fuel Cell Agent

Implementation of Set-Points. As for the assumption of a constant stack temperature, the set-point implementation is restricted to the PQ profile that will be sent to the GA and that is discussed in the next section.

PQ **Profile**. The fuel cell operation is limited by several constraints (see Figure 4.12 for an example):

1. **Maximum current density:** Typically defined by the technology of the cells, this limit defines the absolute maximum current the stack can withstand i_M.

2. **Minimum voltage:** Power converters are normally restricted to working with a minimum DC voltage limitation v_{min} in order to enable the conversion in the whole power range.

3. **Maximum power:** Due to concentration losses, the voltage might dramatically drop when increasing the output current, thus resulting in a reduction of the delivered power (as seen in Figure 4.12). The current for which the power is maximum will define a new limitation that depends on the stack surface temperature $i_M^p|_T$.

4. **Ramping:** Additionally, as the process is based on a chemical reaction, the extracted power cannot be raised instantaneously, therefore, a ramping limit $\rho^+[A/s]$ is imposed. In the opposite direction (power reduction), there is no limitation.

Note that for a given stack temperature the behavior of $v = f(i)$ is monotonic, as all associated losses are always positive in the normal operation range [99, 100, 101]. Therefore, all operational limits can be expressed as a current bound. Thus, the overall

maximum current limitation will be then computed as

$$i_{max} = \min(i_M, i(v_{min})|_T, i_M^p|_T, \hat{i} + \rho^+ \tau), \tag{4.44}$$

where $\hat{i}$ is the actual measured current and τ is the expected delay that a new request will take on arriving from the GA (in our case around 100[ms]). The maximum DC power will be then defined as $p_{max} = v(i_{max})i_{max}$. This computation can be safely done as $p(i)$ is monotonic with i in the operational range $i < i_M^p|T$.

Additionally, in order to avoid reverse power-flow, we need to constrain $i_{min} = \epsilon$, with $\epsilon > 0$ a small safe margin. Consequently, the computation of the power limitation is $p_{min} = v(i_{min})i_{min}$. Finally, we need to consider the power-converter constraints for getting the bounds on the AC side (active and reactive) in order to express the PQ profile.

Belief function. We assume for this device that there is no uncertainty related to the implementation of external requests, thus the belief function is ideal $\mathcal{B}(P, Q) = \{(P, Q)\}$.

Virtual cost. First, we assume that the fuel-cell system would prefer to operate while maximizing its efficiency, which means in this case, the conversion of the power given by the hydrogen flow into electricity

$$\eta(i) = \frac{vi - p_{aux}}{ki}, \tag{4.45}$$

with p_{aux} as the additional power needed for supplying the auxiliaries of the FC system (e.g., the cooling system) and k as a constant that expresses the available power from hydrogen for a given current magnitude[2].

We need, however, to express this efficiency as a function of the delivered power $\eta(p)$. As from Equation (4.39), the analytic definition of $i(p)$ (needed for replacing the term ki in Equation (4.45)) is non-trivial, as it comes from the result of a non-linear equation that has several solutions. We propose instead, to numerically compute it by evaluating on-the-fly the polarization curve for a given T in the current range $i \in [i_{min}, i_{max}]$.

The numerical assessment of the efficiency cost function is simply calculated as $\xi = -\eta$ in the feasible current operational range. In order to send a continuous and differentiable function to the GA, we propose to interpolate the sampled cost function, by using a suitable spline $\mathcal{S}_\xi(P)$.

Additionally, as typically suggested by FC manufacturers, we consider that the stack will prefer to smoothly change its operation power; therefore, we add a time-dependent cost,

[2]The exact expression is $k = \frac{m_{H_2} N_c HV_{H_2}}{2F}$ where m_{H_2} is the molar mass of the H_2 molecule, N_c the number of cells in the stack, HV_{H_2} the lower heating value of the H_2 molecule and F the Faraday constant.

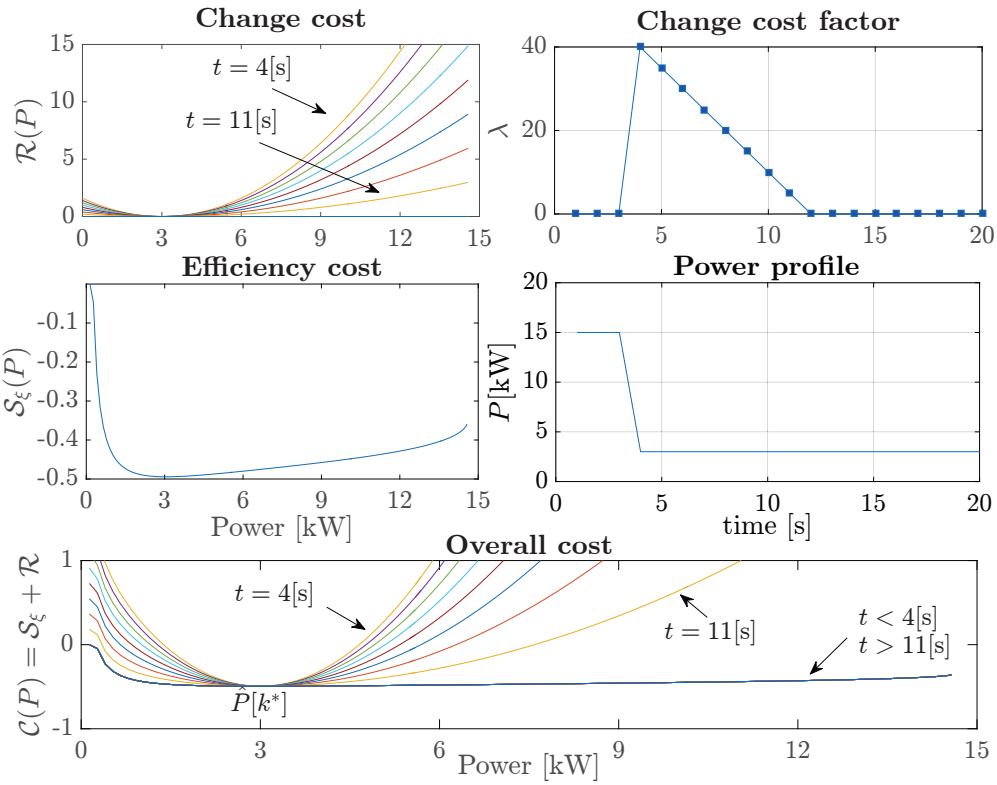

Figure 4.13 – Cost function behavior in time. At $t = 4$[s] there is a power change from 15[kW] to 3[kW]. For this case we have chosen $\omega = 50$ and $\tau = 10\%$. For this representation we use 1[s] period.

$\mathcal{R}(P)$ that we call *Change Cost*. This cost is defined such that it is large when there is a power change and decreases linearly in time (other possible functions can be used for the same purpose). For any time-step k, it might be expressed as

$$\mathcal{R}(P) = \lambda[k]\frac{1}{S_r^2}(P - \hat{P}[k^*])^2, \tag{4.46}$$

where $\hat{P}$ is the measured power, S_r is the rated power of the fuel-cell system and k^* is the time-step when the following conditions hold:

(i) the factor $\lambda = 0$ and

(ii) a power change occurred, namely, $|\hat{P}[k^*] - \hat{P}[k^* - 1]| > 0$.

The factor λ is computed as

$$\lambda[k] = \begin{cases} \omega\frac{|\hat{P}[k] - \hat{P}[k-1]|}{S_r} & \text{if } \lambda[k-1] = 0 \\ \max(0, \lambda[k-1] - \omega\tau) & \text{otherwise.} \end{cases} \tag{4.47}$$

with ω a scaling-parameter that defines the effect of the penalty (the higher the values are, the more the effect there is) and $0 < \tau < 1$ a linear decrease parameter. Note that $0 < \lambda < \omega$.

Hence, the advertised cost function of a fuel-cell system will be (see Figure 4.13):

$$\mathcal{C}(P, Q) = \mathcal{S}_\xi(P) + \mathcal{R}(P). \tag{4.48}$$

Observe that, when $\lambda = 0$, an important change in the request can occur. However, this is limited by the ramp constraint embedded into the PQ profile.

4.10 Battery Bank

In order to express the state of a battery tank in the COMMELEC framework, the battery agent (BA) needs a model to compute the internal limits this resource must respect for the next time-step.

4.10.1 Battery Model

Here, we consider that such an agent uses a simple model that can sufficiently represent the dynamic behavior of the battery in the considered time-frame. In particular, assuming that the state-of-charge (SoC) is fixed between two set-point implementations[3], we can express the model of the battery as a simple time-varying internal voltage-source E_{eq} and resistance Z_{eq} that are functions of the DC current and voltage measurements of the battery array, i and v, respectively. This approximation is reasonable if frequent battery set-point variations are deployed, enabling a pseudo-continuous computation. Several approaches could be used: we propose to use a simple TTC-model as the one presented in [102] shown in Figure 4.14. This is

$$E_{eq}[k] = E[k] - v_1[k-1]e^{\frac{-\Delta t}{\tau_1[k]}} - v_2[k-1]e^{\frac{-\Delta t}{\tau_2[k]}}, \tag{4.49}$$

$$Z_{eq}[k] = R_0[k] + R_1[k]\left(1 - e^{\frac{-\Delta t}{\tau_1[k]}}\right) + R_2[k]\left(1 - e^{\frac{-\Delta t}{\tau_2[k]}}\right), \tag{4.50}$$

with τ_1 and τ_2 known time-constants that are dependant on the SoC (but fix at each time-step).

Then, in general, the DC power of the battery bank, p, can be computed as a function of

[3]For storage systems for which this hypothesis does not hold, there is the need to adopt the complete model whose parameters are SoC-dependent.

the terminals voltage v using

$$p(v) = \frac{(E_{eq} - v)v}{Z_{eq}}. \tag{4.51}$$

It is important to note that this function is maximized at $v = E_{eq}/2$.

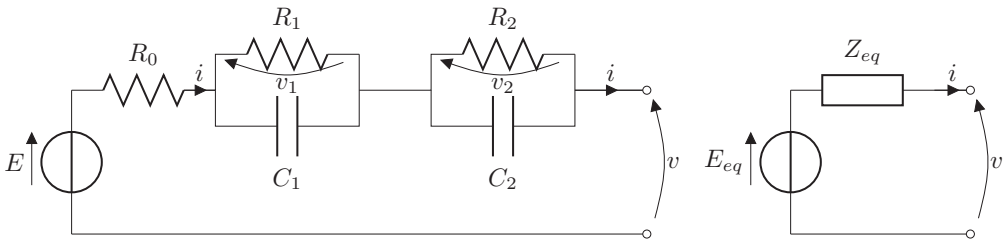

Figure 4.14 – Full battery model and equivalent battery model.

4.10.2 Battery Agent

Implementation of Set-Points. Following the assumption that the state-of-charge of the battery bank is constant from the actual time-step to the following one, the set-point implementation is restricted to the PQ profile that will be sent to the GA. This is covered in the next section.

PQ **Profile**. Considering the limitations on the magnitudes of v and i given by the storage specifications (v_{min}, v_{max} and i_{max}) and the equivalent model, the agent computes the DC power bounds for the resource as

$$p_{max} = p(\max\{v_{min}, E_{eq} - Z_{eq} i_{max}, E_{eq}/2\}), \tag{4.52}$$
$$p_{min} = p(\min\{v_{max}, E_{eq} + Z_{eq} i_{max}\}). \tag{4.53}$$

Finally, this range (translated to the AC-side as for Observation of Section 4.1) is intersected with the circle defined by the power converter rated power S_r.

Belief Function. As storage devices are highly controllable, we assume an ideal belief, namely, $\mathcal{B}(P, Q) = \{(P, Q)\}$ for any $(P, Q) \in \mathcal{A}$.

In Figure 4.15a we show an example of the PQ profile and belief function produced by the agent

Virtual Cost. The role of the virtual cost function is to measure the tendency of the storage agent to stay within particular zones of the PQ profile. For a possible goal, we consider that the main variable of interest for a storage system is its state of charge. In this case, the battery agent tends to steer the SoC to a certain target value that represents

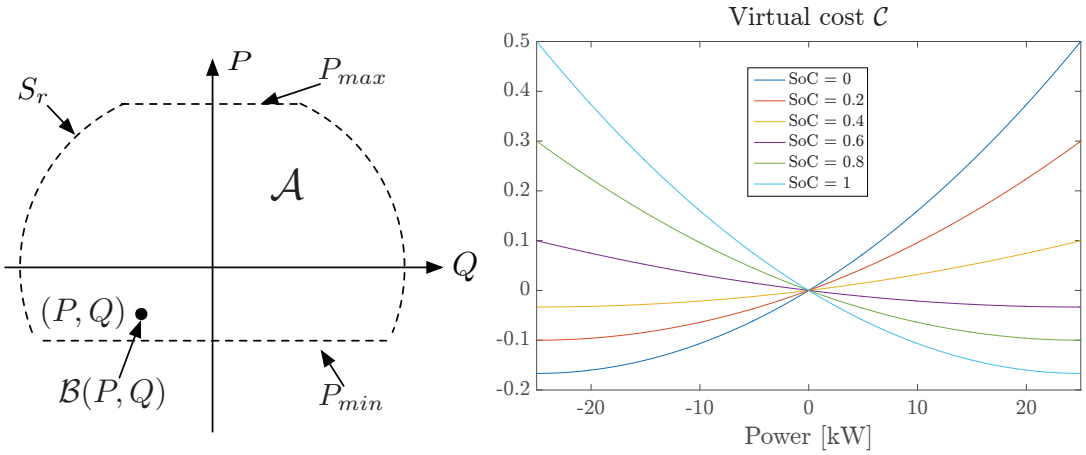

(a) PQ profile and belief function.

(b) Virtual cost for $\text{SoC}_T = 0.5$.

Figure 4.15 – Complete advertisement produced by the battery agent.

a suitable (admissible) internal state of the storage obtained from a long-term scheduler[4]. Therefore, if the current SoC is larger than a target value, the battery prefers to be discharged, hencethe agent advertises a negative cost for discharging (positive P) and a positive cost for charging (negative P). This situation is reversed for the case when the SoC is lower than the target value. If the SoC is equal to the target, the cost will become zero, as the agent is indifferent to the power injection. We assume that the current SoC is measured by the resource using the computation presented in [103].

As an example, the following polynomial function can be used

$$\mathcal{C}(P,Q) = \frac{\Delta\text{SoC}}{3}\left(\frac{\text{sgn}(\Delta\text{SoC})P^2}{S_r^2} - \frac{2P}{S_r}\right), \tag{4.54}$$

where $\Delta\text{SoC} = \text{SoC} - \text{SoC}_T$, SoC_T is the target SoC. This function is chosen so that it presents (i) a positive *cost* when going in the opposite direction of the target SoC, and a negative cost (incentive) when heading towards the target; and (ii) a higher *price* ($\partial\mathcal{C}/\partial P$ that is, the derivative of the cost) for a higher power at constant SoC. It has been also normalized to the range $[-1, 1]$. An illustration of this function is shown in Figure 4.15b for different values of SoC. For example, when $\Delta\text{SoC} > 0$, the cost for charging is positive with a steep slope and the cost for discharging is negative with gentle slope varying with asked power. It should be noted that the cost for reactive power for energy storage systems is considered to be zero.

[4]For electrochemical storage systems, this scheduler might take into account their state-of-health and consequent life-time.

4.11 Supercapacitor Bank

For storage systems characterized by relatively high-energy densities (e.g., batteries), the update rate of the resource set-point imposed by the COMMELEC framework (around 100[ms]) is small enough so that the state of charge can normally be considered constant between two consecutive set-points. In contrast, for a supercapacitors array, this assumption is no longer true. In contrast with battery energy-storage systems, supercapacitors are characterized by a higher power-density and a smaller energy-density [104]. Therefore, the operation capabilities of a supercapacitors array for 100[ms] in the future, will strongly depend on the last implemented power set-points.

As a result, a supercapacitor agent (SCA) must have an accurate model in order to assess the electrical state of its resource. For this purpose, we rely on the supercapacitor-cell model presented in [105], where the redistribution of residual charge phenomena is taken into account. A brief description of the model is given in the next section in order to provide the elements needed for the SCA definition.

4.11.1 Supercapacitor-Cell Model

Figure 4.16 shows the model of a supercapacitor cell [105].

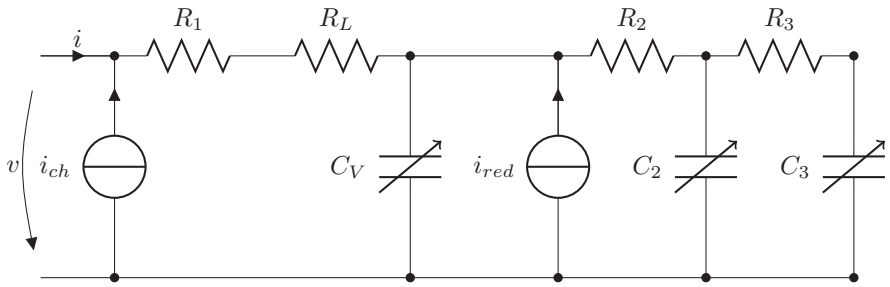

Figure 4.16 – Adopted supercapacitor model.

The peculiarity of this model is that it is capable of representing the so-called redistribution of the residual charge taking place in each supercapacitor cell of the array. The residual charge (Q_R) is the amount of charge that remains stored in the cell after a discharge that results in a terminals' voltage (v) achieved at the end of the discharge [105]. The modeling of Q_R redistribution is accounted for by two current sources i_{ch} and i_{red} in the supercapacitor equivalent circuit in Figure 4.16. Note that i_{ch} is only active when the cell is in operation, i.e., $i > 0$ (charging) or $i < 0$ (discharging), and i_{red} is inactive. Whereas, i_{red} is active when $i = 0$ and i_{ch} is inactive. The supercapacitor cell can then be represented as a system of six state variables

$$\mathbf{x} = (v_{C_V}, v_{C_2}, v_{C_3}, i_{ch}, i_{red}, \dot{i_{red}}), \tag{4.55}$$

where v_{C_V}, v_{C_2} and v_{C_3} are the internal capacitors voltages and, i_{ch} and i_{red} the current magnitude of the current sources.

The system can be defined as a linear control ODE problem where $\mathbf{x}$ is the state, i is the input and v is the output.

$$\dot{\mathbf{x}} = \mathbf{A}\mathbf{x} + \mathbf{B}i \tag{4.56}$$

$$v = \mathbf{C}\mathbf{x} + Di \tag{4.57}$$

$$\mathbf{x}(t_0) = \mathbf{x}_0 \tag{4.58}$$

For the implementation of the SCA, we consider the following assumptions:

- There is access to the instantaneous measurement of v and i. With these measurements available and given initial conditions, we can compute the state of the model at any time-step.
- The parameters of the model are known by means of the process described in [105].
- The supercapacitors array is composed of identical cells connected in series so that we can directly aggregate them. Therefore, the status of a cell inherently identifies that of the entire array[5].

Model Equivalence

We present in this section how to derive Equations (4.56) and (4.57) according to the cell model. As previously mentioned, the current sources in the model of Figure 4.16 are active or inactive, depending upon the current magnitude i. Indeed, when $i = 0$ only i_{red} is active and when $i \neq 0$ only i_{ch} is. We differentiate these two cases as *redistribution mode* and *charging/discharging mode*, respectively. For both cases, $\mathbf{A}$ can be expressed as:

$$\mathbf{A} = \begin{pmatrix} \mathbf{A}_{11} & \mathbf{A}_{12} & \\ \mathbf{0}_{3\text{x}3} & A_{ch} & \mathbf{0}_{1\text{x}2} \\ & \mathbf{0}_{2\text{x}1} & \mathbf{A}_{red} \end{pmatrix}$$

For both cases, $\mathbf{A}_{11}$ can be defined as

$$\mathbf{A}_{11} = \begin{pmatrix} \frac{-1}{C_V R_2} & \frac{1}{C_V R_2} & 0 \\ \frac{1}{C_2 R_2} & -\left(\frac{1}{C_2 R_2} + \frac{1}{C_2 R_3}\right) & \frac{1}{C_2 R_3} \\ 0 & \frac{1}{C_3 R_3} & -\frac{1}{C_3 R_3} \end{pmatrix}$$

[5]Note that the distribution of charge among cells is out of the scope of the model used.

For the redistribution mode ($i = 0$)

$$\mathbf{A}_{12} = \begin{pmatrix} 0 & \frac{1}{C_V} & 0 \\ 0 & 0 & 0 \\ 0 & 0 & 0 \end{pmatrix}, \mathbf{A}_{red} = \begin{pmatrix} 0 & 1 \\ -\frac{1}{\tau_2 \tau_3} & -\left(\frac{1}{\tau_2} + \frac{1}{\tau_3}\right) \end{pmatrix}$$

$$\mathbf{C} = \begin{pmatrix} 1 & 0 & 0 & 0 & 0 & 0 \end{pmatrix}$$

A_{ch}, $\mathbf{B}$ and D can be defined as zero.

For the charging/discharging mode ($i \neq 0$):

$$\mathbf{A}_{12} = \begin{pmatrix} \frac{1}{C_V} & 0 & 0 \\ 0 & 0 & 0 \\ 0 & 0 & 0 \end{pmatrix}, \mathbf{B}^T = \begin{pmatrix} \frac{1}{C_V} & 0 & 0 & 0 & 0 & 0 \end{pmatrix}$$

$$A_{ch} = -\frac{1}{\tau}, \quad \mathbf{C} = \begin{pmatrix} 1 & 0 & 0 & R_1 + R_L & 0 & 0 \end{pmatrix}$$
$$D = R_1 + R_L$$

$\mathbf{A}_{red}$ can be defined as zero. The parameters τ, τ_1 and τ_2 are the time constants of the two current sources.

Initial Conditions

Given the duality of the problem, new initial conditions for the state variables i_{ch}, i_{red} and $\dot{i_{red}}$ have to be computed on each mode transition. In [105] the details for computing these values are discussed. Here we present the useful results for our formulation.

For the transition to the redistribution mode

$$i_{red}(0) = \left(\frac{\eta_2}{\tau_2} + \frac{\eta_3}{\tau_3}\right) \Delta Q_4, \quad \dot{i_{red}}(0) = -\left(\frac{\eta_2}{\tau_2^2} + \frac{\eta_3}{\tau_3^2}\right) \Delta Q_4, \tag{4.59}$$

where η_2 and η_3 are parameters of the model and ΔQ_4 is the quota of charge contributing to the redistribution phase due to the diffusion phenomena. This is the effective charge that will be redistributed in the cell during this phase. It is important to note that this charge is the result of the difference between the available charge for redistribution at the beginning of the last charging/discharging phase (ΔQ) and the charge that was indeed redistributed (ΔQ_1) and the amount of residual charge that the cell would have in case it stays in open-circuit conditions (ΔQ_2), i.e., $\Delta Q_4 = \Delta Q - \Delta Q_1 - \Delta Q_2$. We define ΔQ_3

as the charge that is effectively redistributed during this phase, i.e., the integral of i_{red}:

$$\Delta Q_3 = \eta_2 \Delta Q_4 \left(1 - e^{-\frac{t}{\tau_2}}\right) + \eta_3 \Delta Q_4 \left(1 - e^{-\frac{t}{\tau_3}}\right). \tag{4.60}$$

For the transition to the charging/discharging mode

$$i_{ch}(0) = \frac{\Delta Q}{\tau}, \tag{4.61}$$

where $\Delta Q = \Delta Q_4 - \Delta Q_3 + \Delta Q_2$. As mentioned before, ΔQ_1 is the charge that was redistributed during the charging/discharging mode, i.e., the integral of i_{ch}:

$$\Delta Q_1 = \Delta Q \left(1 - e^{-\frac{t}{\tau}}\right). \tag{4.62}$$

The initial conditions for all other state variables are simply taken as the state in the previous step.

4.11.2 The SCA Problem

The supercapacitors array has operational limits in terms of voltage and current magnitudes: $v_{max} > 0, v_{min} > 0, i_{max} > 0$ and $i_{min} < 0$. In practice the current limits will be mostly defined by the DC-DC stage of the power converter interface.

Observation. *For the cell model presented in Figure 4.16, both the voltage and the current are monotonic with respect to the power.*

In Figure 4.17, we present a numerical validation of the property applied to the cited model where the values are computed for one cell from reference [105]. Each curve represents the evolution of v and i, with respect to p for different initial conditions. The power range of each curve is defined by the operational limits of the cell.

The SCA problem is to compute, at time t_0, the set of all DC-side power set-points $p = p_{t_1 \to t_2}$ that are **feasible**, i.e., for which v and i are inside their operational constraints during the whole interval $[t_1, t_2]$. It follows that, given the mononicity observation, the set of feasible DC-power set-points is an interval, and it is sufficient to compute the

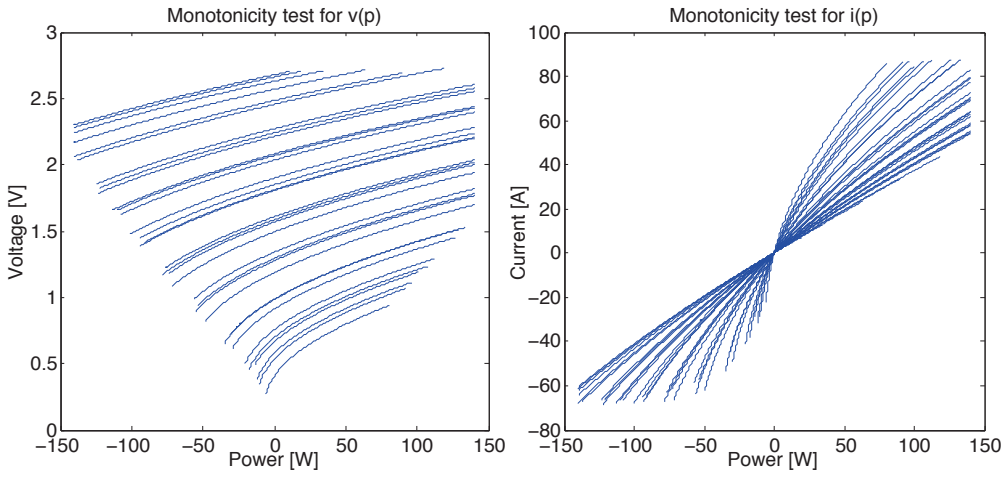

Figure 4.17 – Results of the computation of $v(p)$ and $i(p)$ for different initial conditions.

maximum and minimum DC-powers p_{min} and p_{max}. The SCA problem at t_0 is therefore

$$\begin{array}{ll} \text{minimize (resp. maximize)} & p_{t_1 \to t_2} \\ \text{subject to} & p(t) = v(t)i(t) \\ & v_{min} \leq v(t) \leq v_{max} \\ & i_{min} \leq i(t) \leq i_{max} \\ & \text{Eqs. (4.56) , (4.57) and (4.58)} \\ & \text{for } t \in [t_1, t_2] \end{array} \tag{4.63}$$

4.11.3 Solution of the SCA Problem

First recall that the power p is kept fixed for the considered time-window. We can develop Equation (4.57) to compute v as a function of p, when $i \neq 0$:

$$\begin{aligned} v &= \mathbf{Cx} + D\frac{p}{v} \\ v^2 &- \mathbf{Cx}v - Dp = 0 \\ v &= \frac{\mathbf{Cx} \pm \sqrt{(\mathbf{Cx})^2 + 4Dp}}{2}. \end{aligned} \tag{4.64}$$

Assuming that v is always between bounds, it is always positive $v > 0$. Then, the only valid solution of Equation (4.64) when $p > 0$ is the one linked to the positive sign, since $D > 0$ (see Section 4.11.1). Note that the argument of the square root is negative for

$$p < p_c = -\frac{(\mathbf{Cx}(t_2))^2}{4D}. \tag{4.65}$$

Therefore, the correct operation of the supercapacitors array requires $p \geq p_c + \delta$, where δ is a safety margin suitably defined. The physical meaning of this power is the following: For values lower than p_c, the electrical state of the array is so deteriorated that no actual power can be provided by the device. As a consequence the solution with the negative sign in Equation (4.64) can be never reached by continuity argument, i.e., we always use the positive sign also when $p < 0$. Applying this to Equation (4.56) the non-linear ODE problem to be solved is

$$\begin{aligned}
\dot{\mathbf{x}} &= \mathbf{A}\mathbf{x} + \mathbf{B}i \\
&= \mathbf{A}\mathbf{x} + \frac{\mathbf{B}}{D}(v - \mathbf{C}\mathbf{x}) \\
&= \left(\mathbf{A} - \frac{\mathbf{B}\mathbf{C}}{D}\right)\mathbf{x} + \frac{\mathbf{B}}{D}v \\
&= \left(\mathbf{A} - \frac{\mathbf{B}\mathbf{C}}{D}\right)\mathbf{x} + \frac{\mathbf{B}}{D}\left(\frac{\mathbf{C}\mathbf{x} + \sqrt{(\mathbf{C}\mathbf{x})^2 + 4Dp}}{2}\right) \\
\dot{\mathbf{x}} &= \left(\mathbf{A} - \frac{\mathbf{B}\mathbf{C}}{2D}\right)\mathbf{x} + \frac{\mathbf{B}}{2D}\sqrt{(\mathbf{C}\mathbf{x})^2 + 4Dp},
\end{aligned} \tag{4.66}$$

whose solution is only obtained through numerical methods assuming a given value on the input p.

In the specific case when $p = 0$, $i = 0$ and we can directly solve Equation (4.56):

$$\begin{aligned}
\mathbf{x} &= e^{\mathbf{A}t}\mathbf{x_0} \\
v &= \mathbf{C}e^{\mathbf{A}t}\mathbf{x_0}
\end{aligned} \tag{4.67}$$

With the computation of the initial conditions $\mathbf{x_0}$ as shown in Section 4.11.1.

We now present how to compute the DC power bounds for the period $t_1 \to t_2$ at time t_0. Recall that from the viewpoint of the resource, $p > 0$ represents charging and $p < 0$ discharging.

1. For any time t_1, update the state $\mathbf{x}(t_1) = \mathbf{x_0}$ as previously shown[6].
2. Use Equation (4.67) in the window $[t_1, t_2]$, with the purpose of verifying that the redistribution of charges does not violate the voltage limits. Store the value $v_{test} = v(t_2)|_{p=0}$[7].
3. **Computation of p_{max}:** first, note that in a charging phase when $p > 0$, v always increases as for the monotonicity observation. As p is constant during this phase, the

[6] This step can be further improved by taking into account the current measurement of v and i in the computation of $\mathbf{x_0}$.

[7] For example, if the redistribution phase causes the voltage to increase and violate v_{max}, p_{max} will be negative (i.e., the array should be discharged).

maximum magnitude of i is reached exactly at the beginning of the new operation window. Hence, the corresponding power that will attain this condition is given by

$$p^i_{max} = \mathbf{Cx}(t_1) i_{max} + D i^2_{max}. \tag{4.68}$$

Then, by performing a binary search, we look for the value of p that gives $v(t_2) = v_{max}$. This power is named p^v_{max}. If $v_{test} > v_{max}$, we perform the search in the range $[v_{max} i_{min}, 0]$, otherwise in $[0, v_{max} i_{max}]$.

We finally compute $p_{max} = \min(p^i_{max}, p^v_{max})$.

4. **Computation of p_{min}:** as for p_{max}, we perform a binary search for the value of p such that it reaches

$$i = \max\left(i_{min}, \frac{v_{min} - \mathbf{Cx}(t_2)}{D}\right). \tag{4.69}$$

If $v_{test} < v_{min}$ the search is done in the positive range $[0, v_{max} i_{max}]$, otherwise in the negative one $[\max(p_c, v_{max} i_{min}), 0]$.

4.11.4 SCA Advertisement

Implementation of Set-Points. We apply the previously presented procedure in order for computing p_{min} and p_{max} and check whether the request is between bounds, otherwise we set the closest computed constraint.

PQ **Profile.** After knowing the implemented set-point, using the model we can estimate the state of the supercapacitors array at the end of the period. Similarly, we use the same procedure to compute the DC power limits and suitably transfer them to the AC terminal through the power converter. The power limits on the AC side are called P_{min} and P_{max}[8]. As for the battery, we can define the *PQ* Profile as

$$\mathcal{A} = \{(P, Q) : P \in [P_{min}, P_{max}], \sqrt{P^2 + Q^2} \leq S_r\}. \tag{4.70}$$

Belief Function. Considering that the supercapacitors array is connected through a power converter to the grid, we assume that it is *fully controllable*, i.e., it can follow exactly the requested power. This means that we can define

$$\mathcal{B}(P, Q) = \{(P, Q)\}. \tag{4.71}$$

Virtual Cost. We define $\mathcal{C}$, as a function of the current state-of-charge (SoC), hence only depending on the active power P. As in the battery agent, we assume that there is a desirable or target value (SoC_T) defined externally (e.g., system-wise with a long-term

[8]Note that in the AC side, $P > 0$ is for discharging.

optimizer). Therefore, we set a higher cost for powers that make ΔSoC = SoC - SoC$_T$ larger. A suitable quadratic function is desirable for providing convexity.

We consider that the SoC is computed as the ratio between the charge stored in all the capacitors of the model (C_V, C_2 and C_3) and the nominal capacity[9]:

$$Q_n = (C_V + C_2 + C_3)(v_{max} - v_{min}). \tag{4.72}$$

Then we can compute

$$\text{SoC} = \frac{1}{Q_n}\left(C_V v_{C_V} + C_2 v_{C_2} + C_3 v_{C_3} + Q_R\right) \tag{4.73}$$

$$Q_R = \begin{cases} \Delta Q_1 & \text{if } i \neq 0 \\ \Delta Q_3 & \text{if } i = 0 \end{cases} \tag{4.74}$$

Hence, the cost function that we adopt is the same as the one of the battery agent.

$$\mathcal{C}(P, Q) = \frac{\Delta\text{SoC}}{3}\left(\frac{\text{sgn}(\Delta\text{SoC})P^2}{S_r^2} - \frac{2P}{S_r}\right), \tag{4.75}$$

[9] Q_n represents the effective charge that the supercapacitors array can store because it cannot be operated until $v = 0$, as the DC voltage is bounded by the power electronics interface.

5 Validation of the Framework via Simulations

Chapter Highlights:

In this chapter, we evaluate the performance of the COMMELEC control framework. This assessment is done by using a suitably developed simulation environment. We consider a case study that makes reference to the low-voltage microgrid benchmark defined by the CIGRÉ Task Force C6.04.02. The microgrid is connected to a generic medium-voltage feeder that contains the minimum number of elements that enable us to show the applicability and potentials of the proposed control framework.
In this system, we test the base features of the framework together with the performance at steering the islanding maneuver.

In order to test and validate the behavior of the COMMELEC framework, a generic event-driven simulation environment was implemented in Matlab ®.

We defined a case study whose conditions enable us to show the operation of the framework for both a grid-tie microgrid and an islanded network.

The system exhibits the following general characteristics:

(i) It is composed of the two lowest levels of a power network: low and medium voltage.

(ii) The slack bus is located at the medium voltage level and is provided by the largest storage system.

(iii) Energy storage is distributed in both low and medium voltage.

(iv) Thermal loads (water boilers) are used as virtual storage.

(v) The randomness comes from the absorption patterns of the loads and the solar irradiation. For the latter, we used a high time-resolution profile (sampled each 50[ms]) obtained from real measurements, performed on the EPFL campus.

A challenge in such a system is that most of the physical energy-inertia comes from storage and thermal loads, rather than from rotating machines. This condition matches the goal of the proposed real-time control strategy, i.e., to overcome this difficulty in the presence of extremely volatile resources (e.g., PVs).

In order to assess its performance, the following metrics are used: the distances of node voltages and line currents to their operational limits, the state of charge of electric-storage and thermal-storage devices, the proportion of curtailed renewables, and the robustness against system collapse in case of overproduction from renewables.

The framework is compared to two classic methods that rely on droop control: the first only with *primary control* on both frequency and voltage, and the second with an additional *secondary frequency control* at the slack device (see, e.g., [9]).

5.1 Case Study

In this section, we present a case study where the proposed control framework is implemented. To show its applicability, we selected a closed system that contains several types of agents.

5.1.1 System Details

We consider a $0.4[kV]$ LV network that includes

(i) distributed generation composed of photovoltaic plants (PVi) and a hydraulic microturbine (μH),

(ii) a storage system represented by a battery (ESS_1),

(iii) uncontrollable loads (ULi) and

(iv) controllable loads (WBi) modelled as water boilers, all capable of deploying explicit control setpoints.

The topology and parameters of this LV grid are taken from [106]. As typically used in a microgrid (MG) setup, we assume that all the generation/storage units connected to the LV MG are interfaced with the grid through power-electronic devices [37].

To show the interaction between different grids, the MG is connected to a 20[kV] MV distribution system that interconnects

(i) a large battery-storage system (ESS),

(ii) a combined heat and power generator, interfaced with the MV grid by means of a synchronous generator (SG) and

(iii) an industrial uncontrollable load (UL).

The corresponding electrical diagram for the case study is presented in Figure 5.1a.

To illustrate the mapping between physical subsystems and agents, we consider the hierarchical agents setting shown in Figure 5.1b where the microgrid agent (LVGA) is in charge of the resources in the LV network, whereas the medium-voltage grid agent (MVGA) is in charge of those in the MV network and the LVGA. According to the framework definition made in Chapter 3, the LVGA acts as a grid-connected GA, and the MVGA is an islanded GA.

The line parameters used for the network are presented in the Table 5.1.

Table 5.1 – Electrical parameters of the lines composing the MV and LV lines

Type	MV1	LV1	LV2	LV3	LV4	LV5	LV6
Resistance $[\Omega/km]$	3.938	0.284	0.497	3.690	1.380	0.871	0.822
Reactance $[\Omega/km]$	1.969	0.083	0.086	0.094	0.082	0.081	0.077
Susceptance $[\mu S/km]$	2.780	0	0	0	0	0	0
Ampacity $[A]$	25	170	120	31	60	73	140

We use the base system and the voltage bounds and the parameters of the MV/LV transformer shown in Table 5.2. We use a conventional transformer-model as in [95].

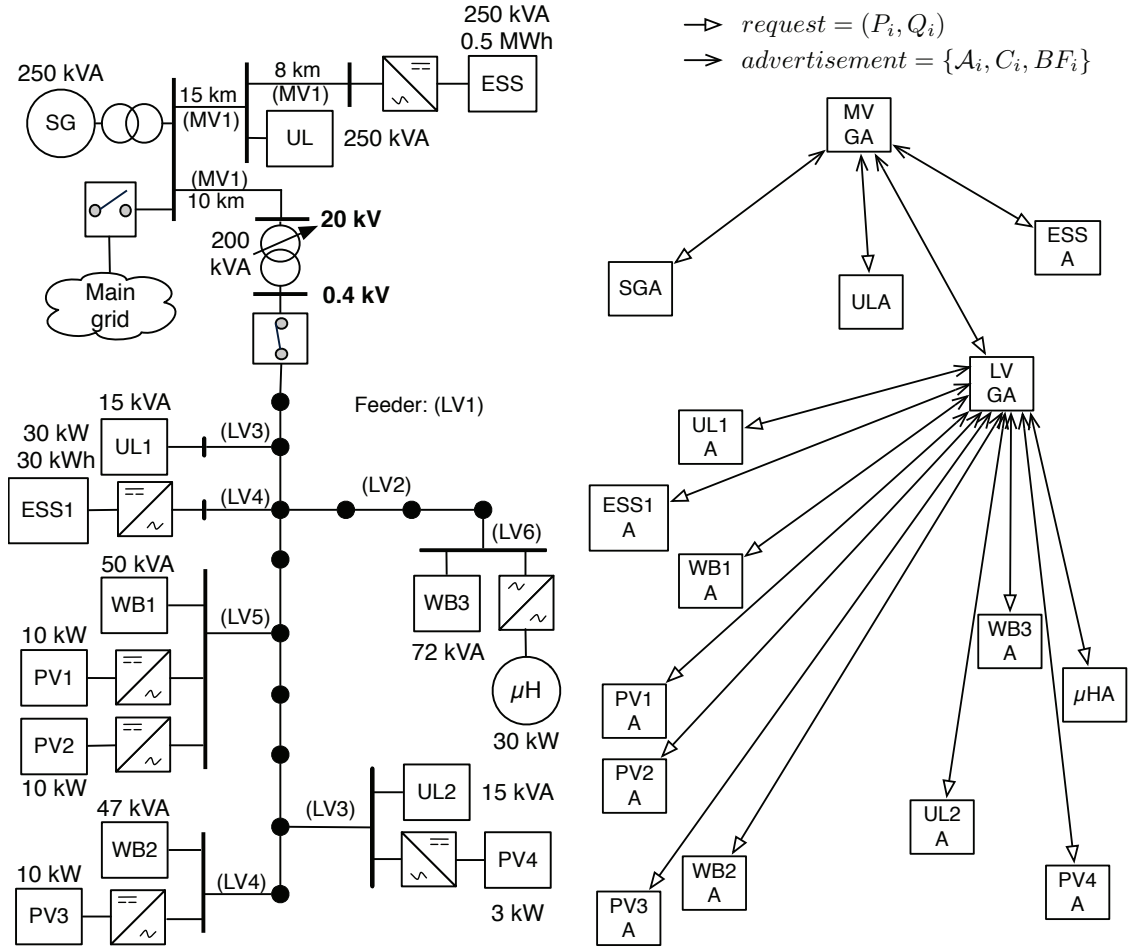

Figure 5.1 – The electrical network and agents for the this case study. (a) Microgrid. (b) Agents.

Table 5.2 – System and transformer parameters

MV base	LV base	Base power	V bounds	S_r	V_k	r_k
20	0.4	1	0.9 - 1.1	400	4	1
[kV]	[kV]	[MVA]	[pu]	[kVA]	[%]	[%]

5.1.2 Control Methods

We perform a comparison between the following control methods applied to the case study.

(i) The COMMELEC architecture of Figure 5.2. We show in the following sections how we implement the framework in this case.

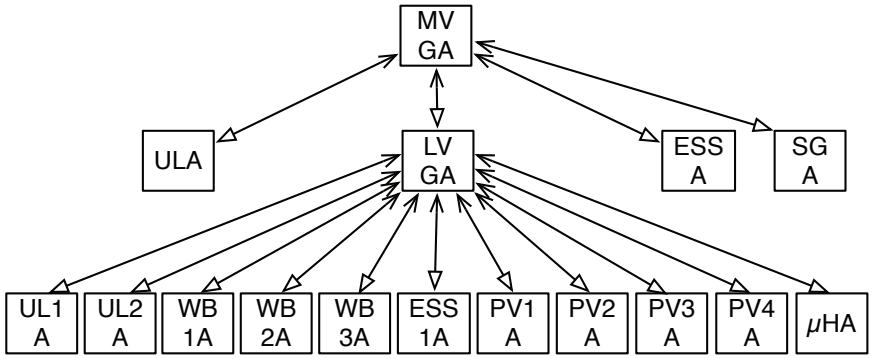

Figure 5.2 – Agents architecture for the case study.

(ii) The droop-control method, with only a *primary control* at each device capable of modifying power set-points (i.e., all with the exception of ULs). In the slack resource, the output frequency is calculated using the conventional droop-control strategy, assuming a null inertia (as it is the case of ESS). This is the signal that will be used for all the other resources to compute their power production. As a result, the frequency is given by

$$f = f_0 - m_f(P - P_0), \tag{5.1}$$

where f_0 is the rated frequency (here 50[Hz]), m_f is the slope, and P_0 is the active power when $f = f_0$. The corresponding frequency and voltage droop-curves in other resources were set to

$$P = P_0 - (f - f_0)/m_f, \tag{5.2}$$
$$Q = Q_0 - (V - V_0)/m_V, \tag{5.3}$$

where V is the measured voltage-magnitude and f is the measured frequency, $V_0 = 1$[pu] is the rated voltage, m_V is the curve slope, and Q_0 is the reactive power when $V = V_0$. It is worth noting that the droop parameters are in general different for each resource. We selected the droop parameters for the resources by using typical values adopted in the literature (e.g. [9]). The selected droop-parameters are shown in Table 5.3.

(iii) The droop-control method as above, with additional *secondary frequency-control* at the slack device, using local frequency-error integrator. In particular, the frequency-droop curve in the slack resource was set to

$$f(t) = f_0 - m_f(P - P_0) + (1/T_i)\int_{t_0}^{t^-}(f_0 - f(\tau))d\tau, \tag{5.4}$$

where $T_i = 50$[s] is the chosen integration constant.

Table 5.3 – Droop parameters

Resource	f_0[Hz]	P_0[pu]	m_f[Hz/pu]	V_0[pu]	Q_0[pu]	m_V[pu]
ESS/ESS$_1$	50	0	-0.5	1	0	-0.04
PV$_i$/WB$_i$	50	0.5	-1	1	0.5	-0.08
SG/μH	50	0.5	-0.8	1	0.5	-0.08

5.1.3 Profiles Data

We chose a simulation scenario for all three control methods (including initial conditions), where we could simulate the case of overall overproduction in the grid from renewables (essentially PV) with minimum load consumption. This scenario is adopted to challenge both control methods to deal with a system characterized by a low margin of controllability. For this purpose, the scenario has the following initial conditions:

1. All batteries are close to their maximum stored-energy capacity. In particular, the initial state of charge (SoC) of both MV and LV battery was set to 0.9.
2. The boilers are undercharged, with initial state of 2.5[kWh].
3. There is a high production from PVs, at a partially sunny day, thus representing high irradiation variability.
4. The loads in the LV grid have zero-consumption profiles, whereas the MV load uses a dynamic profile that represents changes with time resolution of 1 minute.

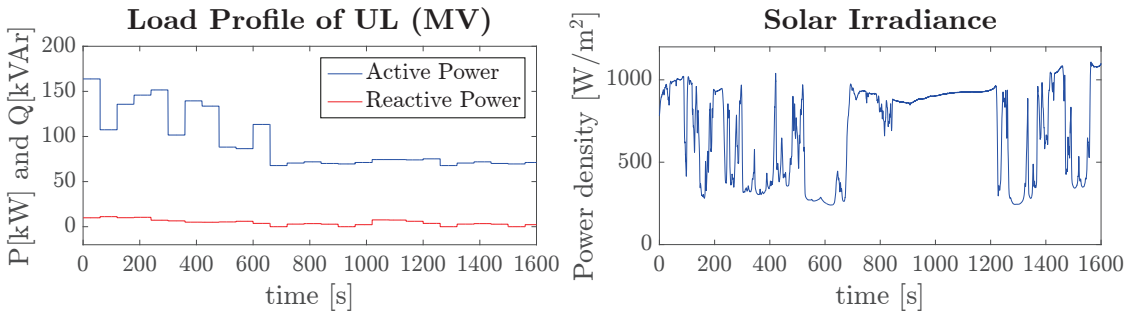

Figure 5.3 – Sources of uncertainty in the case study: UL load profile and solar irradiance.

In this case study, there are two sources of uncertainty: the MV-load (UL) power consumption and the solar irradiance (shown in Figure 5.3). We assume that all the PV plants are exposed to the same irradiance profile. The load consumption is characterized by a dynamic behavior and a low value from minute 11 onwards, whereas the solar-irradiance data is characterized by a highly volatile profile due to the passage of clouds. The irradiance data corresponds to real measurements in Switzerland ($46°31'06.20''N$,

$6°33'54.56''E$) on November the 15^{th}, 2013. The sampling period used to take the data was 50[ms]. The above quantities represent the forcing functions of the targeted case study. Lastly, we use the weights shown in Table 5.4 for the COMMELEC simulations.

Table 5.4 – Simulation parameters

α_{LV}	α_{MV}	ω_{PV_i}, ω_{UL_i} $\omega_{\mu\text{H}}$, ω_{UL}	$\omega_{\text{WB}_{1-3}}$	ω_{WB_2}	ω_{ESS_1}	ω_{ESS}	ω_{SG}	$\omega_{(P_0,Q_0)}$
0.1	5e-5	1	1e-6	1e-8	1e-3	1e-5	0.01	100

5.1.4 Performance Metrics

In order to assess the performance of the control methods, we use the following metrics:

(i) the distances of node voltages and line currents to their limits, representing the quality of supply and the operational margins of the system;

(ii) the state of charge of electric-storage and thermal-storage devices, representing the reserve of the system;

(iii) the proportion of curtailed renewables; and

(iv) the robustness of the method against system collapse.

5.2 Resources

As anticipated, for this validation we consider the following resources:

(i) chemical energy-storage devices (specifically, a *battery*),

(ii) synchronous generator,

(iii) PV generator and

(iv) controllable and uncontrollable loads.

Depending on their nature and/or internal characteristics, these resources have various degrees of controllability, from *fully controllable* resources (e.g., the battery) to *non-controllable* resources (e.g., uncontrollable load).

For the different resources here presented, we use the parameters shown in Table 5.5, the rated powers for each of them can be extracted from Figure 5.1a.

All these resources are associated with a COMMELEC resource agent that follows the design presented in Chapter 4.

Table 5.5 – Resources parameters

Water Boilers		Storage		Synchronous Generators					
$\mathcal{E}^{max}$	$\mathcal{E}^{min}$	η_{ESS}	η_{ESS_1}	P_{min}	P_{max}	X_S	X_T	I_{f_0}	$I_{f_{max}}$
20	1	98	97	0.2	1	0.1	1	1	3.6
[kWh]	[kWh]	[%]	[%]	[pu]	[pu]	[pu]	[pu]	[A]	[A]

5.3 Simulation Results

Below, we present the comparison between the behavior of COMMELEC and the two abovementioned droop-based control strategies; the comparison is followed by the validation of the employed aggregation methods.

5.3.1 Short-Term Behavior

In this section, we compare the results obtained in the scenario described in Section 5.1.3, with three different control methods: COMMELEC, droop with primary frequency and voltage control only in the slack resource (DP), and droop with additional secondary frequency control (DPS) at the slack. The focus here is on the *dynamic short-term behavior*. In particular, the results are presented over the time horizon of 1600[s].

Control of the Reserve of the Storage Systems

The evolution of the state of charge (SoC) of both battery systems (ESS and ESS_1) is shown in Figure 5.4. Note that in the case of COMMELEC, the SoC decreases towards the target value (SoC = 0.5), as opposed to DP/DPS, in both LV and MV networks. In the case of the LV battery, when using COMMELEC, the SoC decreases much faster because this resource is requested to discharge mostly at full power; whereas in the case of the MV battery, it discharges but subject to the fact that this resource is the slack bus of the system (therefore its power production/absorption is the result of all other resources).

The evolution of the SoC of the WBs is also presented in Figure 5.4. It can be seen that the boilers are controlled to react to local power-variations while following their preference to be charged. WB_1 and WB_3 are being charged from the beginning at full power, whereas WB_2 is charged when possible. Whereas, in DP/DPS, they are not charged at all.

Reduced Curtailment of Renewables

Figure 5.5 shows the production of the PVs, by means of the PV active power and the total produced PV energy. It can be seen that in COMMELEC, the PVs produce at

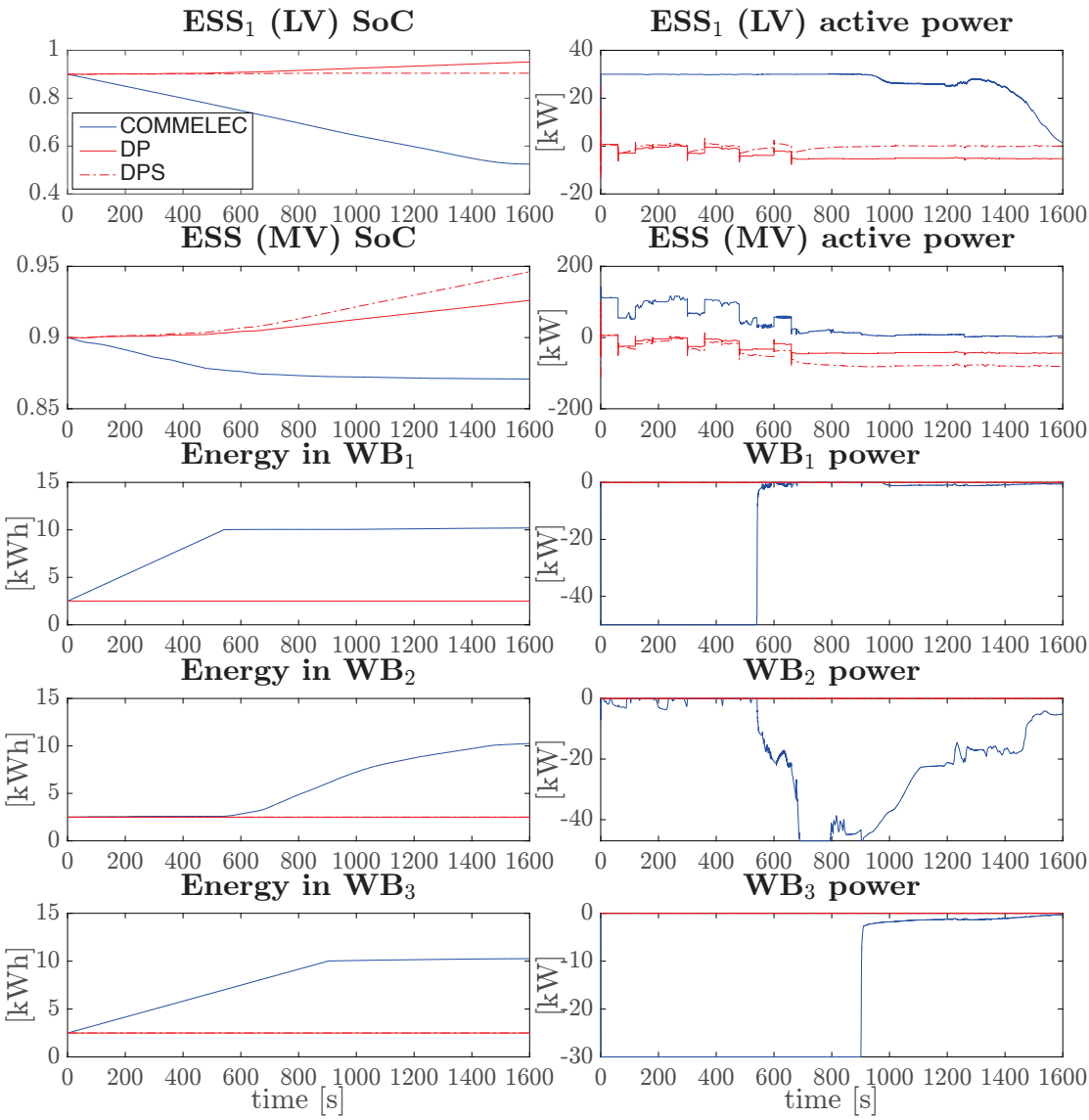

Figure 5.4 – Comparison between COMMELEC and both droop strategies. The left column presents the state-of-charge of the battery systems and the stored energy in the water boilers, while the power profile of the same elements is presented in the right column.

maximum available power most of the time; whereas in DP/DPS they are curtailed, given the excess of power in the network assessed by the frequency signal. In this respect, with COMMELEC the production of renewables is maximized even with high-variability profiles, and it is curtailed only when it affects the power quality or there is not enough storage capacity in the system.

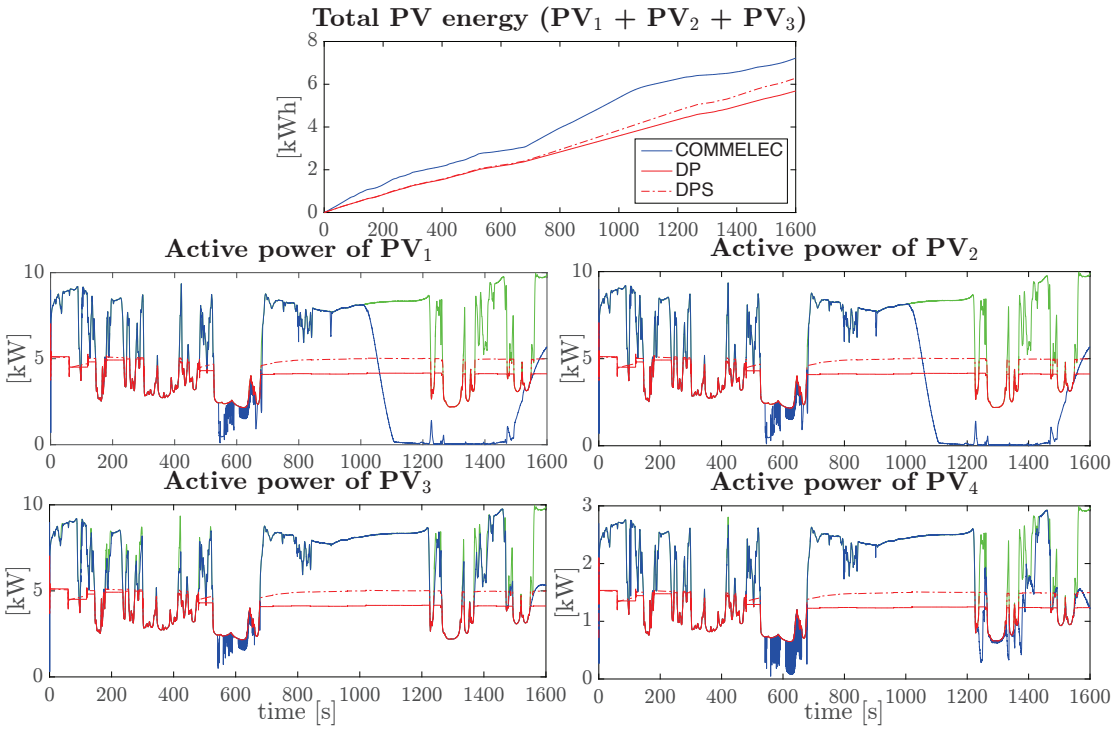

Figure 5.5 – Comparison between COMMELEC and both droop strategies. Total produced energy for the four PV plants connected to the LV microgrid and the power production for each. The dashed green line represents the maximum power production following directly the irradiance profile.

Local Power-Compensations and Exploitation of Degrees of Freedom

Figure 5.6 shows the production of the synchronous generators (SG and μH). It is worth noting that in the case of COMMELEC, the power variations in the LV grid are compensated locally by the means of μH, while maintaining the MV SG at minimum power. In the droop simulation, on the contrary, both machines react in the same way. The main reason for this difference is that COMMELEC exports and uses the internal state of the resources, whereas in DP/DPS the control is performed via the global frequency signal defined by the slack resource.

It is interesting to observe specifically the case of WB_2 that is connected to the same bus with PV_3 (see Figure 5.1). This node is then connected to the main feeder of the LV network by a line with an ampacity close to the current being absorbed by WB_2 at its rated power. We show the dynamic behavior of these two devices in Figure 5.7. It can be seen that WB_2 starts charging around $t = 550$[s]. This becomes possible due to the overall state of the system and, in particular, due to the fact that WB_1 stops charging at this time (see Figure 5.4). However, due to low production from PV_3 at this time and the weakness of the line that connects both devices to the network, the charging is not at the maximum possible power. When the production of PV_3 increases at around $t = 650$[s],

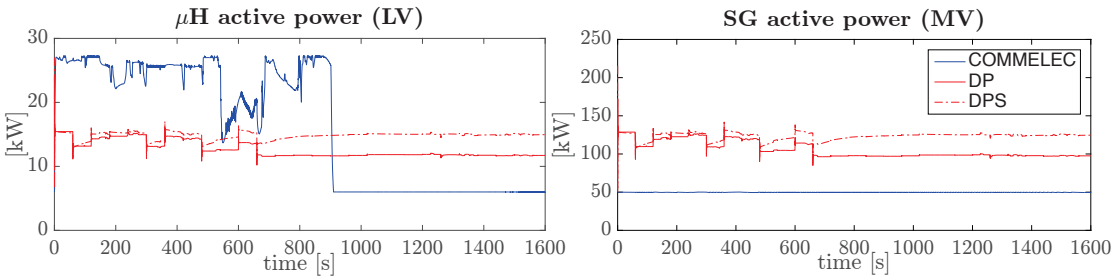

Figure 5.6 – Results for the comparison between COMMELEC and both droop strategies. Active power production of SG and μH.

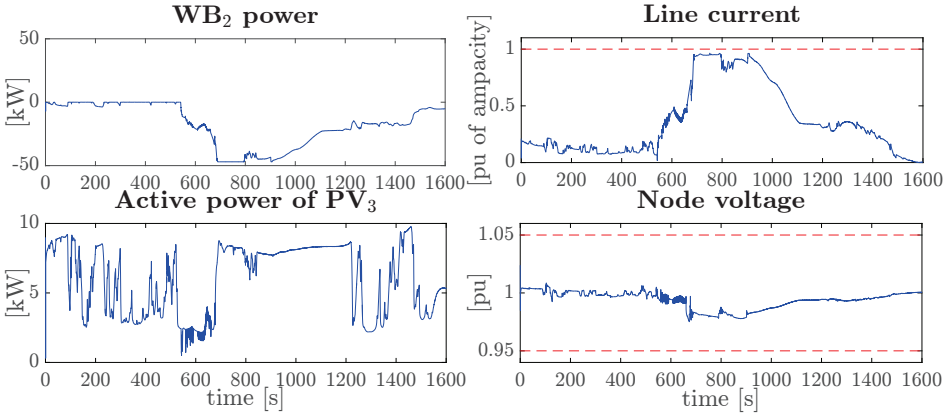

Figure 5.7 – Local power management between WB_2 and PV_3. The left column shows the power profiles while the right column shows the current of the line connected to both resources and the voltage of the common node. The dashed red lines represent the bounds.

WB_2 starts charging at maximum power. We note that the line current remains below the ampacitity during the whole process. This case illustrates again the ability of the framework to compensate for power imbalances locally and to exploit the various degrees of freedom of the system by using the advertised information about the internal state of the devices.

Quality of Service and Stable Frequency

In Figure 5.8, the system frequency is presented. Recall that the slack is the MV storage system (ESS). As the COMMELEC method is explicit, the slack works at a constant frequency by means of an astatic controller.

In the case of DP, on the contrary, the frequency reacts to the changes in UL; and in the case of DPS, it tries to return to the reference value. It is important to note that the frequency variations are highly dependent on the droop parameters and can be very high when there is a sudden change in the network. Therefore, by keeping the frequency

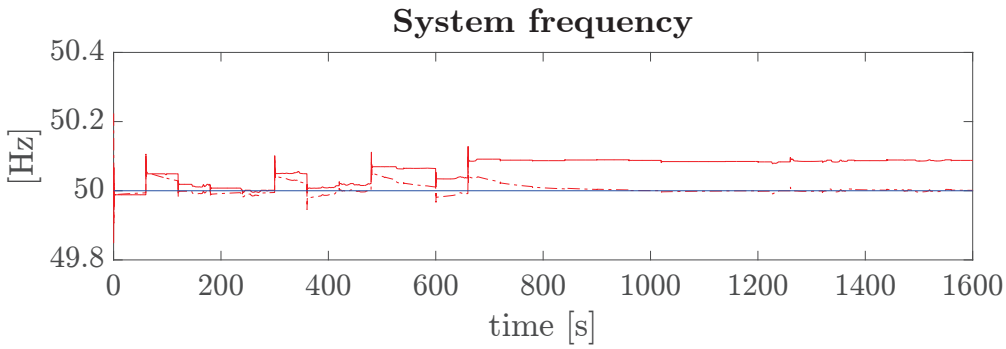

Figure 5.8 – Comparison between COMMELEC and both droop strategies. System frequency.

constant, COMMELEC enables a more accurate control of electrical machines. This is true especially in a microgrid that, when controlled using standard droop-based strategies, is expected to face high variations of frequency due to the uncertainty of the renewables.

In order to analyze the quality of supply of the LV grid, in Figure 5.9 we present the aggregated voltage and current profiles for both networks (i.e., median, minimum and maximum values of node voltages and line currents). It can be seen that the improvement in the overall operation obtained by using the COMMELEC framework does not affect the quality of service. The voltage and current magnitudes are always within the acceptable regions. Note that the maximum LV current using COMMELEC is always close to the ampacity. This specific case is related to WB_2 and PV_3 as explained before. Observe, however, that the median value of the LV current is much lower during the entire simulation run.

5.3.2 Medium-Term Behavior and System Collapse

In this subsection, we illustrate the medium-term system behavior in the critical case corresponding to the overproduction from renewables with initial high value of the SoC of the batteries and minimum load. Specifically, we present the SoC, the production of a PV, and the injection of SG and μH in Figure 5.10, over the time horizon of 4000[s] (around 1 hour). It can be seen that both DP and DPS control strategies lead to the overcharge of the MV battery, essentially causing the *collapse of the system*. In particular, when the power is injected into the ESS with SoC= 1, the local controller of the resource trips its breaker, with the consequent loss of the slack resource that provokes the collapse. The main reason for this behavior is that the droop strategies force the generators to overproduce power regardless of the SoC of the slack resource. It is worth noting that in DP, as there is a permanent positive-frequency error, the LV battery (ESS_1) is always being charged. Hence, it trips even before the MV battery (ESS). The early loss of ESS_1 can be also interpreted as a lack of autonomy of the microgrid if islanded. In the case

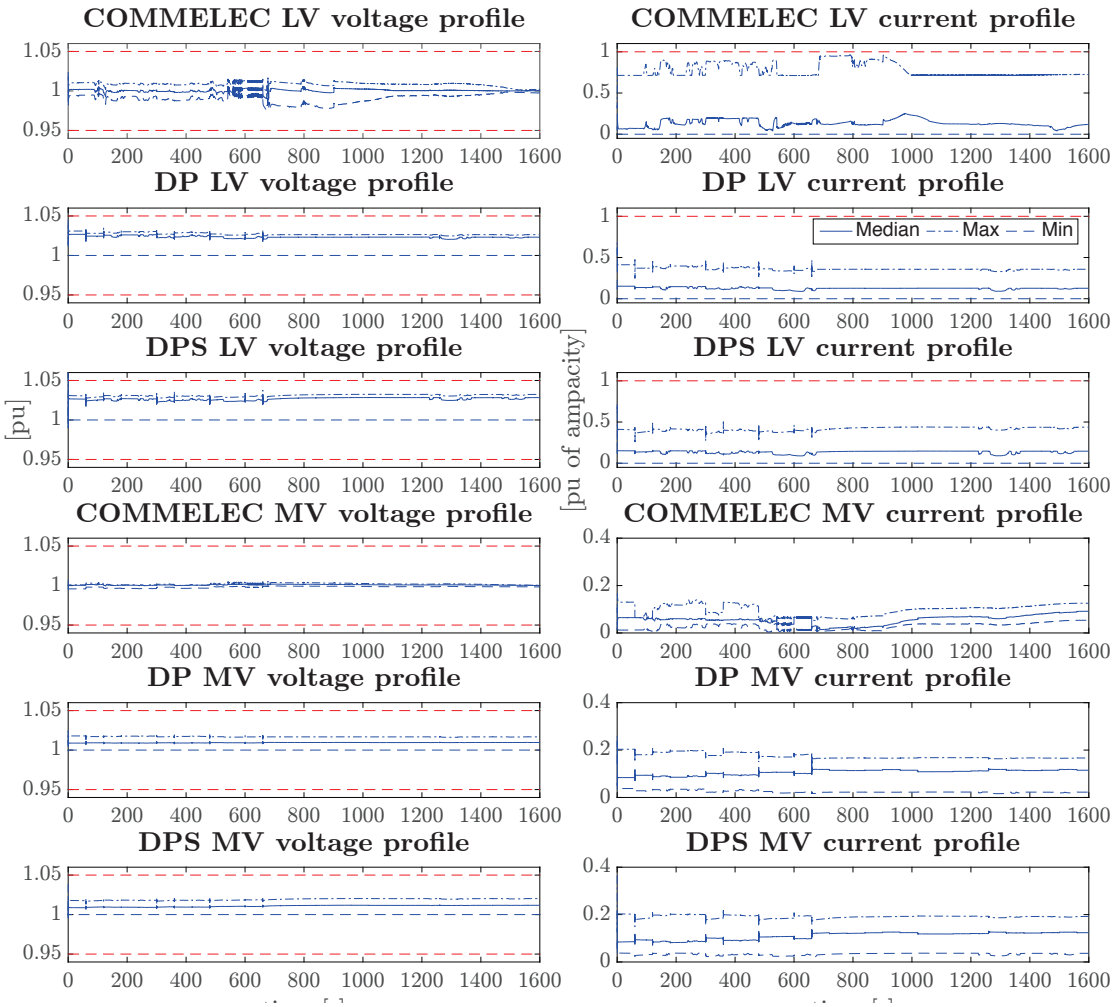

Figure 5.9 – Comparison between COMMELEC and both droop strategies. The red dashed lines represent the predefined bounds for voltage and line congestions.

of DPS, the secondary frequency-control enables a larger production of the generation units, and therefore the SoC of ESS_1 is essentially constant. As a result, the MV battery is charged without an explicit constraint. COMMELEC, on the contrary, keeps the SoC, of both ESS and ESS_1, away from the margins by using internal information from each resource and controlling explicitly their power setpoints.

5.3.3 Unexpected Disconnection of a Device

In this subsection, we demonstrate how COMMELEC is able to cope with an unexpected disconnection of a device. In particular, at $t = 1000$[s] the resource PV_1 and its agent are disconnected. Immediately, the slack resource (ESS) reacts to cope with the imbalance. We recall that, as mentioned above, the control of the slack resource can be astatic. As a consequence, the compensation performed by the slack has no effect on the system

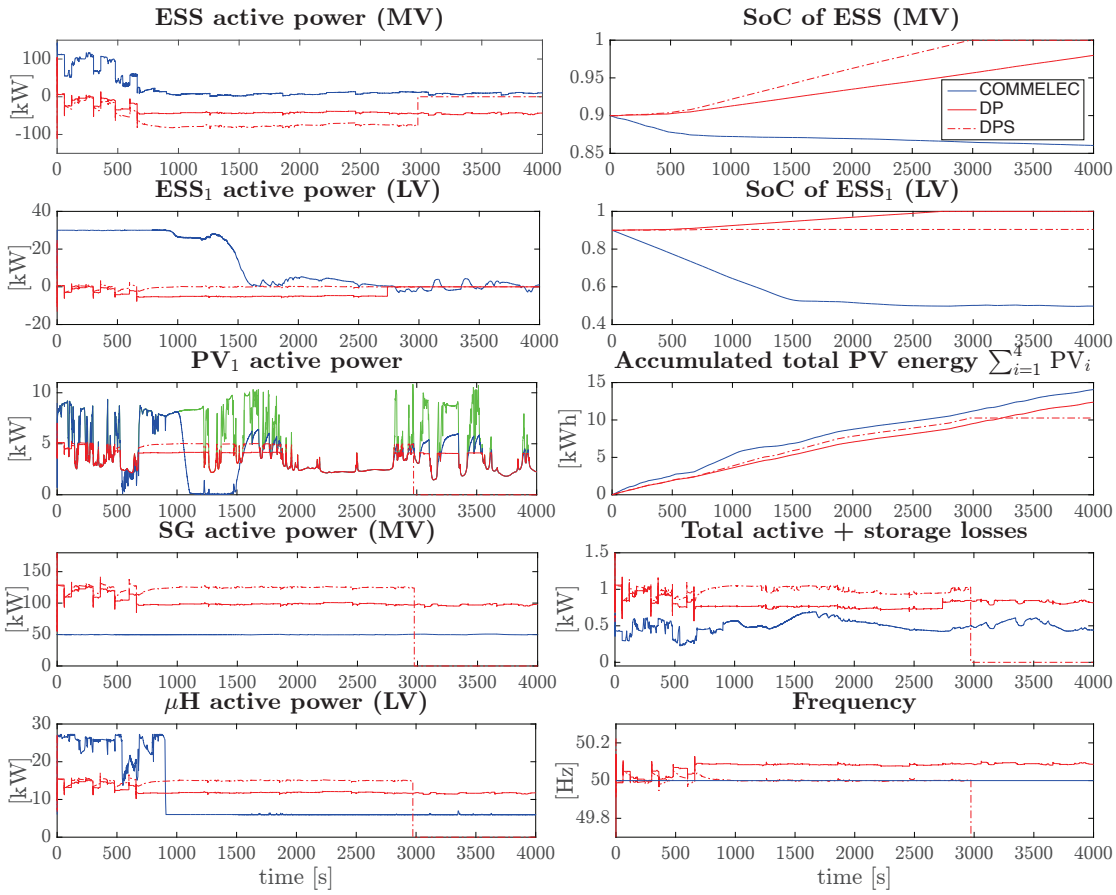

Figure 5.10 – Comparison between COMMELEC and both droop strategies. Medium-term comparison where the batteries are overcharged using DP/DPS strategies due to the production of renewables, even when curtailing their production. A system collapse can be observed for the DPS case from $t \geq 3000$[s].

frequency. Afterwards, COMMELEC takes over. Note that PV_1 is directly connected to WB_1 and PV_2. As WB_1 is already close to its minimum power, and PV_2 aims at producing at maximum, the algorithm also reduces the consumption of WB_2 and WB_3 (connected to different nodes) to assist the event. The simulation shows how COMMELEC handles unexpected disconnection by assisting the slack bus in redistributing the power imbalance between the resources and by keeping the overall state of the grid feasible.

5.3.4 Validation of the Aggregation Methods

In this section, we illustrate the performance of the aggregation method presented in Section 3.4 of Chapter 3. For this part, we use the power profiles for the MV uncontrollable load (UL), the LV uncontrollable loads (UL_1, UL_2), and the solar-irradiance profile shown in Figure 5.12.

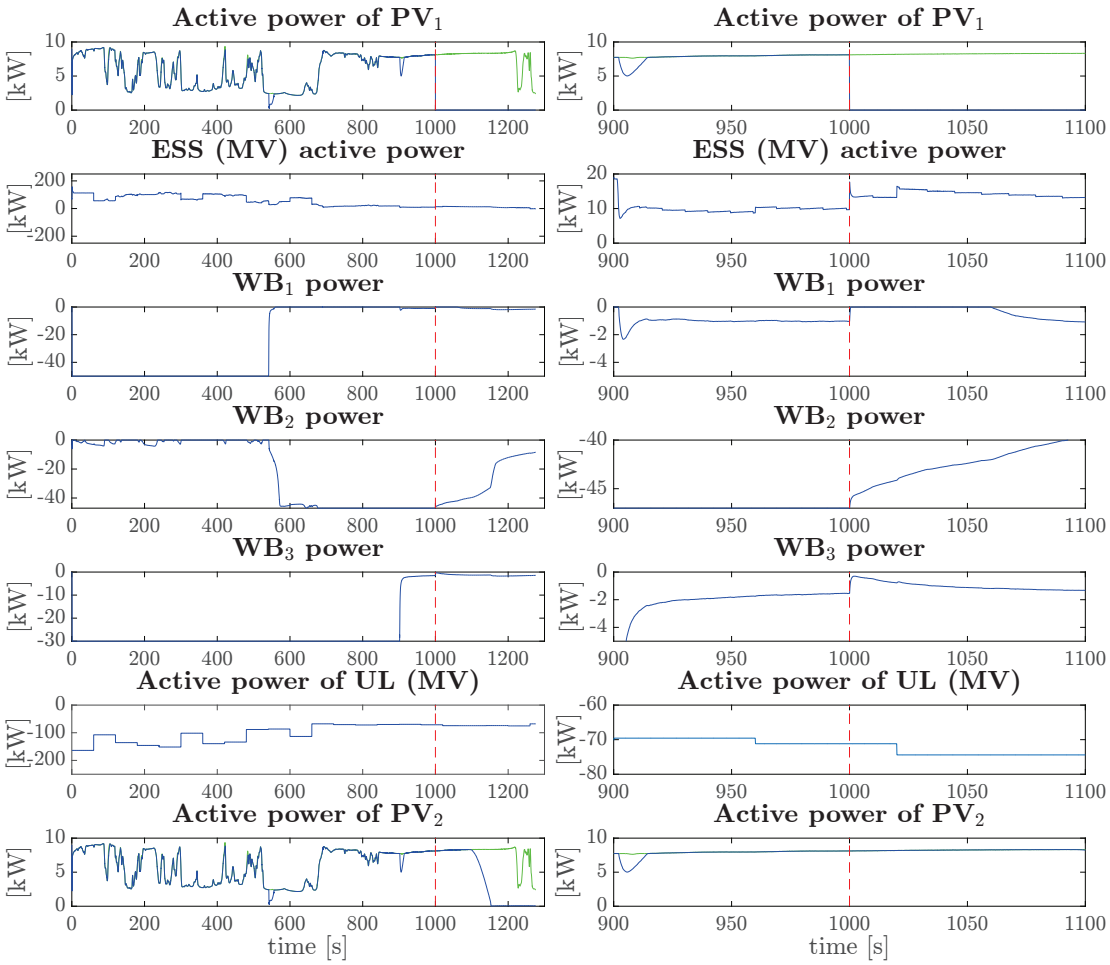

Figure 5.11 – Unexpected disconnection of PV_1 at $t = 1000$[s]. The right column shows a zoom on the left column in the time-window of $[900, 1100]$ seconds.

Figures 5.13 and 5.14 show 4 seconds of simulation of the evolution of the aggregated PQ profile and belief set. For visibility, only one over two messages are presented (therefore the plotted sampling-time is of 200[ms]). For a first observation, note that the power request (blue square) always belongs to the advertised PQ profile (defined by the set with black borders) and that the actual implemented value (red dot) belongs to the advertised belief set (green rectangle). The shape of the aggregated PQ profile is not a perfect rectangle, given the shape of the PQ profile of the PV units, where the power factor limitation imposes the diagonal constraint for negative P. Recall that the aggregation method relies on the approximation of the received PQ profiles to convex polygons. In particular, the circular defined defined by the rated power of the converters (e.g., in the battery agent) is approximated by a rectangle (see Section 3.4 in Chapter 3).

In terms of actual behavior and performance of the aggregated method, we show in Figures 5.15 and 5.16 a longer-term simulation of 120[s].

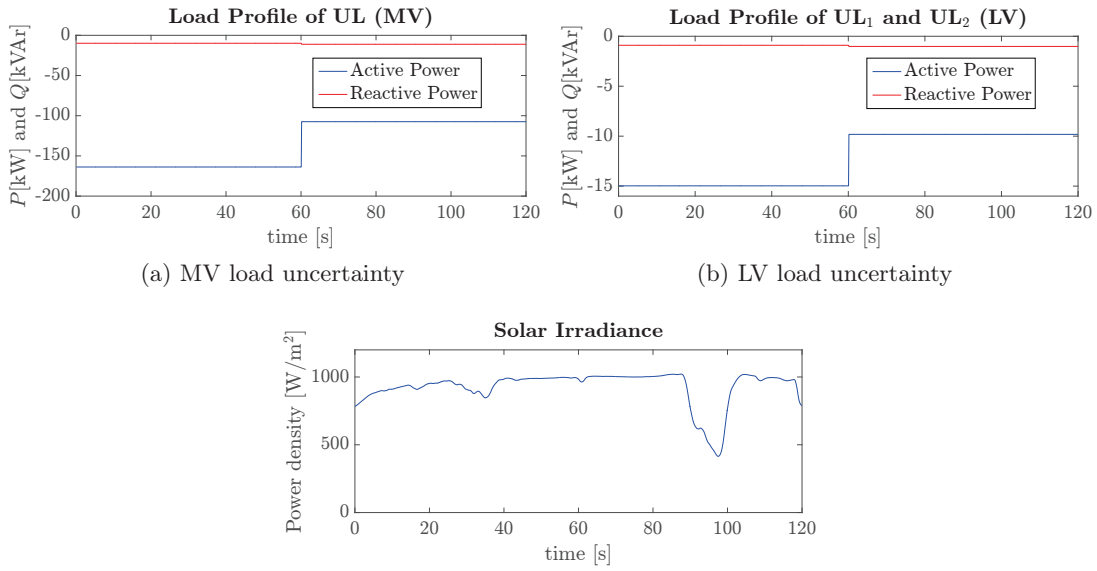

(a) MV load uncertainty

(b) LV load uncertainty

(c) PV uncertainty

Figure 5.12 – Profiles of the uncertain variables for testing the aggregation method.

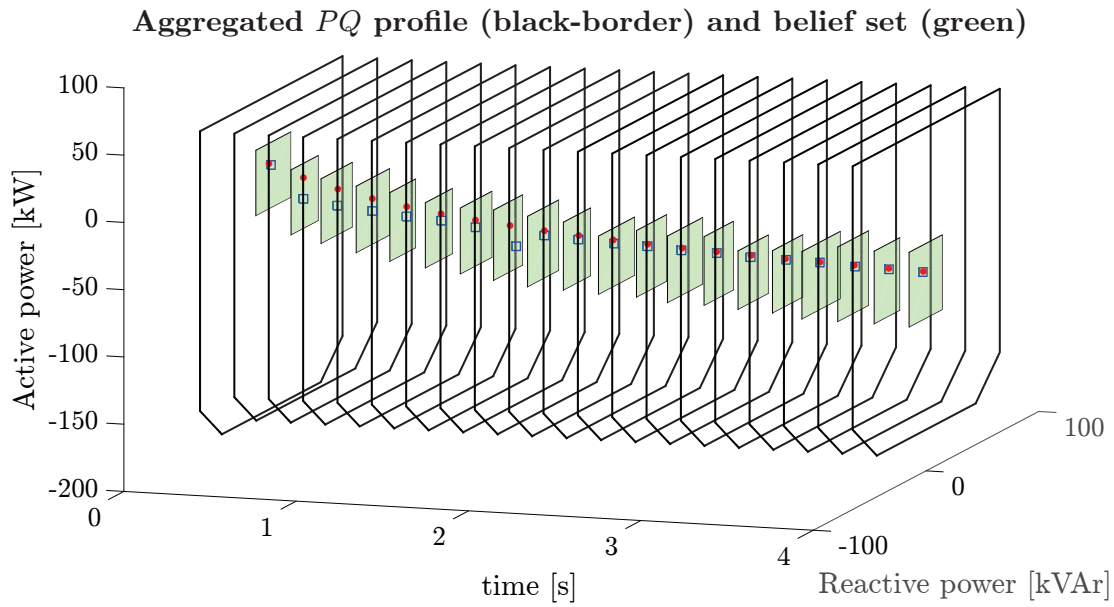

(a) 3D view

Figure 5.13 – Aggregated PQ profile and belief set computed by the LVGA. Red dots represent the implemented LV-MV power flow. Blue squares represent the MVGA request. Green sets represent the belief set of the MVGA request. White sets with black borders represent the PQ profile.

As a result of the variability of the solar irradiance, the aggregated PQ profiles ($\mathcal{AA}$) varies in time following the same shape for both P and Q coordinates. In the Q coordinate,

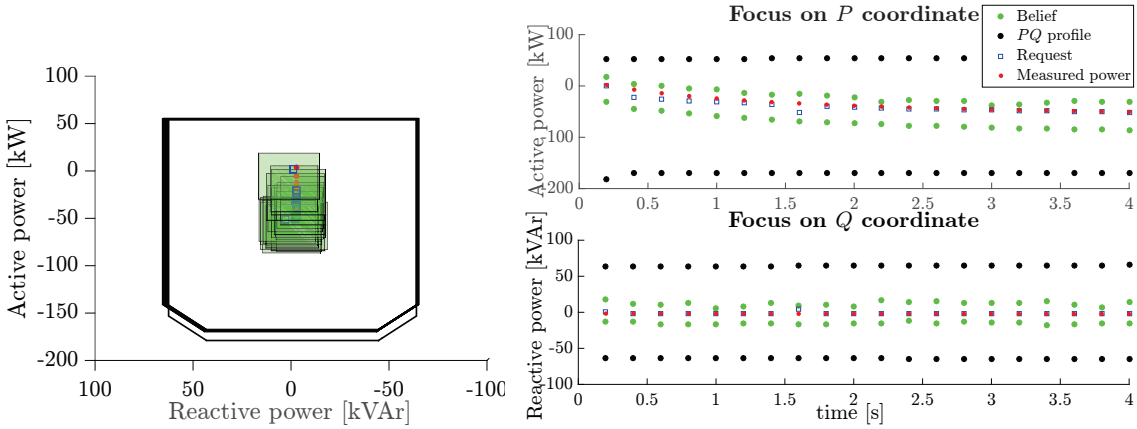

(a) PQ-plane view (b) $P-t$, $Q-t$ view

Figure 5.14 – Aggregated PQ profile and belief set computed by the LVGA. Red circle represents the implemented LV-MV power flow. Blue square represents the MVGA request. Green represents the belief set of the MVGA request. White set with black borders represents the PQ profile.

the power-factor constraint of the PV plants modifies the aggregated PQ profile, by affecting the positive and negative flexibility. The impact of the uncertainty given by the loads profiles is also clear in $t = 60$[s], where the P coordinate of the $A\mathcal{A}$ experiences a jump of 10[kW]. As expected, this jump also affects the MVGA request and the actual implemented power flow.

It can also be seen that, the LVGA sends a consistent advertisement that enables the GA to steer the LV grid according to the MVGA request that follows the aggregation willingness of all the resources in the LV grid. In this case, the aggregated cost expresses the desire of the LV grid to consume given the fact that the water-boiler resources are willing to be charged. In turn, the MVGA power request is consistent with the aggregated cost-function shown in Figure 5.15, stabilizing at the end of the window to the optimum power request.

Indeed, the partial derivative, with respect to P, is positive at the beginning and decreases tending to a close-to-zero negative value; hence, the LVGA wants to minimize production (or maximize consumption) at the beginning of the time window and tries to keep it constant at the end of it. The reason for this very small negative derivative is given by the other objectives of the MVGA, but it is clear that the objective of the LVGA is prioritized. It can be seen, therefore, that the requested and actually implemented power set-points gradually decrease and converge to a constant value as a result. In the case of Q, the derivative is small (compare μ with the values of λ), hence the actual power request does not change significantly, staying near to zero during the entire time-window. Moreover, even when in the case of intense PV dynamics, as those expected in the window from $t = 90$[s] to $t = 100$[s], the cost derivatives are kept smooth. This facilitates the

decision process of the MVGA even in presence of local stochastic resources.

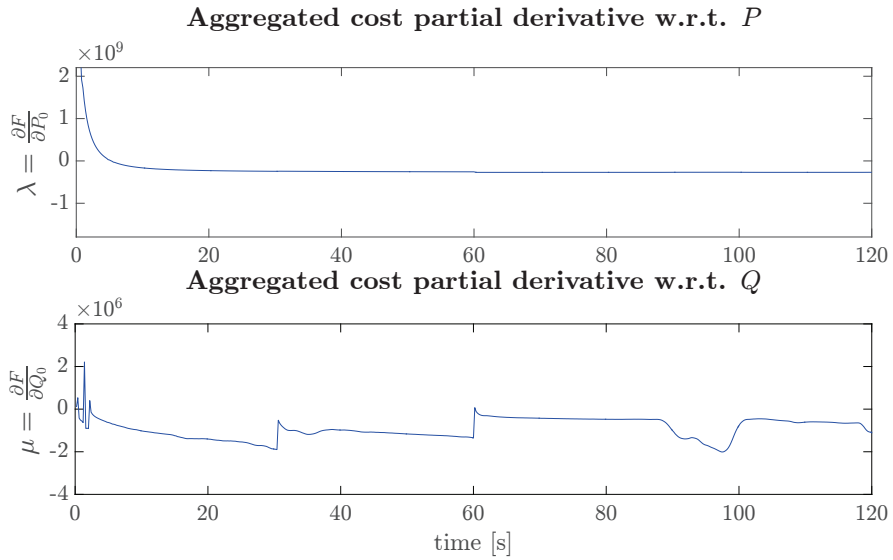

Figure 5.15 – Aggregated cost partial derivatives.

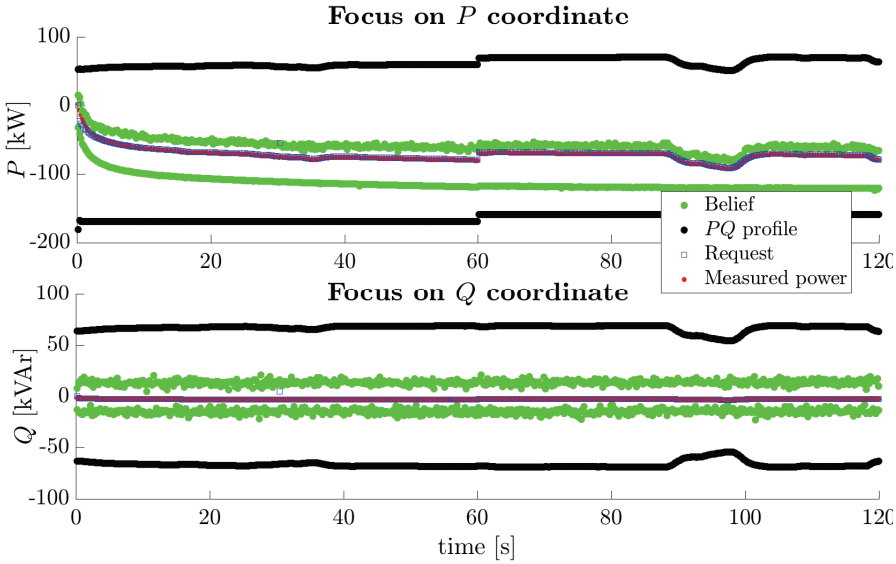

Figure 5.16 – Aggregated PQ profile and belief set computed by the LVGA, along with the actual request and implementation powers at the PCC.

In Figure 5.17, quality-of-service metrics node of voltages and line currents corroborate that, when using the proposed aggregation method, both MV and LV grids are always kept in a safe operation zone (which is the main objective of the control framework).

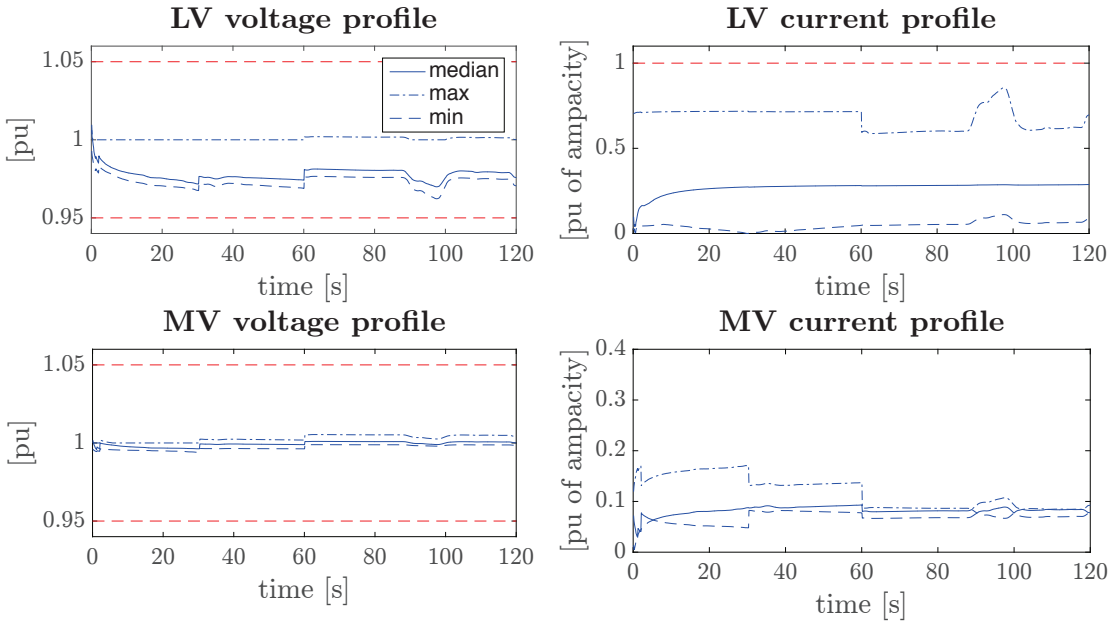

Figure 5.17 – Grid behavior while performing aggregation in a 120[s] time-window.

6 Experimental Setup and Validation

Chapter Highlights:

In this chapter, we present the design of the experimental facility that has been conceived for testing and validating the COMMELEC control framework.
In a first part, special focus is put into the description of the technical specifications of the various physical devices and in the characteristics of the experimental setup.
Secondly, the description of the experiments for the implementation of the framework along with their results are discussed. Emphasis is given to the computational burden needed in all the steps of the process. In particular, results of the operation of the microgrid in grid-connected mode are shown together with a time-latency assessment.

In Chapter 3, the theoretical definition of the COMMELEC framework is presented, and we validate it through simulation in Chapter 5. However, any simulation environment will never be able to completely represent a real system, especially when focusing on real-time control. In this respect, a real-scale experimental facility has been designed with all the typical characteristics of a realistic low-voltage distribution network.

In order to accomplish this target, four main elements are designed and put in place:

1. A weak-by-design power grid, where real line-congestions and voltage-limit violations can arise.
2. A suitable communication network where all devices of the network have access. In the case of COMMELEC, this is especially needed so that the grid agent can (a) *receive*: grid measurements, followers advertisements and external target set-points and (b) *send*: requests to its followers and the advertisement to its leader.
3. A metering infrastructure for visualization purposes that enables the grid agent to estimate in real-time the state of the grid. The COMMELEC framework makes direct use of this information in order to control the microgrid.
4. Equipment on each resource, able to observe, abstract and control the resource state by using the COMMELEC framework.

In the following we provide details concerning the implementation of these elements.

6.1 General Architecture

We setup the thest in order to represent the CIGRÉ LV microgrid benchmark illustrated in [106].

The benchmark network is based on a standard low-voltage feeder that serves a suburban residential area with a limited number of consumers connected along its length and adds various types of microsources and energy storage devices.

To permit efficient modeling and simulation of the microgrid operation, including connected and islanded modes, this benchmark grid keeps the important technical characteristic of realistic low voltage utility grids, while it dispenses with the complexity of actual networks, . It has been conceived to be suitable for steady-state and transient simulations.

The microgrid test-bed is part of the facilities of the Distributed Electrical Systems Laboratory at EPFL. Its general architecture is shown in Figure 6.1. It is connected to the 20[kV] medium-voltage grid of the EPFL campus through a 20/0.4[kV] transformer at bus $B01$ (also called PCC). A controllable breaker is installed between bus $B01$ and the

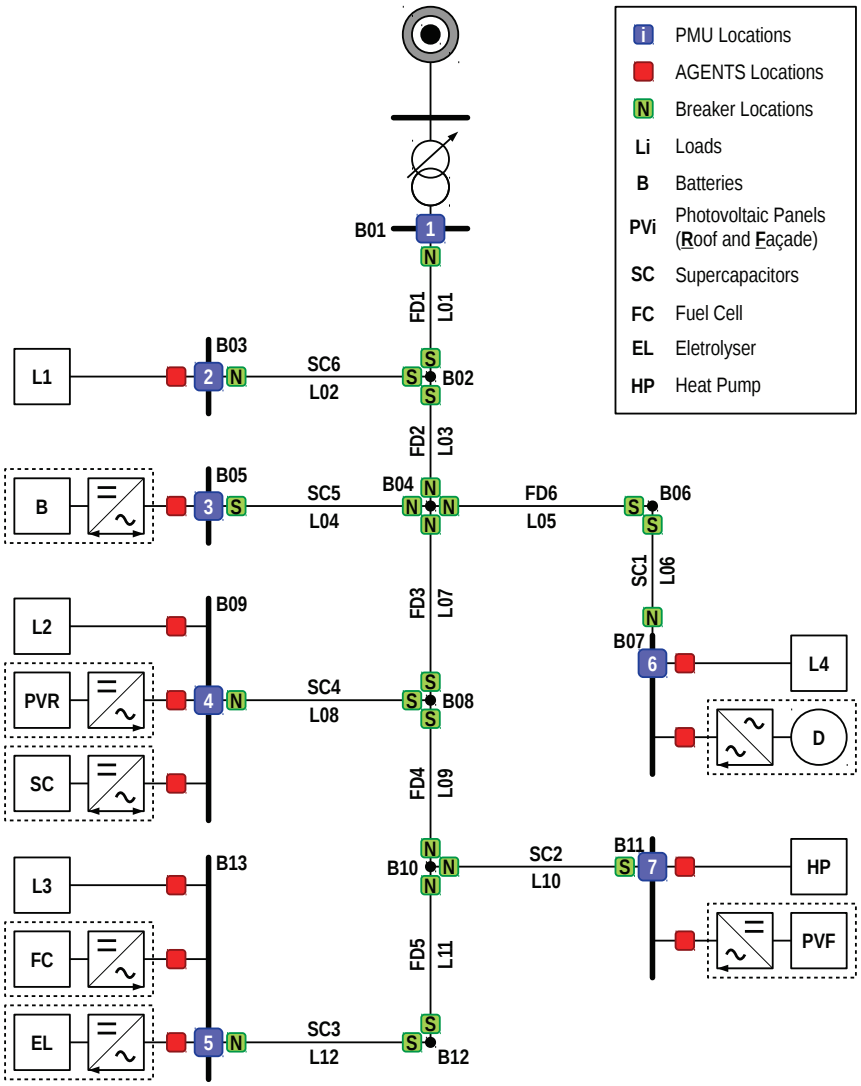

Figure 6.1 – Microgrid overall architecture.

LV/MV transformer in order to enable for both islanded and grid-connected operation modes.

As in [106], we put in place a heterogeneous set of resources in order to test different setups with and without inertia, by increasing or reducing flexibility and controllability, etc. In particular, we used three different storage technologies for exploiting three different levels of energy provision: short, medium and long-term. We consider typical resources found in European networks, such as diesel generators, heat pumps and photovoltaic plants.

In the following, we provide detailed information about each resource in the microgrid.

6.1.1 Batteries

The battery bank is a 25[kW] – 25[kWh] storage system based on the lithium-titanate technology manufactured by the Swiss company, Leclanché. This bank has the special characteristic of having a lifetime of more that 15000 cycles for a 4C discharge rate and a deep of discharge of 100% when operating at 25[°C]. The cell specifications are shown in Figure 6.2a. 60 cells are arranged in one module, with a 20 serial, 3 parallel configuration. The system is installed in a rack with 13 modules.

The rack has its own battery management system. It has an embedded monitoring tool that continuously streams data via several communication channels. It is used for actuating the contactors that connect the batteries with the battery converter, disconnecting them in case of limits violation. Details of the power converters are presented in Section 6.1.7. The entire battery rack is depicted in Figure 6.2b.

Technical Data	
Nominal Capacity	16[Ah] (measured at C/10 discharge rate, RT)
Nominal Voltage	2.3[V]
Voltage range	1.7 to 2.7[V]
Impedance (1[kHz])	$< 2[m\Omega]$
Dimensions Length	162.5[mm] ±1.5[mm]
Dimensions Width	173.5[mm] ±1.5[mm]
Dimensions Thickness	12[mm] $+0.4/-0.2$[mm]
Weight	641[g] ±2[g]
Volume	250[ml] ±3[ml]
Housing	Foil packaging
Tabs	Aluminium (+ Pole), Ni-coated Copper (- Pole)
Tabs Length	33[mm] ± 3[mm]
Tabs Distance	88[mm] ± 2[mm]
Tabs Width	50[mm] ± 0.5[mm]
Tabs Thickness	0.2[mm] ± 0.02[mm]
Expected lifetime	> 15000 cycles
Expected calendar life	20 years
Charge	
Charging method	CC/CV (constant voltage with limited current)
Max charge voltage	2.7[V] (+0.05[V])
Recommended charge current	16[A] (1C)
Max charge current	64[A] (4C)
End of charge	$U = 2.7$[V] and $I < C/10$
Max temperature range	0 to +45[°C]
Discharge	
Recommended discharge current	16[A] (1C)
Max discharge current	64[A] (4C)
End of discharge voltage	1.7[V]
Max temperature range	−20 to +60[°C]
Storage and transport	
Max temperature range	−20 to +60[°C]

(a) Single cell specifications.

(b) Leclanché StoraXe® Storage Rack System SRS0029

Figure 6.2 – Technical specificatios and view of the battery system at the DESL microgrid laboratory.

6.1.2 Supercapacitors

The supercapacitor bank is composed of 6 NESSCAP 125V 62F SR2 modules connected in series. It is a 50[kW] - 0.8[kWh] based a 2.7[V] 3000[F] cell that has a rated cycle lifetime of 1'000'000 cycles at room temperature. With a high power-density and small

energy-density, this storage device is especially effective for very fast power changes such as those coming from loads and PV drops due to cloud passing. The experimental equipment and its technical specifications are shown in Figure 6.3.

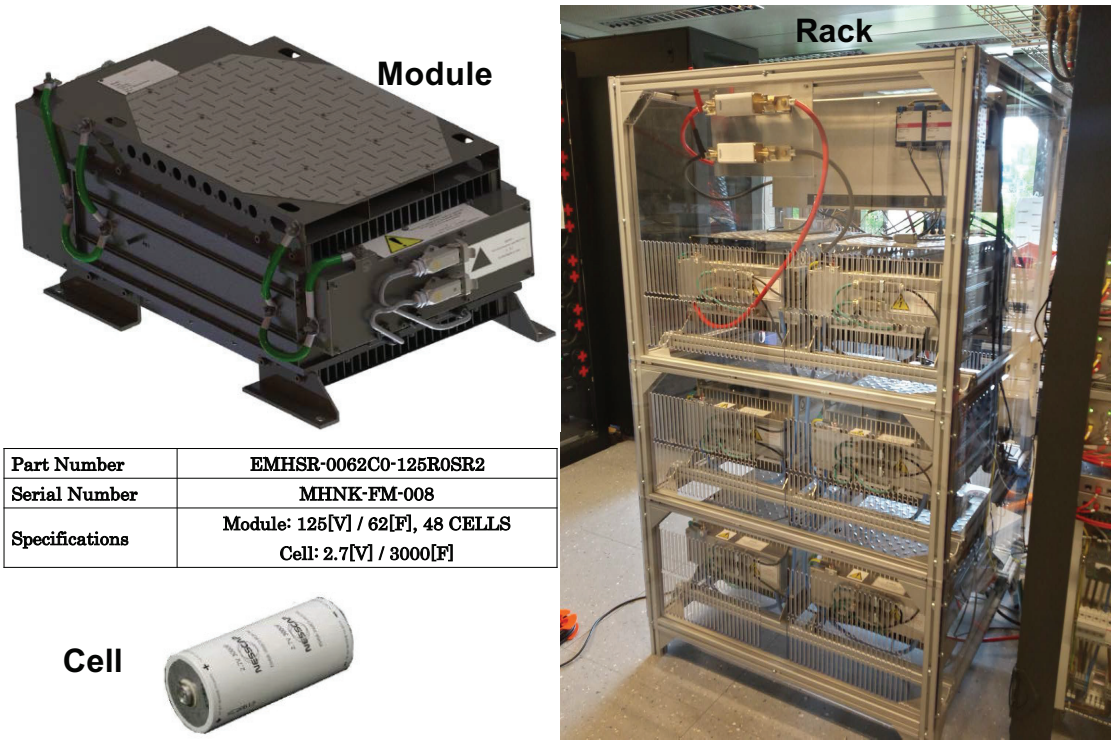

Figure 6.3 – Supercapacitor bank installed at the microgrid test-bed.

6.1.3 Power-to-gas Storage

The power-to-gas storage system is composed by a proton-exchange-membrane (PEM) fuel cell, oxygen and hydrogen storage tanks and a PEM electrolyzer. The general diagram of the setup is shown in Figure 6.4a.

The fuel cell in Figure 6.4b, uses the oxygen and hydrogen from the storage tanks as inputs to generate electricity. Its chemical process also generates heat that is used as by-product. The PEM fuel cell provides 15[kW] electrical and 15[kW] thermal output.

The gas tanks can store 0.9[MWh]@200[bar] and are equipped with pressure and temperature sensors, whose information is sent in real time to a monitoring unit placed in the laboratory.

The electrolyzer is 6[kW] of rated power, producing 1[Nm^3/h] of H_2 and 0.5[Nm^3/h] of O_2 at 30[bar]. Using high-quality de-ionized water as a feedstock, the system produces dry gases, hydrogen and oxygen, ready to be stored for use in the PEM fuel cell. The

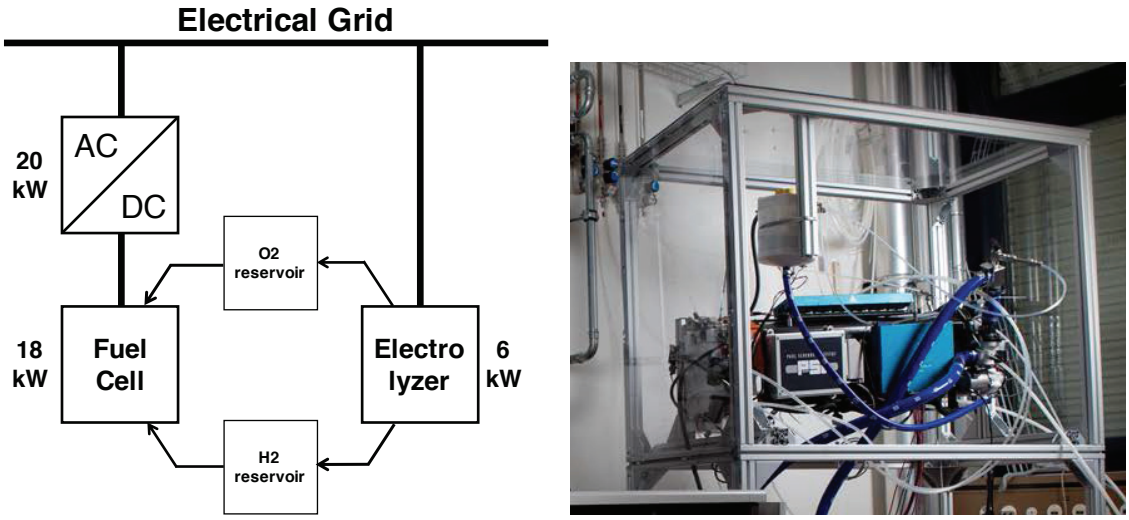

(a) Overall Schematic. (b) Fuel cell

Figure 6.4 – Hydrogen/oxygen storage at the DESL microgrid laboratory.

system offers the possibility to respond to external set-points over the entire power range (0-100%). A simplified scheme of the electrolyzer cabinet and its battery limits is shown in Figure 6.5.

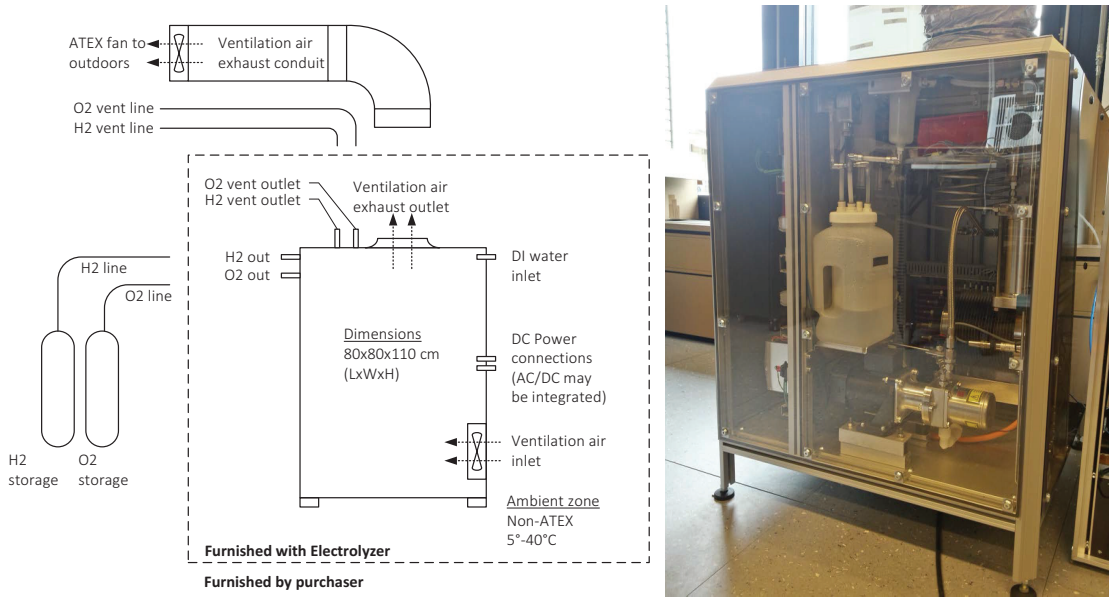

Figure 6.5 – Simplified scheme of the electrolyzer cabinet and its connections to the microgrid and gas storage system (left), and the actual device in the laboratory (right).

It is important to point out that, with batteries, supercapacitors and power-to-gas storage we conceived a system with three storages of different time-scale, that are orchestrated

Figure 6.6 – Hydrogen tanks in the laboratory.

such that they provide services according to their capabilities. We believe that these are the three most expected technologies to be deployed in future distribution networks and microgrids.

6.1.4 Heat Pump

As a controllable load, the microgrid also counts on an air-water SATAG Vitocal 300, type AW 100. It is a one-stage heat pump that provides nominal thermal power of 9[kW] for a *coefficient of performance* (COP) of 3.31 with 10[kW] of rated electrical power. The heat pump uses R407C as working fluids [107].

6.1.5 Load Emulators

Three fast dynamic AC converters with an overall rated power of 30[kVA] are used as load emulators to enable a flexible and unbalanced configuration of loads. Each power converter is connected on a single-phase of the microgrid and injects the power into the EPFL grid. Note that, even if the MV external grid is the same, the converters inject power through a different MV/LV transformer. Each converter can receive an analog signal that then will be amplified as a real current by the converters. The strategy to generate these *booster* signals is shown in Figure 6.8; makes use of the direct-quadrature-zero transformation for allowing decoupled active and reactive reference tracking. The booster-signal generator block (BSG) takes the current set-point i_{abc}^{sp} and fits its values to the input characteristics of the converter.

Figure 6.7 – Heat pump.

For the purposes of this thesis, the load emulators represent a residential building space-heating system. The building is modeled in discrete state-space equations as described in [94] an previously discussed in Section 4.4 of Chapter 4.

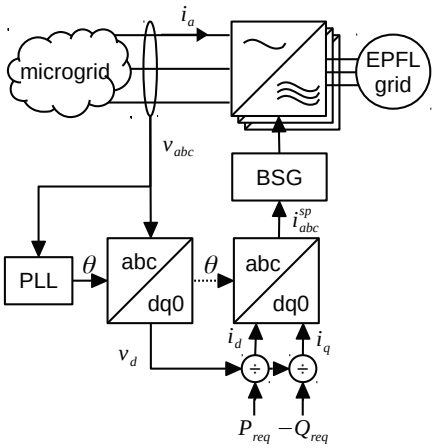

(a) Booster signal generation strategy

(b) Power converters

Figure 6.8 – Setup used for emulating loads.

6.1.6 PV Plants

The main source of uncertainty in the microgrid comes from two photovoltaic (PV) power plants. The first is installed in the roof of the building with 20[kW] of rated power and the second is in the southern facade of the building with 7[kW] of rated power.

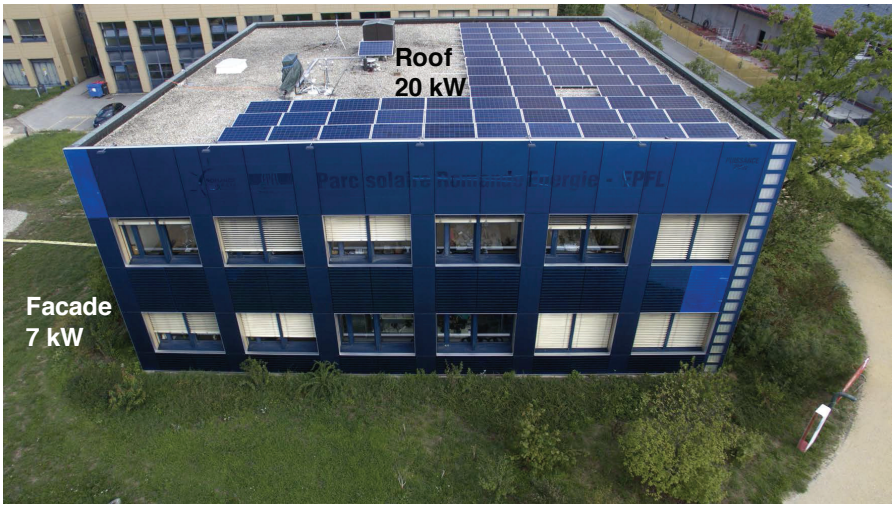

Figure 6.9 – Photovoltaic plants in the building.

In particular, the PV plants use commercial power-converters that work by using only the maximum-power-point-tracking strategy, hence they are not responsive to external power references.

(a) SolarMax for 20kW plant (b) Fronius for 7kW plant

Figure 6.10 – Power converters of PV plants.

6.1.7 Flexible Power-Converters

In order to enable maximum controlability and flexibility for deploying a large variety of experiments, the microgrid is equipped with flexible power-converters designed and manufactured by the EPFL startup *Imperix*. These converters are used to interface the DC buses of the batteries, supercapacitors and fuel cell to the AC microgrid.

The converters are both flexible on hardware and software. The power trenches are designed to be modular and scalable so that it is easy to expand the power capabilities of the converter, and the software enables the user to deploy different control strategies. A representative rack is shown in Figure 6.11, where the main elements are indicated. Note that the resource agent is hosted in the external microcontroller inside the same rack and takes its measurements from the additional measurement board that is not part of the original converter but has been added later.

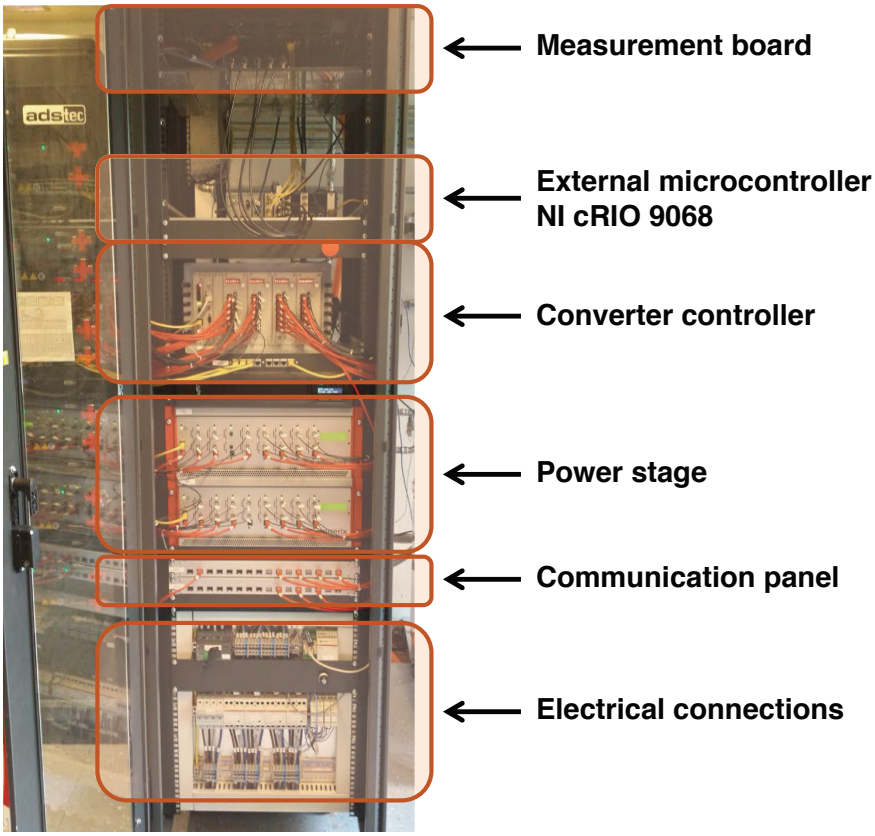

Figure 6.11 – Flexible power converters.

6.1.8 Diesel Generator

For a typical rotating machine, we have installed a combined heat and power diesel-based unit able to provide 12.5[kVA] of electrical output and 15[kW] of thermal output.

6.1.9 Other Planned Devices

In order to describe additional perspectives of the laboratory setup to the reader, w plan to install additional elements in the near future in order to provide more complexity to the microgrid:

- 4x22[kW] real electrical vehicle charging-stations.
- Extension of the PV power capacity of the rooftop installation (see available space in Figure 6.9), enabling this expansion to be interfaced with a fully controllable power converter.
- In order to minimize the effect of the re-injection of powers done by the load emulatores, we plan to add resistive elements that dissipate energy on the microgrid side. This feature is needed, especially when controlling both the MV network and the microgrid.

6.2 Power Network

Recall that, the microgrid power network has been designed in order to reproduce the targeted CIGRÉ LV microgrid benchmark. In this respect, the grid topology and the line lengths were strictly preserved from the benchmark, whereasthe electrical characteristics were slightly modified:

(i) *Overhead lines are emulated using real power coaxial cables.* In order to approximate our setup as much as possible to reality, we opted to use real cables instead of lumped-elements line emulators . This choice brings more realistic grid electrical and thermal behavior of the lines. The use of power coaxial-cables (i.e., shielded), which are representative of standard European LV distribution networks, also allows us to minimize electromagnetic coupling among lines.

(ii) *Intentional weak-grid design.* The cross-section of the cables has been sized such that voltage and/or cable current limits can actually be violated in the presence of stochastic resources.

(iii) *Adapted rated power.* Devices rated power is adapted according to the characteristics of the installation but following, in general, the benchmark recommendations.

We use a worst-case scenario analysis for the sizing of the power cables. For this purpose, two scenarios have been defined:

1. **Full-load scenario**. All loads, including storage systems with negative power-flow, absorb their rated power from the microgrid.
2. **Full-generation scenario**. All producing units, including storage systems with positive power-flow, inject their rated power into the microgrid.

For both scenarios, we run several power-flow simulations, for all the available commercial power-cables. On each simulation, only the cable specifications, cross-section and electrical parameters, are changed. In the simulations, we assume that the voltage at the MV/LV transformer (B01) is 1[pu], base 400[V].

In Table 6.1 and in Table 6.2, the design simulation results, for the full-load scenario and for the full-production, are presented for the selected cables, respectively. Please refer to Figure 6.1 for nomenclature.

Table 6.1 – Design simulation results for the full-load scenario, using the cables of Table 6.3.

(a) Devices power

Device	Node	P[kW]	Q[kVAr]
L1	B03	12	9
B	B05	25	0
L4	B07	21.6	16.2
D	B07	0	0
L2	B09	20	15
PVR	B09	0	0
SC	B09	50	0
HP	B11	10	0
PVF	B11	0	0
FC	B13	0	0
EL	B13	6	0
L3	B13	18.4	13.8

(b) Nodes voltage

Node	V[pu]
B02	0.96
B03	0.95
B04	0.94
B05	0.94
B06	0.92
B07	0.91
B08	0.91
B09	0.89
B10	0.87
B11	0.86
B12	0.86
B13	0.86

(c) Lines current

Line	I[A]	I_{max}[A]
FD1	278	207
FD2	256.5	207
FD3	179.1	135
FD4	62.7	82
FD5	47.5	82
FD6	42.9	82
SC1	42.9	82
SC2	16.8	44
SC3	47.5	82
SC4	117	207
SC5	38.6	108
SC6	22.8	44

Ampacity violations can be seen in the full-load scenario for the main-feeder lines (FD). These violations represent a maximum overload of 34%. In this scenario almost all nodes show voltage violations, considering a feasible range of 1[pu]±5%. In the full-production scenario, no-congestion is found, but most of the nodes also show voltage violations.

We intentionally avoided congestion in the *service connections* lines (SC) as they are typically designed to support the maximum current of the device connected to it. However, the main feeder is typically designed in an earlier stage. Therefore, it is probable to congest it, when adding new devices to the distribution network. Recall that these worst-case scenarios are very rare.

Table 6.2 – Design simulation results for the full-production scenario, using the cables of Table 6.3.

(a) Devices power

Device	Node	P[kW]	Q[kVAr]
L1	B03	0	0
B	B05	25	0
L4	B07	0	0
D	B07	10.6	6.6
L2	B09	0	0
PVR	B09	20	0
SC	B09	50	0
HP	B11	0	0
PVF	B11	5	0
FC	B13	15	0
EL	B13	0	0
L3	B13	0	0

(b) Nodes voltage

Node	V[pu]
B02	1.03
B03	1.03
B04	1.04
B05	1.05
B06	1.05
B07	1.06
B08	1.06
B09	1.08
B10	1.08
B11	1.08
B12	1.08
B13	1.09

(c) Lines current

Line	I[A]	I_{max}[A]
FD1	170	207
FD2	170	207
FD3	120.6	135
FD4	26.7	82
FD5	20	82
FD6	17.2	82
SC1	17.2	82
SC2	17.8	44
SC3	20	82
SC4	93.9	207
SC5	34.7	108
SC6	0	44

The final grid design is presented in Table 6.3.

Table 6.3 – Grid final design. Helukabel TOPFLEX-EMV-UV-3 PLUS 2YSLCYK-J.

Line	Part Number	Length[m]	I_{max}[A]
FD1	22682	70	207
FD2	22682	35	207
FD3	22680	70	135
FD4	22678	105	82
FD5	22678	35	82
FD6	22678	105	82
SC1	22678	30	82
SC2	22676	30	44
SC3	22678	30	82
SC4	22682	30	207
SC5	22679	30	108
SC6	22676	30	44

It is important to mention that the microgrid laboratory was implemented in a reduced space, considering the total length of the sized grid-topology. In this respect, the actual placement of the cables was done by raising the room floor and installing the cables below the new floor level. Even when the chosen cables from the manufacturer are well shielded, i.e. they avoid the electromagnetic interference, for the placement the floor we considered that the cables do not loop, thus avoiding any coil effect that can increase electromagnetic fields production.

6.3 Metering and Situation Awareness System

We assumed to have available a metering system capable of observing the electrical quantities of the main nodes of the microgrid. This can be achieved using standard smart-meters. However, we opted for low-cost phasor measurement units (PMU), as the recent literature promotes and justifies their use also in LV networks [108]. As it is known, PMUs can provide synchronized and time-tagged information, from which we can take advantage to have a reliable grid state knowledge.

Furthermore, we use a PMU that satisfies every requirement defined in the standard for class-P PMUs [109], implemented in a NI cRIO 9068. It uses a novel synchrophasor estimation algorithm that improves the performances of the so-called interpolated-DFT method by means of a specific compensation scheme for the spectral interference produced by the negative image of the spectrum. The algorithm has been fully deployed on the FPGA target only, leaving the CPU free to perform any other task such as the streaming of the estimated quantities, based on the protocol specified by the standard IEEE C37.118.1-2011.

The whole metering process starts with the voltage and current sensors installed at several nodes of the microgrid. We use LEM CV 3-1000 voltage sensors that have an accuracy of $\pm 0.2\%$ at 25[°C] [110] and LEM LF 205-S/SP1 current sensors with an accuracy of $\pm 0.5\%$ at 25[°C] [111]. These sensors feed the PMUs with scaled waveforms in order to estimate the synchrophasors (see Figure 6.12). PMUs encapsulate UDP (user data protocol) datagrams according to the standard and the datagrams are transmitted over a secured and dedicated communication network.

A dedicated low-latency PDC is used [83]. It takes care of the decapsulation of the IEEE C37.118.2 datagrams. It relies on a timeout-based circular buffer that uses synchrophasor time-stamps for time alignment. It finally replaces missing measurements, in order to feed other applications with a consistent and complete set of data. This solution always ensures that the available measurements will be forwarded in an acceptable time range ($\sim$ 20[ms] in case of PMUs streaming at 50[fps]), thus increasing the determinism of the process.

In order to know the actual state of the network in the entire microgrid, we use a linear state-estimation (SE) technique. The adopted SE is based on the discrete Kalman filtering technique (DKF-SE) that is suitable for 3-phase power systems and relies only on nodal synchrophasor measurements provided by PMUs [82].

A diagram of the entire process is presented in Figure 6.13.

Figure 6.12 – PMUs (NI cRIO 9068) and sensors. 1. GPS card (NI 9467), 2-3: acquisition cards (NI 9215), 4: power source (TRACO POWER TML 20215), 5: voltage sensors (LEM CV 3-1000), 6: current signal conditioning board, 7: current sensors (LEM LF 205-S/SP1).

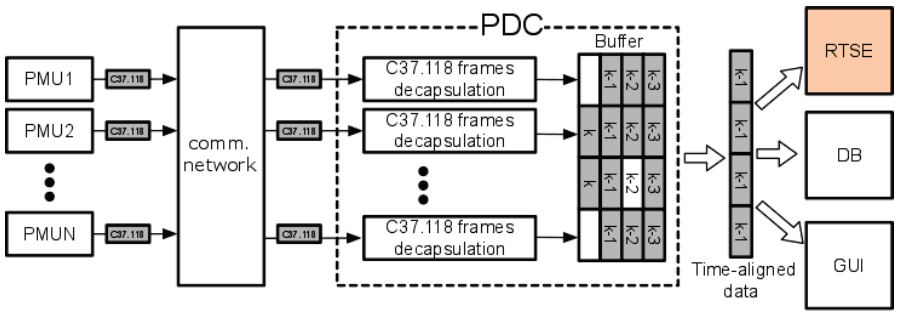

Figure 6.13 – Situation awareness process deployed in the microgrid.

6.4 Resource-Agents Hardware and Software

Every resource in the microgrid is equipped with a National Instruments CompactRIO 9068 that acts as a controller and can locally command and query the resource, in other words, it serves as an intermediate player between the real actuator and an external device that wants to communicate information to the resource. This device is of special importance for enabling the flexibility of the experimental setup. Any new control technique can be programmed here without changing the bottom-level actuator behavior.

In the context of the COMMELEC framework, this micro-controller hosts the resource

agent that will

1. verify the feasibility of a requested power set-point,
2. command the resource to implement the verified power set-point and
3. provide in real time an internal view of the resource in the generalized format.

For accomplishing these tasks, the RA uses a device-specific communication protocol to speak with the resources controllers (e.g., batteries, supercapacitors, etc.), whereas in general we use CAN bus to speak with the converter controllers. The general layout of the physical interaction between devices is shown in Figure 6.14a. The measurement board is equipped with the same sensors as the power network (see Figure 6.12).

Furthermore, a schematic diagram of the various processes deployed on the micro-controller during normal operation is shown in Figure 6.14b. For simplicity, mode transitions (start-up, control to voltage mode, etc.) are not shown but are also supported. In particular, there are four main parallel processes.

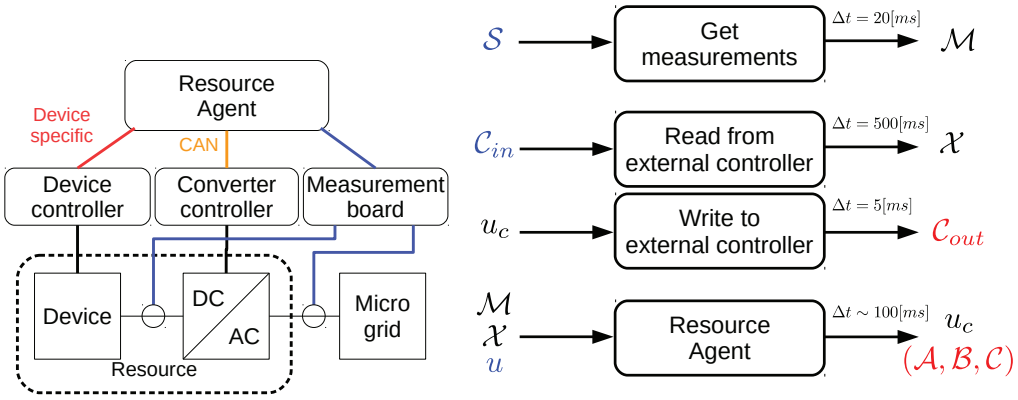

(a) Hardware setup.

(b) Software setup.

Figure 6.14 – Resource-agent hardware and software setup. In the right diagram external inputs are highlighted in blue and external outputs in red. The time-delays Δt shown on each process represent the expected execution periodicity.

1. The first process obtains sampled signals $\mathcal{S}$ from current and voltage sensors, and computes power measurements $\mathcal{M}$ every 20[ms]. The algorithm used for this computation is the same used in the PMUs [109], hence $\mathcal{M}$ is expressed using complex power phasors.
2. The second process obtains communication packets $\mathcal{C}_{in}$ from external resource controllers (device or converter controller) and transforms them into a meaningful

state vector $\mathcal{X}$. Slow-dynamics variables, such as temperature, are typically taken from these controllers, whereas fast-dynamics electrical variables are taken from the measurement board. In general, given the communication bandwidth of typical protocol (CAN, MODBUS, PROFIBUS, etc.), this loop runs at a pace of 500[ms].

3. The third process takes a command $u_c = (P_c, Q_c)$ (not necessarily equal to the request from the GA, u) and translates it into the corresponding format (according to the protocol) to be sent to the actuator (typically the converter) in the message $\mathcal{C}_{out}$. This process is typically executed every 5[ms] but only sends a message when there is new input. This fast pace enables us to minimize the implementation delay.

4. Finally, the fourth process is the resource agent. It takes the request u sent by the GA, along with the local measurements $\mathcal{M}$ and $\mathcal{X}$, and computes the command u_c and the advertisement $(\mathcal{A}, \mathcal{B}, \mathcal{C})$. This loop runs only upon receiving a new request, hence its pace is defined by the GA. The four loops communicate among themselves by reading and writing global variables, hence, they work in an asynchronous fashion.

A generic resource-agent implements four consecutive tasks, as depicted in Figure 6.15.

1. **Compute Power Constraints.** Upon receiving a new request from the GA $u(t_0)$, it takes the measured RA state $\mathcal{X}(t_0)$ and $\mathcal{M}(t_0)$ and computes the current PQ-capabilities of the resource.

2. **Project to Power Constraints.** Then, at t_1, it verifies the feasibility of the requested set-point $u(t_0)$ according to these power constraints. This is done through a simplified Euclidean projection. The result of this projection is the command $u_c(t_2)$. In the actual implementation, the projection is done assuming that different constraints can be expressed in convex sets, either in cartesian $\mathcal{A}^c$ or in polar $\mathcal{A}^p$ coordinates (typical examples for $\mathcal{A}^c$ are active power limits and for $\mathcal{A}^p$ apparent power limits). The actual PQ profile is the intersection of both sets $\mathcal{A} = \mathcal{A}^c \cap \mathcal{A}^p$. Then naming initially $u^*[0] = u(t_0)$, we alternately compute (changing the coordinates on each iteration):

$$u^*[k] = \inf_{\substack{x \in \mathcal{A}^i \\ i=\{p,c\}}} \{||x - u^*[k-1]||\}, \tag{6.1}$$

   where $||\cdot||$ is the euclidean $\mathbb{R}^2$. The iteration ends when $||u^*[k] - u^*[k-1]|| < \epsilon$, for $\epsilon > 0$ a small number. Then $u_c(t_2) = u^*[k]$.

3. **Send Command and Wait.** It overwrites the register and waits until the set-point is actually implemented; delay will depend on the nature of each resource.

4. **Compute Advertisement.** After this necessary delay, it again obatains the variables $\mathcal{X}(t_3)$ and $\mathcal{M}(t_3)$ that represent a new state after the power set-point

implementation, and it computes the new advertisement $(\mathcal{A}, \mathcal{B}, \mathcal{C})(t_4)$ to be sent to the GA.

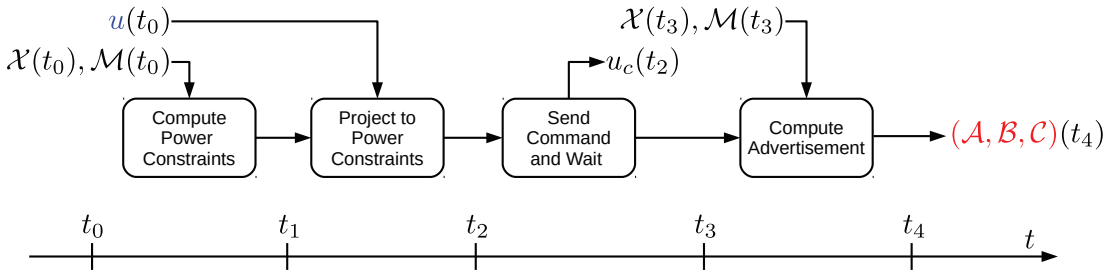

Figure 6.15 – Full process performed by a generic resource agent. It is expected that the computation time $t_4 - t_0 < 20$[ms].

6.5 Grid-Agent Hardware

The GA was written in C++. Currently, we run the GA on a Scientific Linux 7.2 64-bit desktop workstation, but the GA code was designed so that it can be portable to less powerful embedded platforms, and it was already tested for cross-compilation to embedded platforms such as ARM.

In the same machine runs a PDC and a RTSE, both programmed in LabView, which enable the GA to receive continuous updates of the real state of the microgrid as in the SCADA, which are instead used in this case for control purposes.

6.6 Communication Infrastructure

The microgrid is equipped with a dedicated reliable and secure communication network, using the iPRP redundancy protocol [112] (see Figure 6.16). We use two TP-LINK TL-SG1048 Gigabit switches that enable a duplicated 1000[Mbps] communication bandwidth. All devices, PMUs, RAs, GA and monitoring units are wired-connected using category 5.e Ethernet cabling (max. 20[m]). The cables are to be shielded, as they are installed alongside with the power cables.

For this implementation, we use the IPv4 protocol. PMUs and RAs send their data by using IP multicast, so that the messages are received both at the GA and at a monitoring unit (SCADA). For reliability, the devices of the microgrid use the iPRP redundancy protocol proposed in [112]. Both the GA and the SCADA have their own PDC and RTSE.

Experimental round-trip package latencies between two devices in the network (say grid agent and 1 resource agent) are of 0.228[ms] in average.

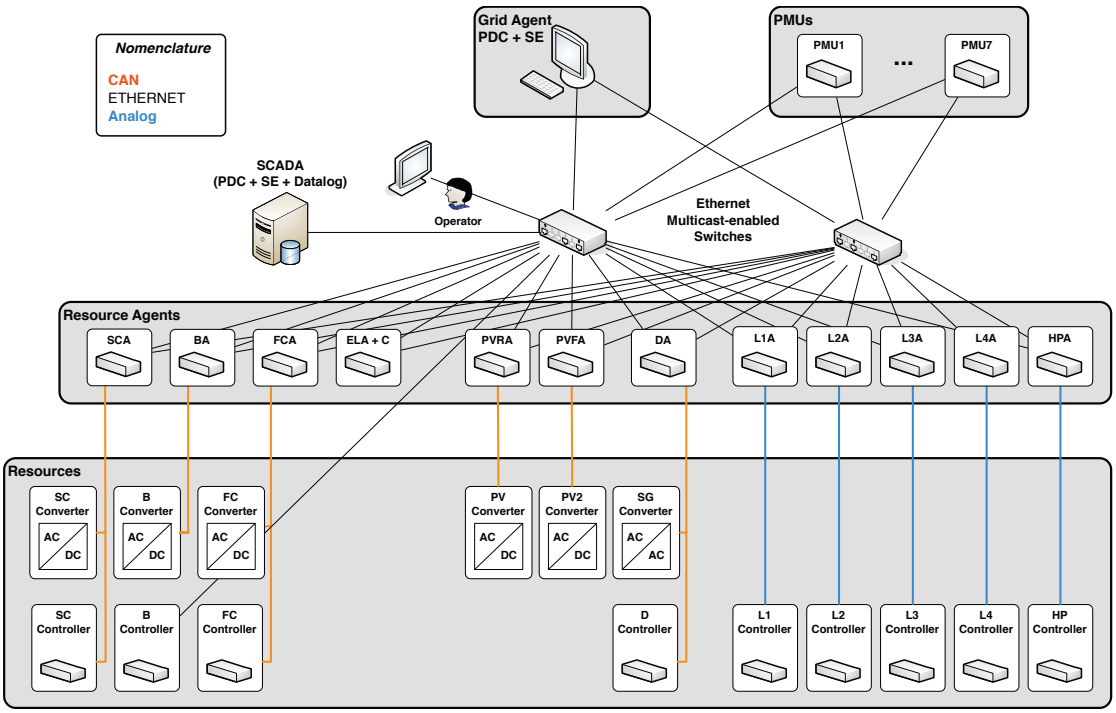

Figure 6.16 – Communication network of the experimental microgrid.

6.7 Protections

The microgrid is equipped with 3 levels of protection:

1. The automatic circuit breakers, dimensioned according to the ampacity of the power cables, as defined in Section 6.2.

2. A software-based protection, which continuously runs in the SCADA and uses the RTSE output. The SCADA acts directly on the circuit breakers through their auxiliary contacts. This feature could also be used for the assessment of grid topology changes.

3. A manual emergency stop (panic button) that the operator triggers to open all breakers at once.

6.8 Experimental Results

In this section we present the experimental results of the implementation of the COMM-ELEC framework on the EPFL microgrid operating in grid-connected mode.

In order to facilitate the understanding of the results, a reduced set of the setup of Figure 6.1 has been considered for this experimental validation. In this case, only three

resources are used. The battery bank, the roof PV plant, working as an uncontrollable generator, and a load that emulates the behavior of an 8-room building with heaters of 3[kW] of rated power (namely, the load has a maximum consumption of 24[kW]). In our emulation, this load has a consumption with a power factor of 0.995.

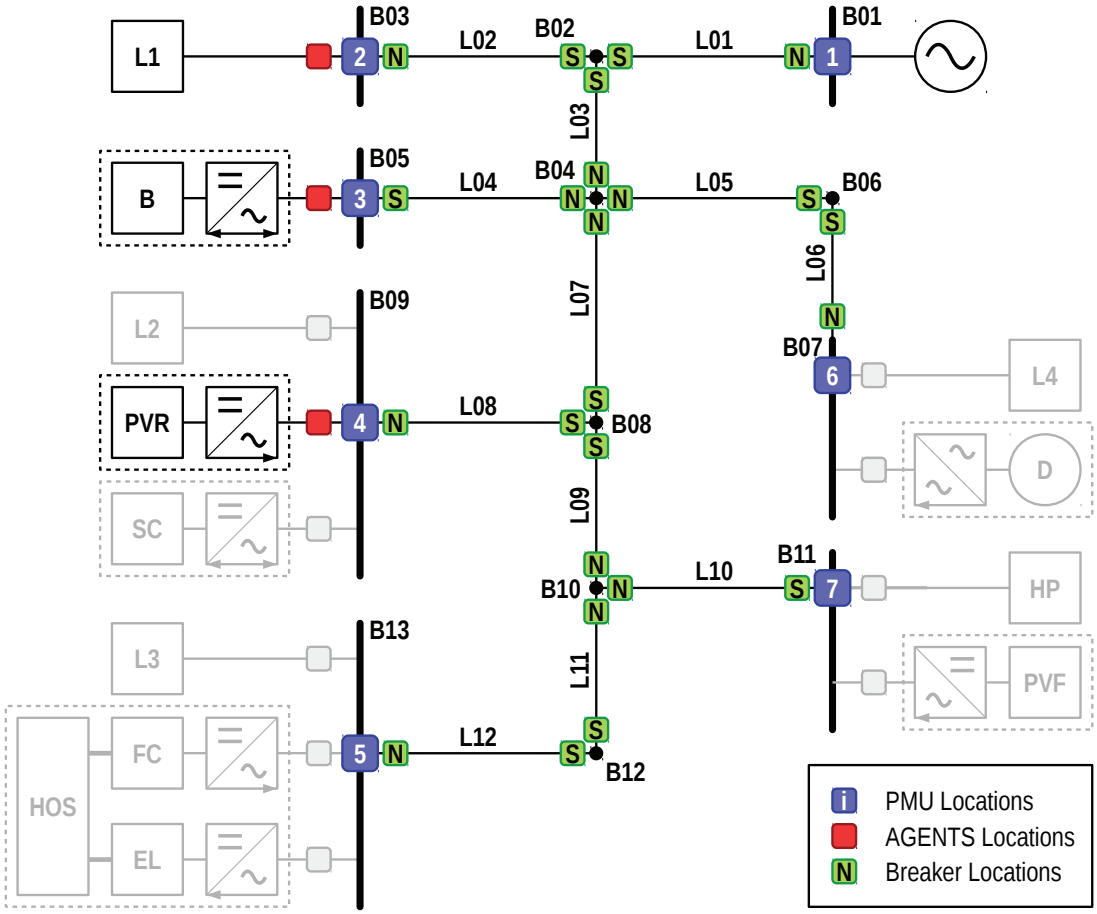

Figure 6.17 – Microgrid setup used for performing the experiments.

We have performed three types of experiments.

1. The first shows the operation of the microgrid when there is no external request, i.e., the grid agent will minimize the cost of the followers by respecting the operational limits of the grid.

2. In the second, we make the microgrid work as a virtual power-plant by providing frequency support to the main grid, using a classic droop characteristic and respecting the internal optimality and security.

3. A third operation mode is shown, where the grid agent receives a continuous request from the main grid and steers the microgrid resources in order to follow such a

request.

Note: the rated power of the selected devices is small with respect to the lines ampacities as presented in Table 6.3. With this, the expected voltage variations are also small, and do not compromise the safe operation of the microgrid. In order to test the ability of the framework to avoid unfeasible operation, we virtually defined the ampacity of line L01 to 30[A].

Finally, we present a latency assessment of the overall process that includes the computation of the RAs, the estimation of the state of the grid and the computation of power set-points performed by the GA.

6.8.1 Local Grid Safety and Optimality

In this experiment, we assumed that there is no request from the external grid, and that the microgrid works in grid-connected mode, while try to meet the needs of the resources defined by the virtual costs, and respecting their operational constraints defined by the PQ profiles. To push the system to its limits, we chose a scenario where the battery needs to be charged and the rooms in the building are cold, in other words, both resources would need to consume energy.

At the beginning of the experiment, in Figure 6.18, the battery starts charging at its maximum allowed power 25[kW], but given the current limitation in line L01, the power consumption of the building is reduced. Note that, given the gradient of the penalty function associated with the current limits, the GA opts to keep an operational margin of the current in line L01, with respect to the ampacity. As the battery charges at full power, its flexibility (defined by the PQ profile) is accordingly reduced in time. As the battery losses its flexibility, the load can increment its consumption.

The congestion management performed by the GA is clear around $t = 400$[s]. As the battery flexibility has decreased substantially, the load tries to increment its consumption in 6[kW]. However, as the resulting current in line L01 is too close to the ampacity, the GA request to the battery to temporarily counteract by reducing its charge (increase active power) and by reducing its reactive power compensation. After a while, the load consumption decreases and the battery is again limited by its own flexibility.

Right after $t = 700$[s], when some clouds make the solar production variable, due to the current limit, the flexible load, restricted by its discrete nature, is requested to adapt its consumption in order to track the solar variations. This shows explicitly how the COMMELEC framework, being agnostic of the resource it is controlling, is able to perform real-time demand-response.

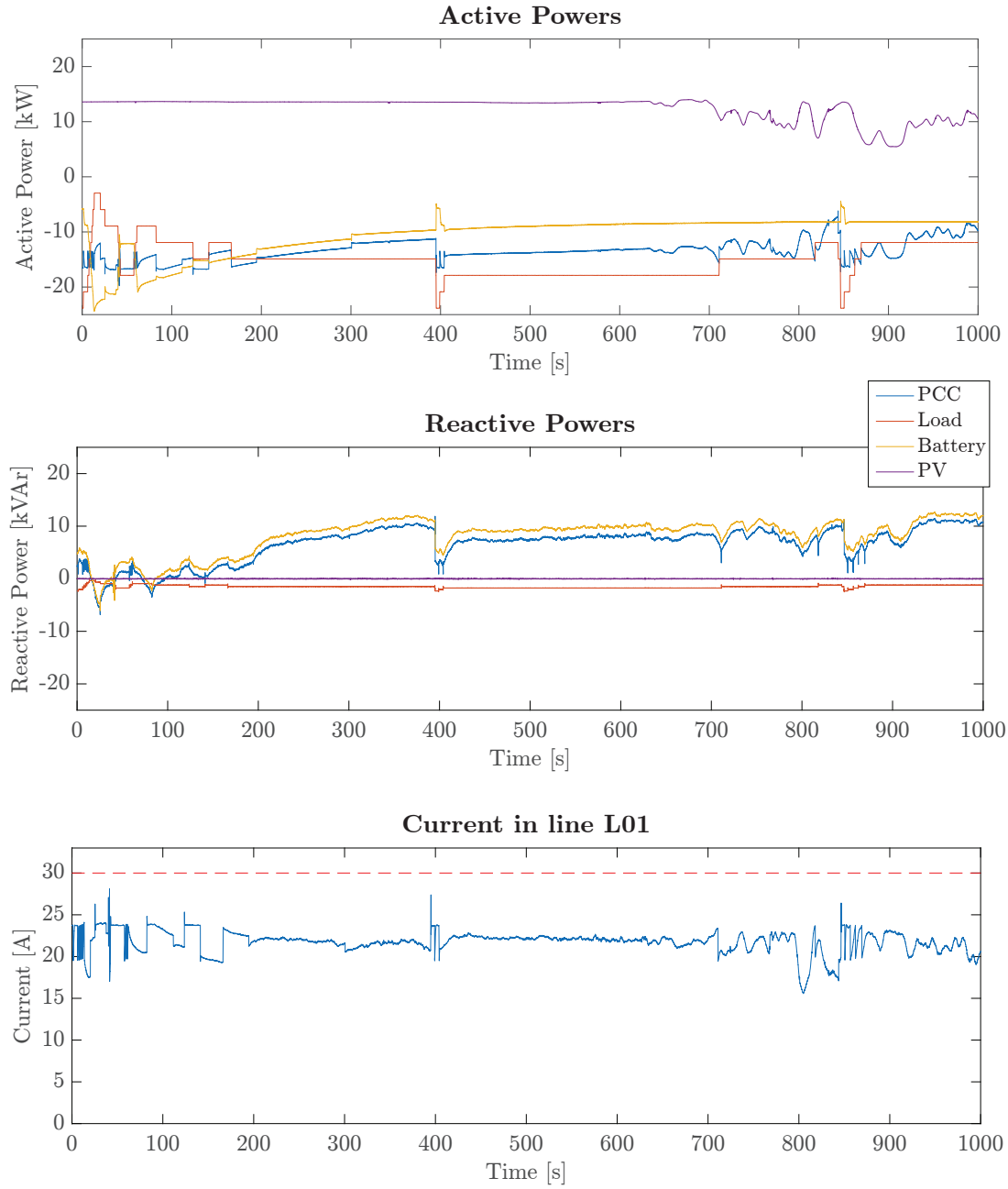

Figure 6.18 – Experimental results for the microgrid operation when operating with the COMMELEC framework without external request.

6.8.2 Primary Frequency Support

We now present an experiment where the microgrid offers frequency support to the main grid. In order to do so, the GA first computes candidate power set-points as usual. Then, it computes an estimate of the power flow at the PCC, $P_0(u)$, as if the candidate

power set-points where implemented. It then applies a droop law to compute the target power-flow P_0 at the PCC

$$P_0 = P_0(u) - \frac{1}{m_f}(f_{nom} - f), \tag{6.2}$$

where m_f^{-1} is the droop parameter whose selected value for our experimental testing is 200[kW/Hz]. This is compatible with the maximum measured frequency in the EPFL grid $\Delta f_{max} = 0.2$[Hz] [83] and half of the maximum power range of the actual setup $0.5\Delta P_{max} \sim 40$[kW]. The factor 0.5 is chosen as a safety margin that accounts for the uncertainty of the PV resource. $f_{nom} = 50$[Hz] is the nominal frequency and f the actual measured frequency. This target power is then used again by the GA for computing new power set-points, as if this was a request from the upper GA. For this experiment, we assume that there is no special need for the reactive power flow at the PCC.

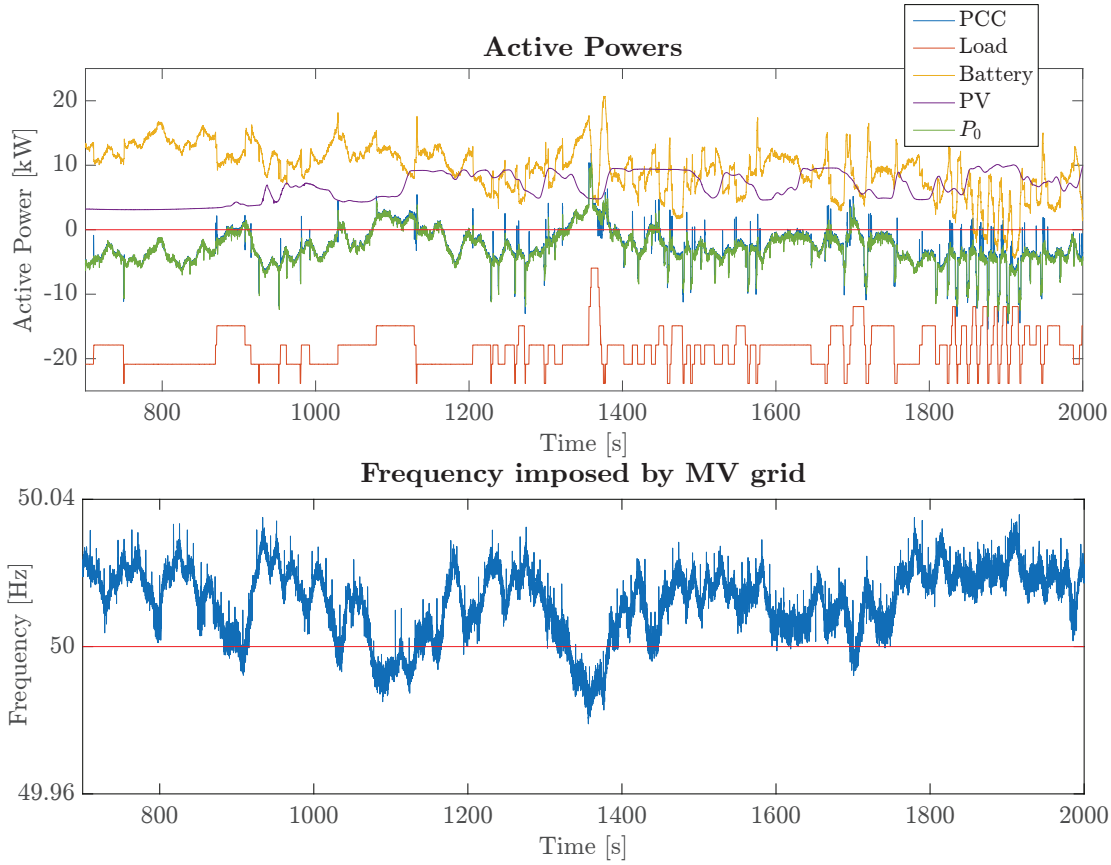

Figure 6.19 – Experimental results for the microgrid operation when providing frequency support under the umbrella of the COMMELEC framework. In this scenario, the internal resources have complementary objectives.

We show in Figure 6.19 a case when the load and the battery have complementary objectives, in other words, the load wants to consume while the battery wants to be

discharged. We see that, even with the volatility of the solar irradiance, the GA is able to steer the flexible resources to provide frequency support. Indeed, the power flow at the PCC follows the shape of the frequency signal (flipped) by utilizing both the battery and the load.

In turn, in Figure 6.20 we show the case when the load and the battery resources have contradictory objectives from the point of view of the power at the PCC, i.e., both the battery and load want to consume power. This situation might force the microgrid to continuously consume power from the grid. Instead, we see that even when both resources follow their internal desire, the GA is able to find power set-points that track the frequency signal, again providing frequency support with the microgrid as an overall.

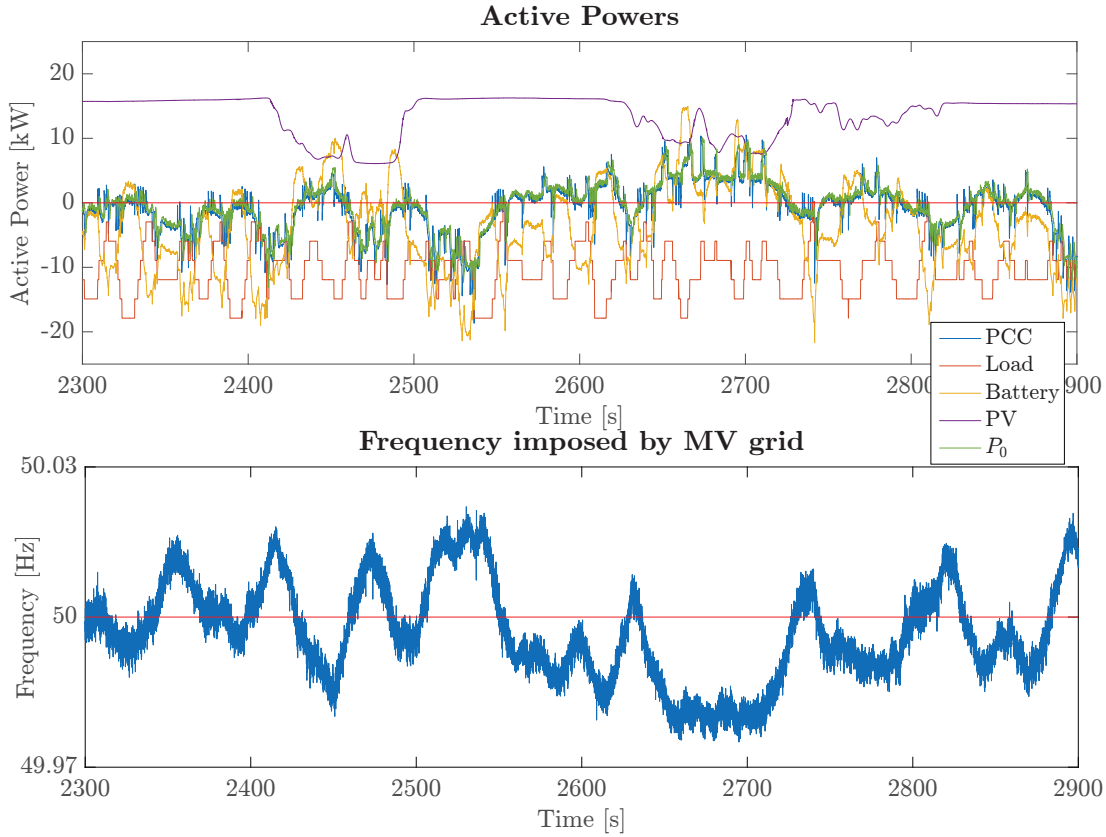

Figure 6.20 – Experimental results for the microgrid operation when providing frequency support under the umbrella of the COMMELEC framework. In this scenario, the internal resources have contradictory objectives.

It is interesting to see that, because of the discrete action of the building emulator, some small spikes are present in the actual implemented power-flow at the PCC. This behavior is a natural consequence of the discrete nature of the controller and is an inherent definition of the advertisement on each RA. Indeed, recall that the set-point computation

is done in a continuous way, whereas the discrete nature of the flexible building resource is embedded into the belief function that is used for verifying the feasible of the power set-points.

6.8.3 Microgrid Real-Time Dispatchability

In this experiment, we show the case where the microgrid is continuously requested to change its power flow at the PCC. As an example, in Figure 6.21 we test a pre-defined cyclic request for active power that is directly sent to the GA. He intentionally selected a request that forces the flow in line L01 to be close to violating the current limit. We also set a constant reactive power request $Q_0 = 0$[kVA].

It is possible to see that the external set-point is almost always tracked, except in the cases when the current in line L01 is close to its ampacity limit, independent of the variability of the PV production. Likewise, both the battery and the load behave according to the external request that the GA distributes among them.

On the reactive-power side, as the load has a power factor of 0.995, its reactive-power curve follows the active-power one. Therefore, in order to follow the external request, the battery is requested to compensate.

For details, Figure 6.22 presents a zoom to the previous figure, where the detailed behavior of the resources is shown. It is especially important to see that, even when the external set-point and the internal desire of the microgrid resources are opposite, as when the load decreases its consumption even when the microgrid is requested to consume more, the GA finds a feasible set of set-points that follows the external request by instructing the battery be charged instead.

6.8.4 Latency Assessment

As a confirmation of the real-time capabilities of the framework, in Figure 6.23 the measured time-delays of a full COMMELEC cycle are shown. The measurements were taken during all the experiments previously presented. Recall that, the COMMELEC cycle is characterized by three steps:

1. Wait until receiving the advertisements from all the resource agents. These processes naturally run in parallel.

2. Only after all advertisements are received, wait until receiving a meaningful update of the state of the grid. As in our demonstrator, the state-estimation technique is done through phasors, we have experimentally assessed that an updated measurement is always stable after three estimation periods.

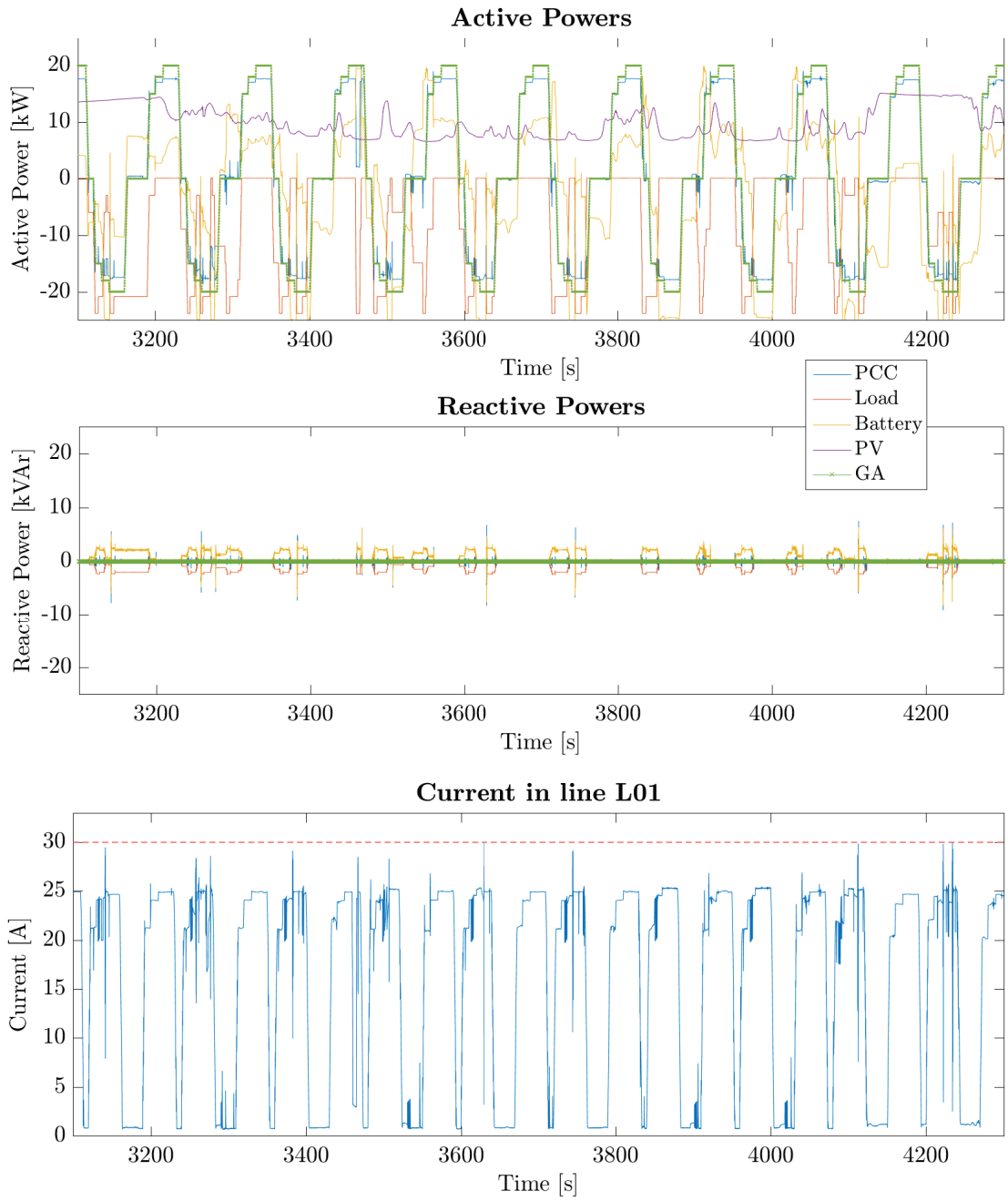

Figure 6.21 – Experimental results for the microgrid operation when operating of the COMMELEC framework with a pre-defined external request.

3. Perform the set-points computation and send them to the resource agents.

We see that a full COMMELEC cycle always takes less than 100[ms] and that its maximum delay is incurred in the process of getting a new meaningful state measurement.

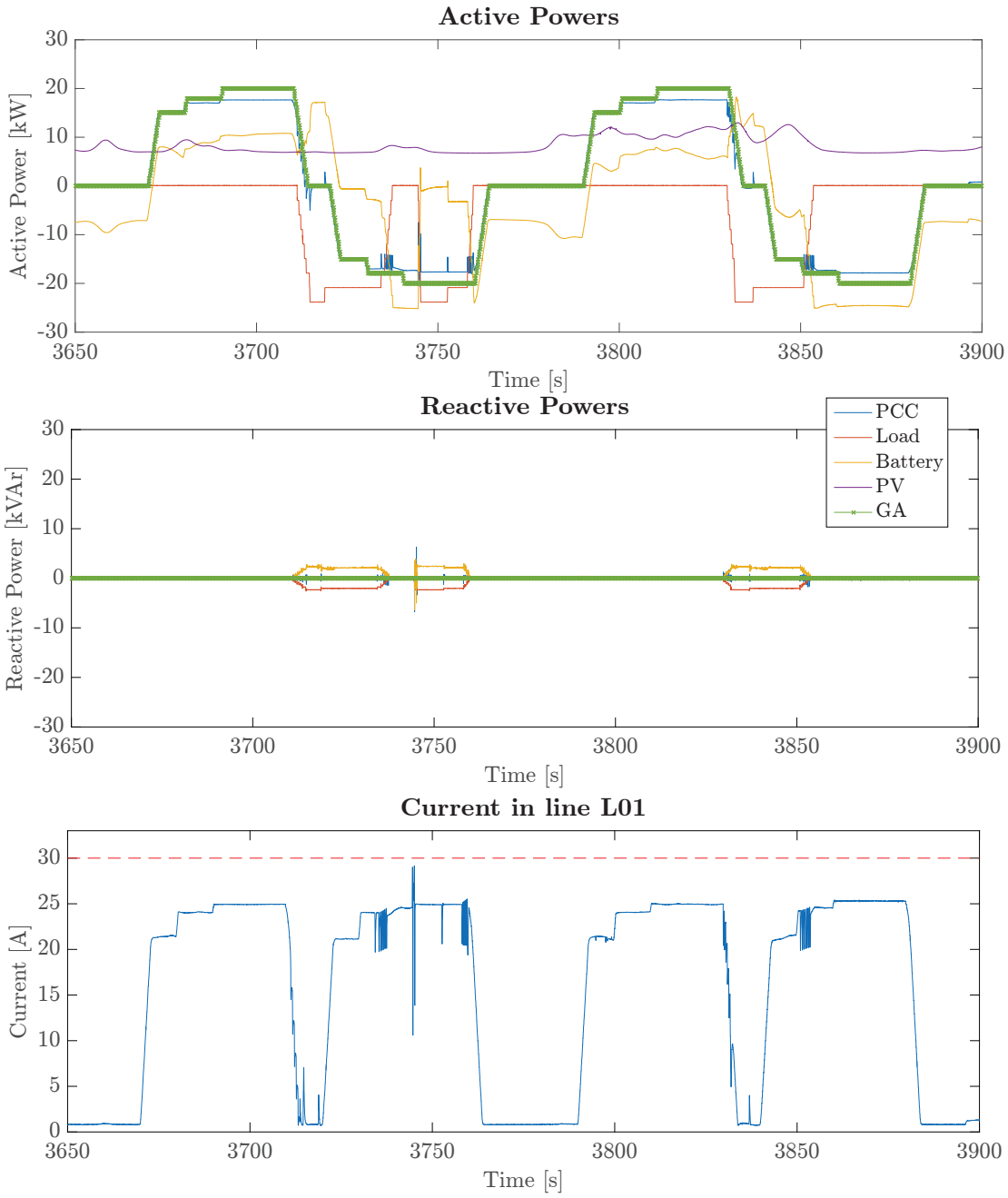

Figure 6.22 – Experimental results for the microgrid operation when operating of the COMMELEC framework with a pre-defined external request. Detailed view.

Specifically, the time needed for the computation of the set-points, after receiving all the needed information is shown in Figure 6.24. In average the set-point computation takes less than 1[ms]. In very few cases, the computation takes a bit longer than 2[ms].

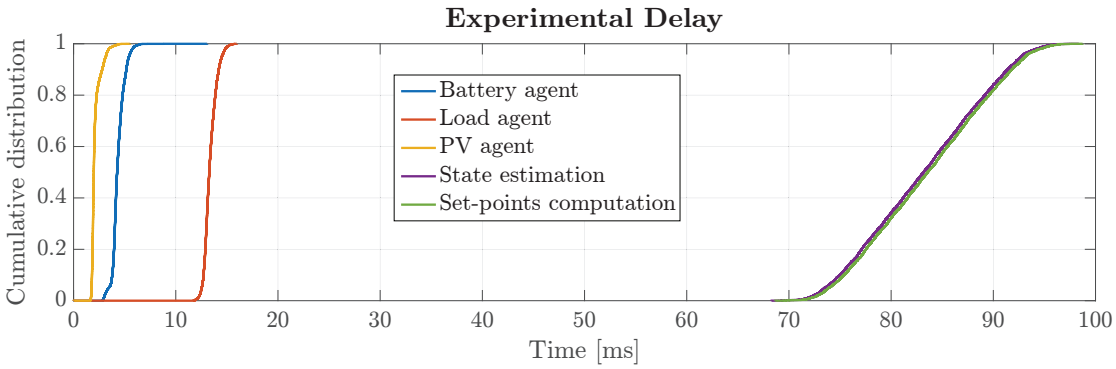

Figure 6.23 – Time delays incurred in a full COMMELEC cycle.

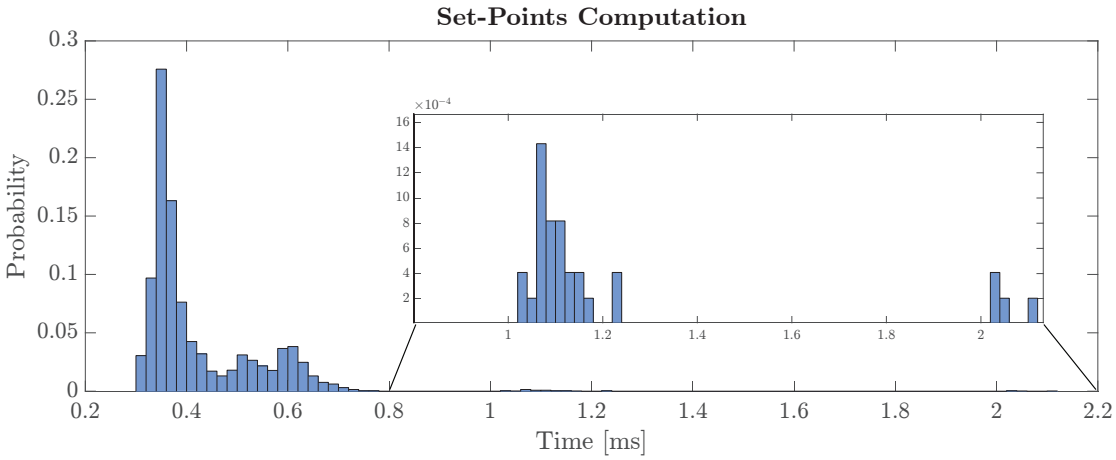

Figure 6.24 – Computation effort made by the GA at computing set-points.

7 Conclusions

We have introduced a control framework that uses explicit power set-points in order to perform real-time control of electrical grids in a scalable and reliable way. The main feature of the proposed control framework is *composability* that enables for scalability. We have verified the applicability of the framework, both via off-line simulations and laboratory experiments. We performed the simulations on a case study composed of a low voltage microgrid benchmark (proposed by CIGRÉ Task Force C6.04.02) connected to a generic medium voltage feeder.

Our proposed framework achieves several desirable performance goals in an islanded distribution network and in a grid-connected microgrid, in the presence of highly volatile resources. As already mentioned, these goals are achieved through a simple and generic method, with a key property of composability. It can be seen that this property enables us to easily achieve the implementation of the framework in higher levels of power grids, up to the transmission level.

Furthermore, it is shown that the properties of the COMMELEC framework are fundamental in the case of *inertia-less grids*. Such grids are typically associated with energy conversion systems interfaced to the AC grid via power electronic converters. Indeed, in the cases where these energy-conversion systems represent the majority of the electricity supply means, the control strategies have to be revisited. In this respect, as the proposed framework does not rely on any shared signals (i.e., frequency), it can inherently account for the control of inertia-less grids. This feature potentially enables its application to generic and more complex power systems. It can be concluded that the proposed control scheme represents an effective *actuation method* for the real-time (sub-second) control of active distribution networks capable of accounting for the main requirements associated with the evolution of these grids.

We have given special emphasis to the experimental validation of the framework, which is a key aspect that is generally minimized. We have carried out the laboratory experiments on a real-scale microgrid connected to the medium voltage feeder of the EPFL campus.

The selected cases study are characterized by

(i) the typical level of complexity of distribution networks,

(ii) a pervasive penetration of renewable energy resources,

(iii) the presence of distributed storage systems, and

(iv) the fact that most of the inertia comes from storage and thermal loads rather than rotating machines.

The obtained results confirm that the proposed real-time control framework is able to efficiently steer such a system in the presence of extremely volatile energy resources. Our main findings are

(a.) the framework is able to indirectly control the reserve of the storage systems, thus maximizing the autonomy of the islanding operation,

(b.) it keeps the system in feasible operation conditions and better explores, compared to existing techniques, the various degrees of freedom that characterize the system, and

(c.) it maintains the system's power equilibrium without using the frequency as a global variable, even being able to do so in inertia-less systems.

Potential Further Research

In the continuation of this work, the following topics are identified for further research and potential industrial applications.

- Extension of the COMMELEC framework to 3-phase systems, in order to take into account the unbalanced nature of power distribution networks. In principle, this will need the introduction of an advertisement that is characterized by a higher cardinality. It is particularly of interest for further research: for instance, for the PQ profile, the coupling or decoupling between bounds defined per phase and the inclusion of the coupled or decoupled implementation of the set-points.

- Under the umbrella of the proposed framework, the necessary conditions for finding a unique solution to the load-flow problem for meshed grids is to be investigated. In particular, the definition of a region around the current operating conditions as a function of the expected implemented power-flows defined by the belief functions of the resource agents.

- As the grid agent control function is designed to solve a robust optimization problem at all layers of the power system, the decision at the highest layer could be too conservative (or the problem could become unsolvable), due to the strictness of the feasible state of operation bounds and the simplifications done in the computation of the aggregated belief sets. In this respect, the investigation of the inclusion of the belief function in the solution of optimization problem is suggested, in other words, to not use it only as a robustness verification. It would also be interesting to investigate the inclusion of *soft constraints* into the definition of the feasible operation state.

Bibliography

[1] Observ'ER. 14th inventory of worldwide electricity production from renewable energy sources, 2012.

[2] David MacKay. *Sustainable Energy-Without the Hot Air*. UIT Cambridge, 2008.

[3] K.A. Papadogiannis and N.D. Hatziargyriou. Optimal allocation of primary reserve services in energy markets. *IEEE Transactions on Power Systems*, 19(1):652–659, Feb. 2004.

[4] European Network of Transmission System Operator for Electricity (ENTSO-E). UCTE Operation Handbook. Technical Report v. 2.5, 2004.

[5] European Network of Transmission System Operator for Electricity (ENTSO-E). Draft network code on demand connection. Technical report, December 5 2012.

[6] N. Troy, D. Flynn, and M. OMalley. Multi-mode operation of combined-cycle gas turbines with increasing wind penetration. *IEEE Transactions on Power Systems*, 27(1):484–492, Feb. 2012.

[7] J. Machowki, J.W. Bialek, and J.R. Bumby. *Power System Dynamics*. John Wiley & Sons, Ltd., second edition, 2008.

[8] M. Paolone, editor. *Editorial*. Sustainable Energy, Grids and Networks, 2015.

[9] N. Hatziargyriou, editor. *Microgrids: Architectures and Control*. John Wiley and Sons Ltd., 2014.

[10] R. H. Lasseter. Microgrids. In *Power Engineering Society Winter Meeting, 2002. IEEE*, volume 1, pages 305–308 vol.1, 2002.

[11] A. Ulbig, T.S. Borsche, and G. Andersson. Impact of low rotational inertia on power system stability and operation. https://arxiv.org/pdf/1312.6435.pdf, 2014.

[12] N. Pogaku, M. Prodanovic, and T. C. Green. Modeling, analysis and testing of autonomous operation of an inverter-based microgrid. *IEEE Transactions on Power Electronics*, 22(2):613–625, March 2007.

[13] J. A. Peças Lopes, C. L. Moreira, and A. G. Madureira. Defining control strategies for microgrids islanded operation. *IEEE Transactions on Power Systems*, 21(2):916–924, 2006.

[14] J. M. Guerrero, M. Chandorkar, T. L. Lee, and P. C. Loh. Advanced control architectures for intelligent microgrids - part I: Decentralized and hierarchical control. *IEEE Transactions on Industrial Electronics*, 60(4):1254–1262, April 2013.

[15] D. Georgakis, S. Papathanassiou, N. Hatziargyriou, A. Engler, and C. Hardt. Operation of a prototype microgrid system based on micro-sources quipped with fast-acting power electronics interfaces. In *Power Electronics Specialists Conference, 2004. PESC 04. 2004 IEEE 35th Annual*, volume 4, pages 2521–2526 Vol.4, 2004.

[16] D.E. Olivares, A. Mehrizi-Sani, A.H. Etemadi, C.A. Cañizares, R. Iravani, M. Kazerani, A.H. Hajimiragha, O. Gomis-Bellmunt, M. Saeedifard, R. Palma-Behnke, G.A. Jimenez-Estevez, and N.D. Hatziargyriou. Trends in microgrid control. *IEEE Transactions on Smart Grid*, 5(4):1905–1919, 2014.

[17] M. C. Chandorkar, D. M. Divan, and R. Adapa. Control of parallel connected inverters in standalone ac supply systems. *IEEE Transactions on Industry Applications*, 29(1):136–143, Jan 1993.

[18] J. Rocabert, G. Azevedo, I. Candela, R. Teoderescu, P. Rodriguez, and I. Etxebarria-Otadui. Microgrid connection management based on an intelligent connection agent. In *IECON 2010 - 36th Annual Conference on IEEE Industrial Electronics Society*, pages 3028–3033, Nov 2010.

[19] T. L. Vandoorn, B. Meersman, J. D. M. De Kooning, and L. Vandevelde. Directly-coupled synchronous generators with converter behavior in islanded microgrids. *IEEE Transactions on Power Systems*, 27(3):1395–1406, Aug 2012.

[20] Y. W. Li and C. N. Kao. An accurate power control strategy for power-electronics-interfaced distributed generation units operating in a low-voltage multibus microgrid. *IEEE Transactions on Power Electronics*, 24(12):2977–2988, Dec 2009.

[21] T.E. Del Carpio-Huayllas, D.S. Ramos, and R.L. Vasquez-Arnez. Microgrid transition to islanded modes: Conceptual background and simulation procedures aimed at assessing its dynamic performance. In *Proceedings of the 2012 IEEE PES Transmission and Distribution Conference and Exposition (T&D)*, 2012.

[22] Jeffrey M. Bloemink and M. Reza Iravani. Control of a multiple source microgrid with built-in islanding detection and current limiting. *IEEE Transactions on Power Delivery*, 27(4):2122 – 2132, Oct. 2012.

[23] Qiang Fu, AdelNasiri, Vijay Bhavaraju, Ashish Solanki, Tarek Abdallah, and David C. Yu. Transition management of microgrids with high penetration of renewable energy. *IEEE Transactions on Smart Grid*, 5(2):539 – 549, March 2014.

[24] I. Grau, L. M. Cipcigan, N. Jenkins, and P. Papadopoulos. Microgrid intentional islanding for network emergencies. In *Universities Power Engineering Conference (UPEC), 2009 Proceedings of the 44th International*, pages 1–5, Sept 2009.

[25] M. Rizo, F. Huerta, E. Bueno, and M. Liserre. A synchronization technique for microgrid reclosing after islanding operation. In *IECON 2012 - 38th Annual Conference on IEEE Industrial Electronics Society*, pages 5596–5601, Oct 2012.

[26] T. L. Vandoorn, B. Meersman, J. D. M. De Kooning, and L. Vandevelde. Transition from islanded to grid-connected mode of microgrids with voltage-based droop control. *IEEE Transactions on Power Systems*, 28(3):2545–2553, Aug 2013.

[27] C. Cho, J. H. Jeon, J. Y. Kim, S. Kwon, K. Park, and S. Kim. Active synchronizing control of a microgrid. *IEEE Transactions on Power Electronics*, 26(12):3707–3719, Dec 2011.

[28] F. Tang, J. M. Guerrero, J. C. Vasquez, D. Wu, and L. Meng. Distributed active synchronization strategy for microgrid seamless reconnection to the grid under unbalance and harmonic distortion. *IEEE Transactions on Smart Grid*, 6(6):2757–2769, Nov 2015.

[29] N.W.A Lidula and A.D. Rajapkse. Voltage balancing and synchronization of microgrids with higly unbalanced loads. *Renewable and Sustainable Energy Reviews*, 31:907 – 920, 2014.

[30] N. Hatziargyriou, G. Contaxis, M. Matos, J. A. P. Lopes, G. Kariniotakis, D. Mayer, J. Halliday, G. Dutton, P. Dokopoulos, A. Bakirtzis, J. Stefanakis, A. Gigantidou, P. O'Donnell, D. McCoy, M. J. Fernandes, J. M. S. Cotrim, and A. P. Figueira. Energy management and control of island power systems with increased penetration from renewable sources. In *Power Engineering Society Winter Meeting, 2002. IEEE*, volume 1, pages 335–339 vol.1, 2002.

[31] R. Palma, C. Benavides, F. Lanas, B. Severino, L. Reyes, J. Llanos, and D. Saez. A microgrid energy management system based on the rolling horizon strategy. *IEEE Transactions on Smart Grid*, 4(2):996 – 1006, May 2013.

[32] D. E. Olivares, C. A. Cañizares, and M. Kazerani. A centralized optimal energy management system for microgrids. In *2011 IEEE Power and Energy Society General Meeting*, pages 1–6, July 2011.

[33] F. Katiraei, R. Iravani, N. Hatziargyriou, and A. Dimeas. Microgrids management. *IEEE Power and Energy Magazine*, 6(3):54–65, May 2008.

[34] M. B. Delghavi and A. Yazdani. An adaptive feedforward compensation for stability enhancement in droop-controlled inverter-based microgrids. *IEEE Transactions on Power Delivery*, 26(3):1764–1773, July 2011.

[35] X. J. Zhao, J. Dong, C. J. Zhang, and X. M. Meng. Modeling and stability analysis of autonomous microgrid composed of inverters based on improved droop control. In *2016 IEEE 8th International Power Electronics and Motion Control Conference (IPEMC-ECCE Asia)*, pages 1720–1724, May 2016.

[36] X. Yu, A. M. Khambadkone, H. Wang, and S. T. S. Terence. Control of parallel-connected power converters for low-voltage microgrid - part I: A hybrid control architecture. *IEEE Transactions on Power Electronics*, 25(12):2962–2970, Dec 2010.

[37] F. Katiraei and M. R. Iravani. Power management strategies for a microgrid with multiple distributed generation units. *IEEE Transactions on Power Systems*, 21(4):1821–1831, Nov. 2006.

[38] A. Vargas-Serrano, D. Sáez, L. Reyes, B. Severino, R. Palma-Behnke, and R. Cárdenas-Dobson. Design and experimental validation of a dual mode vsi control system for a micro-grid with multiple generators. In *IECON 2012 - 38th Annual Conference on IEEE Industrial Electronics Society*, pages 5631–5636, Oct 2012.

[39] W. Yao, M. Chen, J. Matas, J. M. Guerrero, and Z. M. Qian. Design and analysis of the droop control method for parallel inverters considering the impact of the complex impedance on the power sharing. *IEEE Transactions on Industrial Electronics*, 58(2):576–588, Feb 2011.

[40] K. De Brabandere, B. Bolsens, J. Van den Keybus, A. Woyte, J. Driesen, and R. Belmans. A voltage and frequency droop control method for parallel inverters. *IEEE Transactions on Power Electronics*, 22(4):1107–1115, July 2007.

[41] J. He, Y. W. Li, J. M. Guerrero, F. Blaabjerg, and J. C. Vasquez. An islanding microgrid power sharing approach using enhanced virtual impedance control scheme. *IEEE Transactions on Power Electronics*, 28(11):5272–5282, Nov 2013.

[42] Q. C. Zhong and Y. Zeng. Universal droop control of inverters with different types of output impedance. *IEEE Access*, 4:702–712, 2016.

[43] J. He and Y. W. Li. Analysis, design, and implementation of virtual impedance for power electronics interfaced distributed generation. *IEEE Transactions on Industry Applications*, 47(6):2525–2538, Nov 2011.

[44] José Matas, Miguel Castilla, Luis García de Vicuña, Jaume Miret, and Juan Carlos Vásquez. Virtual impedance loop for droop-controlled single-phase parallel inverters using a second-order general-integrator scheme. *IEEE Transactions on Power Electronics*, 25(12):2993 – 3002, December 2010.

[45] Q. C. Zhong. Robust droop controller for accurate proportional load sharing among inverters operated in parallel. *IEEE Transactions on Industrial Electronics*, 60(4):1281–1290, April 2013.

[46] G. Hou, F. Xing, Y. Yang, and J. Zhang. Virtual negative impedance droop method for parallel inverters in microgrids. In *Industrial Electronics and Applications (ICIEA), 2015 IEEE 10th Conference on*, pages 1009–1013, June 2015.

[47] J. M. Guerrero, N. Berbel, L. G. de Vicuna, J. Matas, J. Miret, and M. Castilla. Droop control method for the parallel operation of online uninterruptible power systems using resistive output impedance. In *Twenty-First Annual IEEE Applied Power Electronics Conference and Exposition, 2006. APEC '06.*, pages 7 pp.–, March 2006.

[48] J. M. Guerrero, J. Matas, L. Garcia de Vicuna, M. Castilla, and J. Miret. Decentralized control for parallel operation of distributed generation inverters using resistive output impedance. *IEEE Transactions on Industrial Electronics*, 54(2):994–1004, April 2007.

[49] Y. A. R. I. Mohamed and E. F. El-Saadany. Adaptive decentralized droop controller to preserve power sharing stability of paralleled inverters in distributed generation microgrids. *IEEE Transactions on Power Electronics*, 23(6):2806–2816, Nov 2008.

[50] R. Majumder, B. Chaudhuri, A. Ghosh, R. Majumder, G. Ledwich, and F. Zare. Improvement of stability and load sharing in an autonomous microgrid using supplementary droop control loop. *IEEE Transactions on Power Systems*, 25(2):796–808, May 2010.

[51] J. M. Guerrero, J. C. Vasquez, J. Matas, L. G. de Vicuna, and M. Castilla. Hierarchical control of droop-controlled ac and dc microgrids - a general approach toward standardization. *IEEE Transactions on Industrial Electronics*, 58(1):158–172, Jan 2011.

[52] X. Lu, K. Sun, J. Guerrero, and L. Huang. Soc-based dynamic power sharing method with ac-bus voltage restoration for microgrid applications. In *IECON 2012 - 38th Annual Conference on IEEE Industrial Electronics Society*, pages 5677–5682, Oct 2012.

[53] H. Bevrani, F. Habibi, P. Babahajyani, M. Watanabe, and Y. Mitani. Intelligent frequency control in an ac microgrid: Online pso-based fuzzy tuning approach. *IEEE Transactions on Smart Grid*, 3(4):1935–1944, Dec 2012.

[54] A. H. Etemadi, E. J. Davison, and R. Iravani. A decentralized robust control strategy for multi-der microgrids - part I: Fundamental concepts. *IEEE Transactions on Power Delivery*, 27(4):1843–1853, Oct 2012.

[55] A. H. Etemadi, E. J. Davison, and R. Iravani. A generalized decentralized robust control of islanded microgrids. *IEEE Transactions on Power Systems*, 29(6):3102–3113, Nov 2014.

[56] E. Davison. The robust decentralized control of a general servomechanism problem. *IEEE Transactions on Automatic Control*, 21(1):14–24, Feb 1976.

[57] H. Liang, B. J. Choi, W. Zhuang, X. Shen, A. S. A. Awad, and A. Abdr. Multiagent coordination in microgrids via wireless networks. *IEEE Wireless Communications*, 19(3):14–22, June 2012.

[58] A. Vaccaro, V. Loia, G. Formato, P. Wall, and V. Terzija. A self-organizing architecture for decentralized smart microgrids synchronization, control, and monitoring. *IEEE Transactions on Industrial Informatics*, 11(1):289–298, Feb 2015.

[59] D. Papadaskalopoulos, D. Pudjianto, and G. Strbac. Decentralized coordination of microgrids with flexible demand and energy storage. *IEEE Transactions on Sustainable Energy*, 5(4):1406–1414, Oct 2014.

[60] M. Bahramipanah, R. Cherkaoui, and M. Paolone. Decentralized voltage control of clustered active distribution network by means of energy storage systems. *Electric Power Systems Research*, 136:370 – 382, 2016.

[61] V. Nasirian, Q. Shafiee, J.M. Guerrero, F.L. Lewis, and A. Davoudi. Droop-free distributed control for ac microgrids. *IEEE Transactions on Power Electronics*, 31(2):1600–1617, 2016.

[62] Q. Li, F. Chen, M. Chen, J. M. Guerrero, and D. Abbott. Agent-based decentralized control method for islanded microgrids. *IEEE Transactions on Smart Grid*, 7(2):637–649, March 2016.

[63] A. Borghetti, M. Bosetti, S. Grillo, S. Massucco, C. A. Nucci, M. Paolone, and F. Silvestro. Short-term scheduling and control of active distribution systems with high penetration of renewable resources. *IEEE Systems Journal*, 4(3):313–322, Sept 2010.

[64] T. Wu, Q. Yang, Z. Bao, and W. Yan. Coordinated energy dispatching in microgrid with wind power generation and plug-in electric vehicles. *IEEE Transactions on Smart Grid*, 4(3):1453 – 1463, Sept 2013.

[65] S. Tan, J.-X. Xu, and S.K. Panda. Optimization of distribution network incorporating distributed generators: An integrated approach. *IEEE Transactions on Power Systems*, 28(3):2421 – 2432, Aug 2013.

[66] Y Zhang, N. Gatsis, and G.B. Giannakis. Robust energy management for microgrids with high-penetration renewables. *IEEE Transactions on Sustainable Energy*, 4(4):944 – 953, Oct 2013.

[67] F. Sossan, H. Bindner, H. Madsen, D. Torregrossa, L. Reyes-Chamorro, and M. Paolone. A model predictive control strategy for the space heating of a smart building including cogeneration of a fuel cell-electrolyzer system. *International Journal of Electrical Power & Energy Systems*, 62:879–889, 2014.

[68] G. Valverde and T. Van Cutsem. Model predictive control of voltages in active distribution networks. *IEEE Transactions on Smart Grid*, 4(4):2152–2161, Dec 2013.

[69] Christian Rehtanz. *Autonomous Systems and Intelligent Agents in Power System Control and Operation*. Springer, 2003.

[70] C. M. Colson and M. H. Nehrir. Comprehensive real-time microgrid power management and control with distributed agents. *IEEE Transactions on Smart Grid*, 4(1):617–627, 2013.

[71] Y. S. Foo and H. B. Gooi. Multi-agent system for optimization of microgrids. In *Proceedings of the 8th International Conference on Power Electronics (ECCE Asia)*, May 2011.

[72] L. Thillainathan, S. Dipti, A. M. Khambadkone, and H. N. Aung. Multiagent system for real-time operation of a microgrid in real-time digital simulator. *IEEE Transactions on Smart Grid*, 3(2):925–933, 2012.

[73] M. Pipattanasomporn, H. Feroze, and S. Rahman. Multi-agent systems in a distributed smart grid: Design and implementation. In *Proceedings of the IEEE/PES Power Systems Conference and Exposition (PSCE '09)*, 2009.

[74] A. Solanki, A. Nasiri, V. Bhavaraju, Y. L. Familiant, and Q. Fu. A new framework for microgrid management: Virtual droop control. *IEEE Transactions on Smart Grid*, 7(2):554–566, March 2016.

[75] C. Zhao, E. Mallada, S. Low, and J. Bialek. A unified framework for frequency control and congestion management. In *Proceedings of the 19th Power Systems Computation Conference (PSCC 2016)*, Jun 2016.

[76] B. Davie, A. Charny, J. C. R. Bennet, K. Benson, J.-Y. Le Boudec, W. Courtney, and D. Stiliadis. An expedited forwarding PHB (per-hop behavior). Technical report, Internet RFC 3246, 2002.

[77] K. Christakou, D.-C. Tomozei, J.-Y. Le Boudec, and M. Paolone. GECN: Primary voltage control for active distribution networks via real-time demand-response. *IEEE Transactions on Smart Grid*, 5(2):622–631, Feb. 2013.

[78] K. Christakou, D.-C. Tomozei, M. Bahramipanah, J.-Y. Le Boudec., and M. Paolone. Primary voltage control in active distribution networks via broadcast signals: The case of distributed storage. *IEEE Transactions on Smart Grid.*, 5(5):2314– 2325, 2014.

[79] IEEE Standards Association. IEEE std. c37.118.1-2011, IEEE standard for synchrophasor measurements for power systems. Technical report, Revision of the IEEE Std. C37.118.2005, 2011.

[80] IEEE Standards Association. IEEE std. c37.118.2-2011, IEEE standard for synchronophasor data transfer for power systems. Technical report, Revision of the IEEE Std. C37.118.2005, 2011.

[81] L. Zhang, A. Bose, A. Jampala, V. Madani, and J. Giri. Design, testing, and implementation of a linear state estimator in a real power system. *IEEE Transactions on Smart Grid*, PP(99):1–8, 2016.

[82] S. Sarri, L. Zanni, M. Popovic, J.-Y. Le Boudec, and M. Paolone. Performance assessment of linear state estimators using synchrophasor measurements. *IEEE Transactions on Instrumentation and Measurement*, 65(3):535–548, March 2016.

[83] M. Pignati, M. Popovic, S. Barreto Andrade, R. Cherkaoui, D. Flores, J.-Y. Le Boudec, M. M. Maaz, M Paolone, P. Romano, S. Sarri, T. T. Tesfay, D.-C. Tomozei, and L. Zanni. Real-Time State Estimation of the EPFL-Campus Medium-Voltage Grid by Using PMUs. In *The Sixth Conference on Innovative Smart Grid Technologies (ISGT2015)*, 2015.

[84] S.S. Acevedo and M. Molinas. Power electronics modeling fidelity: Impact on stability estimate of micro-grid systems. In *Proceedings of the 2011 IEEE PES Innovative Smart Grid Technologies Asia (ISGT)*, Nov. 13-16, 2011.

[85] N. Jelani and M. Molinas. Shunt active filtering by constant power load in microgrid based on irp p-q and cpc reference signal generation schemes. In *Proceedings of the 2012 IEEE International Conference on Power System Technology (POWERCON)*, Oct. 30 - Nov. 2, 2012.

[86] Hsiao-Dong Chiang and M.E. Baran. On the existence and uniqueness of load flow solution for radial distribution power networks. *IEEE Transactions on Circuits and Systems*, 37(3):410–416, 1990.

[87] K.N. Miu and Hsiao-Dong Chiang. Existence, uniqueness, and monotonic properties of the feasible power flow solution for radial three-phase distribution networks. *IEEE Transactions on Circuits and Systems I: Fundamental Theory and Applications*, 47(10):1502–1514, 2000.

[88] K. Christakou, J.-Y. Le Boudec, M. Paolone, and D.-C. Tomozei. Efficient computation of sensitivity coefficients of node voltages and line currents in unbalanced radial electrical distribution networks. *IEEE Transactions on Smart Grid*, 4(2):741–750, June 2013.

[89] Q. Zhou and J. Bialek. Generation curtailment to manage voltage constraints in distribution networks. *IET Generation, Transmission & Distribution*, 1(3):492–498, May 2007.

[90] N. Hoffmann and F. Wilhelm. Minimal invasive equivalent grid impedance estimation in inductuve-resistive power networks using extended Kalman filter. *IEEE Transactions on Power Electronics*, 29(2):631–641, 2014.

[91] Z. Staroszczyk. A method for real-time, wide-band identification of the source impedance in power sytems. *IEEE Transactions on Instrumentation and Measurement*, 54(1):377–385, 2005.

[92] M. Céspedes and J. Sun. Online grid impedance identification for adaptive control of grid-connected inverters. In *Proceedings of the IEEE Energy Conversion Congress and Exposition (ECCE)*, pages 914–921, Sept. 15-20, 2012.

[93] S. Agmon. The relaxation method for linear inequalities. *Canadian Journal of Mathematics*, 6:382–392, 1954.

[94] G. Costanzo, A. Bernstein, L. Reyes Chamorro, H.W. Bindner, J.-Y. Le Boudec, and M Paolone. Electric space heating scheduling for real-time explicit power control in active distribution networks. In *Proceedings of the 3rd IEEE PES Innovative Smart Grid Technologies (ISGT) Europe Conference, Istanbul, Turkey (October 12-15, 2014)*, 2014.

[95] J. Grainger and W. Stevenson. *Power System Analysis*. McGraw-Hill, 1994.

[96] A. Kabza. Just another fuel cell formulary. http://www.pemfc.de/FCF_A4.pdf.

[97] G. Marsala, M. Pucci, G. Vitale, M. Cirrincione, and A. Muraoui. A prototype of a fuel cell PEM emulator based on a buck converter. *Applied Energy*, 86:2192–2203, 2009.

[98] J. Larminie and A. Dicks. *Fuel Cell Systems Explained*. John Wiley and Sons Ltd., second edition edition, 2003.

[99] M.Y. El-Sharkh, A. Rahman, M.S. Alam, P.C. Byrne, A.A. Sakla, and T. Thomas. A dynamic model for a stand-alone {PEM} fuel cell power plant for residential applications. *Journal of Power Sources*, 138(1–2):199 – 204, 2004.

[100] J. M. Lee and B. H. Cho. A dynamic model of a pem fuel cell system. In *Applied Power Electronics Conference and Exposition, 2009. APEC 2009. Twenty-Fourth Annual IEEE*, pages 720–724, Feb 2009.

[101] J.T. Pukrushpan. *Modeling and Control of Fuel Cell Systems and Fuel Processors*. PhD thesis, University of Michigan, 2003.

[102] M. Bahramipanah, D. Torregrossa, R. Cherkaoui, and M. Paolone. Enhanced electrical model of lithium-based batteries accounting the charge redistribution effect. In *Power Systems Computation Conference (PSCC 2014)*, August 18-22, 2014, Wroclaw, Poland.

[103] B. Balvedere, M. Bianchi, A. Borghetti, C.A. Nucci, M. Paolone, and A. Peretto. A microcontroller-based power management system for standalone microgrids with hybrid power supply. *IEEE Transactions on Sustainable Energy*, 3(3):422–431, 2012.

[104] T.A. Smith, J.P. Mars, and G.A. Turner. Using supercapacitors to improve battery performance. In *Proceedings of the 2002 IEEE 33rd Annual Power Electronics Specialists Conference*, volume 1, pages 124–128, 2002.

[105] D. Torregrossa, M. Bahramipanah, E. Namor, R. Cherkaoui, and M. Paolone. Improvement of dynamic modeling of supercapacitor by residual charge effect estimation. *IEEE Transactions on Industrial Electronics*, 61(3):1345 – 1354, April 2013.

[106] S. Papathanassiou, N. Hatziargyriou, and K. Strunz. A benchmark low voltage microgrid network. In *Proceedings of the CIGRÉ Symposium "Power Systems with Dispersed Generation: technologies, impacts on development, operation and performances"*, Apr. 2005, Athens, Greece.

[107] N. Bory. Development of the thermal processes of the EPFL microgrid project. Master's thesis, EPFL, 2013.

[108] A. von Meier, D. Culler, A. McEachern, and R. Arghandeh. Micro-synchrophasors for distribution systems. In *Innovative Smart Grid Technologies Conference (ISGT), 2014 IEEE PES*, pages 1–5, Feb 2014.

[109] P. Romano and M. Paolone. Enhanced interpolated-DFT for synchrophasor estimation in FPGAs: Theory, implementation, and validation of a PMU prototype. *IEEE Transactions on Instrumentation and Measurement*, 63(12):2824–2836, December 2014.

[110] LEM. Voltage transducer CV-3000 specifications. http://www.lem.com/docs/products/cv_3-1000.pdf.

[111] LEM. Current transducer LF 205-S/SP1 specifications. http://www.lem.com/docs/products/lf%20205-s%20sp1.pdf.

[112] M. Popovic, M. M. Maaz, D.-C. Tomozei, and J.-Y. Le Boudec. iPRP - Parallel Redundancy Protocol for IP Networks: Protocol Design and Operation. *IEEE Transactions on Industrial Informatics*, 2016.

Lorenzo Enrique Reyes Chamorro

PERSONAL DETAILS

Address	École Polytechnique Fédérale de Lausanne (EPFL) Department of Electrical Engineering Distributed Electrical Systems Laboratory (DESL) ELL 037, Station 11, CH-1015 Lausanne, Switzerland
Phone	+41 21 69 37369
E-Mail	lorenzo.reyes@epfl.ch
Website	http://people.epfl.ch/lorenzo.reyes

EDUCATION

Ph.D. in Energy 2013 - 2016

École Polytechnique Fédérale de Lausanne (EPFL)

Supervisor: Professor Mario Paolone

Thesis title: Real-Time Control Framework for Active Distribution Networks – Theoretical Definition and Experimental Validation

B.Sc in Electrical Engineering and Diploma of Electrical Engineering 2003 - 2009

University of Chile, Chile

Supervisor: Professor Luis Vargas D.

Thesis title: Damping of electro-mechanical oscillations using HVDC link control

RESEARCH AREAS

- Microgrids
- Distributed Generation
- Smart Grid
- Small-Scale Generation Technologies
- Energy Storage Systems
- Real-time operation of Power Systems

PUBLICATIONS

Jounals

1. **L. Reyes-Chamorro**, A. Bernstein, J.-Y. Le Boudec and M. Paolone. A composable method for real-time control of active distribution networks with explicit power setpoints. Part II: Implementation and Validation,in *Electric Power Systems Research*, vol.125, num.August, p.265-280, 2015.

2. A. Bernstein, **L. Reyes-Chamorro**, J.-Y. Le Boudec and M. Paolone. A composable method for real-time control of active distribution networks with explicit power setpoints. Part I: Framework,in *Electric Power Systems Research*, vol.125, num.August, p.254-264, 2015.

3. K. Ubilla, G. Jiménez, R. Hernández, **L. Reyes-Chamorro**, C. Hernández, B. Severino, R. Palma-Behnke. Smart microgrids as a solution for Rural Electrification: Ensuring long-term sustainability through cadastre and business models. *IEEE Transactions on Sustainable Energy*, vol. 5, no. 4, pp. 1310-1318, October 2014.

4. F. Sossan, H. Bindner, H. Madsen, D. Torregrossa, **L. Reyes-Chamorro**, M. Paolone. A model predictive control strategy for the space heating of a smart building including cogeneration of a fuel cell-electrolyzer system. *International Journal of Electrical Power and Energy Systems*, vol.62, num.November, p.879889, 2014.

5. Palma-Behnke, C. Benavides, F. Lanas, B. Severino, **L. Reyes**, J. Llanos, D. Sáez. A Microgrid Energy Management System Based on the Rolling Horizon Strategy. *IEEE Transactions on Smart Grid*. June 2013, pp. 996 - 1006

6. Alvial-Palavicino C., Garrido-Echeverría N., Jiménez-Estévez G., **Reyes L.**, Palma-Behnke R. A Methodology for Community Engagement in the Introduction of Renewable based Smart Microgrid. *Energy for Sustainable Development* 15, pp. 314323, 2011.

Conferences and Magazines

1. A. Bernstein, J.-Y. Le Boudec, M. Paolone, **L. Reyes-Chamorro** and W. Saab. Aggregation of Power Capabilities of Heterogeneous Resources for Real-Time Control of Power Grids. *Proceedings of the 19th Power Systems Computation Conference (PSCC 2016)*, Genoa, Italy, 2016.

2. **L. Reyes-Chamorro**, M. Paolone, A. Bernstein and J.-Y. Le Boudec. A SuperCapacitor Agent for Providing Real-Time Power Services to the Grid. *Proceedings of the IEEE PES Conference on Innovative SMART GRID Technologies (ISGT-LA 2015)*, Montevideo, Uruguay, 2015.

3. A. Bernstein, **L. Reyes-Chamorro**, J.-Y. Le Boudec and M. Paolone. Real-Time Control of Microgrids with Explicit Power Setpoints: Unintentional Islanding. *Proceedings of the 2015 IEEE PES PowerTech*, Eindhoven, Netherlands, 2015.

4. G. Tommaso Costanzo, A. Bernstein, **L. Reyes-Chamorro**, H. Binder, J.Y. Le Boudec, M. Paolone. Electric Space Heating Scheduling for Real-time Explicit Power Control in Active Distribution Networks. *Proceedings of theIEEE PES ISGT Europe 2014, Istanbul*, Turkey, October 12-15, 2014.

5. C. Abbey, D. Cornforth, J. Dilliott, N. Hatziargyriou, T. Oyama, C. Marnay, K. Hirose, A. Kwasinski, E. Kyriakides, G. Platt, **L. Reyes**, S. Suryanarayanan, Microgrids in Disaster Relief. *IEEE Power & Energy Magazine*, May-June 2014.

6. F. Ávila, D. Sáez, G. Jiménez-Estévez, **L. Reyes**, A. Nuñez. Fuzzy demand forecasting in a predictive control strategy for a renewable-energy based microgrid. *Proceedings of the 2013 European Control Conference*, 17-19 July 2013, Zurich.

7. A. Vargas-Serrano, D. Sáez, **L. Reyes**, B. Severino, R. Palma-Behnke, R. Cárdenas. Design and Experimental Validation of a Dual Mode VSI Control System for a Micro-grid with Multiple Generators. *Proceeding of the 38th Annual Conference of the IEEE Industrial Electronics Society 2012*.

8. R. Palma-Behnke, D. Ortiz, **L. Reyes**, G. Jiménez-Estévez, N. Garrido. A social SCADA Approach for a Renewable based Microgrid - The Huatacondo Project, *2011 IEEE Power & Energy Society General Meeting*, Detroit, Michigan, USA. July 24 - 28 2011.

9. Vargas-Serrano A., **Reyes L.**, Sáez D., Palma-Behnke R. Design of Bidirectional Inverter Operating in a Microgrid with Multiple Generators, *Revista Chilena de Ingeniera. Anales del Instituto de Ingenieros de Chile*, December, 2011. pp 89- 98.

PROFESSIONAL EXPERIENCE

Electricity Technician January 2009
Energy Center - FCFM, Chile
PV module installation for rural electrification in Mineral de Talca, Ovalle

Project Engineer August 2009
Energy Center - FCFM, Chile
Study on the long-term prediction of the electrical demand in San Pedro de Atacama

Project Engineer October 2009 - October 2010
Energy Center - FCFM, Chile
Implementation of the first Latin American renewable-based microgrid in a community setting for Huatacondo
https://www.youtube.com/watch?v=BHh98yerEmM

Project Manager June - July 2011
Energy Center - FCFM, Chile
Energetic demand diagnosis and energy program definition for San Juan Bautista, Robinson Crusoe Island, Juan Fernandez Archipelago

Project Manager September - October 2011
Energy Center - FCFM, Chile
Technical, economic and social pre-feasibility of electrification of Ollagüe.
https://www.youtube.com/watch?v=3Zgcw46nRUA

Project Manager November 2011 - January 2012
Energy Center - FCFM, Chile
Study of technical specifications for a diesel-based system and design of an emergency microgrid for San Juan Bautista, Robinson Crusoe Island, Juan Fernandez Archipelago.

Project Manager March - July 2012
Energy Center - FCFM, Chile
Design and implementation of a PV power plant for a rural school in El Romeral, La Serena

Project Manager August 2011 - December 2012
Energy Center - FCFM, Chile
A standalone micro-hydraulic generator prototype for distributed generation

AWARDS AND GRANTS

PhD Fellowship 2013 - 2016
Advanced Human Capital Program of the National Commission for Scientific and Technological Research (CONICYT) of Chile
USD$25,000 *per annum* stipend and consumables

Best Poster Award December 2014
2014 Annual Conference of the SCCER-FURIES
Real-Time Control of Active Distribution Networks by Using Explicit Power Setpoints (COMMELEC)

EPFL Seed Money Program 2015
Campus-level Smart Grid demonstration project at Austral University
CHF 10,000, students exchange and laboratory material.

PEER REVIEW

1. IEEE Transactions on Industrial Informatics
2. International Journal of Electrical Power and Energy Systems
3. Elsevier Sustainable Energy, Grids and Networks Journal
4. IEEE Transactions on Smart Grid
5. Renewable and Sustainable Energy Reviews Journal
6. IEEE/PES Transmission and Distribution, Latin America
7. IEEE/PES Innovative Smart Grids Technologies Latin America
8. MDPI Energies

LANGUAGE SKILLS

- Spanish (mother tongue).
- English, fluent (professional proficiency).
- French, fluent (Level B2 according to European Language Portfolio).

OTHER ACTIVITIES

- President and Founder of the Association of Chilean Researchers in Switzerland. http://www.ices-net.ch/
- Ad-honorem Professor at Austral University of Chile.